DOI:10.14753/SE.2025.3224

SEMMELWEIS EGYETEM

DOKTORI ISKOLA

Ph.D. értekezések

3224.

SZEKÉR PATRIK

Patobiokémia

című program

Programvezető: Dr. Csala Miklós, egyetemi tanár

Témavezető: Dr. Gyöngyösi Norbert, egyetemi adjunktus

DOI:10.14753/SE.2025.3224

DEVELOPMENT AND OPTIMIZATION OF SCREENING ASSAYS FOR TARGETED MINIPROTEIN THERAPEUTICS: FOCUS ON KV1.3 AND MMP-2

Ph.D thesis

Patrik Szekér

Semmelweis University Doctoral School

Division of Molecular Medicine

Supervisor:	Norbert Gyöngyösi, PhD
Official reviewers:	Roland Csépányi-Kömi, PhD
	József Dobó, PhD
Head of the Complex Examination Committee:	Péter Várnai, DSc
Members of the Complex Examination Committee:	Krisztina Káldi, MD, PhD
	László Nyitray, DSc

Budapest

2025

DOI:10.14753/SE.2025.3224

TABLE OF CONTENTS

DOI:10.14753/SE.2025.3224

DOI:10.14753/SE.2025.3224

DOI:10.14753/SE.2025.3224

LIST OF ABBREVIATIONS

A488 – Alexa fluor 488 (a fluorophore)

ADA – Anti-drug antibody

ADC – Antibody-drug conjugate

Adoptive EAE – Adoptive transfer experimental autoimmune encephalomyelitis

ANX-2 – Annexin A2

BSA – Bovine serum albumin

cDNA – Complementary DNA

CLC-3 – Chloride channel 3

CR-EAE – Chronic relapsing-remitting experimental autoimmune encephalomyelitis

CRAC – Calcium release-activated calcium channel

CRPs – Cysteine-rich peptides

CsA – Cyclosporine A

CTX – Chlorotoxin

Cy-5 – Cyanine 5 (a fluorophore)

DDM – n-Dodecyl-beta-maltoside

DDDKTX1 – Inactive Kaliotoxin-1

DMEM – Dulbecco's modified Eagle medium

DNA – Deoxyribonucleic acid

DPBS – Dulbecco’s phosphate-buffered saline

DsbC – Disulfide bond isomerase C

DTH – Delayed-type hypersensitivity

DTT – Dithiothreitol

E. coli – Escherichia coli

EC50 – Half-maximal effective concentration

ECM – Extracellular matrix

EDTA – Ethylenediaminetetraacetic acid

EGTA – Ethylene glycol tetraacetic acid

ELISA – Enzyme-linked immunosorbent assay

FACS – Fluorescence-activated cell sorting

FBS – Fetal bovine serum

FRET – Förster resonance energy transfer

GBM – Glioblastoma multiforme

GFP – Green fluorescent protein

GPCRs – G-protein coupled receptors

HBSS – Hanks' balanced salt solution

HPLC – High-performance liquid chromatography

HTS – High-throughput screening

HgTX1 – Hongotoxin-1 (Kv1.3 channel inhibitor)

h – Human

IC50 – Half-maximal inhibitory concentration

IgG – Immunoglobulin G

IMAC – Immobilized metal affinity chromatography

IPTG – Isopropyl β-D-1-thiogalactopyranoside

KD – Equilibrium dissociation constant

KCNE – Potassium voltage-gated channel subfamily E regulatory subunits

KChIP – Potassium channel interacting proteins

KcsA – Potassium channel from Streptomyces lividans

KTX1 – Kaliotoxin-1 (Kv1.3 channel inhibitor)

Kv1.x – Voltage-gated potassium channel subfamily 1.x

Kv1.3 – Voltage-gated potassium channel subtype 1.3

Kvβ – Voltage-gated potassium channel beta subunits

LB – Luria-Bertani medium

mAbs – Monoclonal antibodies

MMP – Matrix metalloproteinase

MMP-2 – Matrix metalloproteinase-2

MoA – Mechanism of action

MTX – Maurotoxin

NaCl – Sodium chloride

NFAT – Nuclear factor of activated T cells

NRP1 – Neuropilin-1

PASI – Psoriasis area and severity index

PBS – Phosphate-buffered saline

PBMCs – Peripheral blood mononuclear cells

PDB – Protein Data Bank

PCR – Polymerase chain reaction

PEG – Polyethylene glycol

PIA – Pristane-induced arthritis

PK/PD – Pharmacokinetics/pharmacodynamics

Potassium channel abbreviation – Likely Kv1.x family (found on page 21)

qPCR – Quantitative polymerase chain reaction

rCTX – Recombinant chlorotoxin

RNA – Ribonucleic acid

RP-HPLC – Reverse-phase high-performance liquid chromatography

RT-PCR – Reverse transcription polymerase chain reaction

RFI – Relative fluorescence intensity

SEC – Size-exclusion chromatography

ShK – Stichodactyla toxin

SDS-PAGE – Sodium dodecyl sulfate polyacrylamide gel electrophoresis

SplB – Staphylococcal serine protease

SPR – Surface plasmon resonance

T+F – Turret-filter

T-only – Turret-only

TBS – Tris-buffered saline

TCEP – Tris(2-carboxyethyl)phosphine

TEA+ – Tetraethylammonium ion

TEM – Transmission electron microscopy

TCR – T cell receptor

TIMP-2 – Tissue inhibitor of metalloproteinases 2

TIMPs – Tissue inhibitors of metalloproteinases

TMB – Tetramethylbenzidine

TMS – Transmembrane segment

UV – Ultraviolet

VEGFA – Vascular endothelial growth factor A

VSD – Voltage-sensing domain

DOI:10.14753/SE.2025.3224

1 INTRODUCTION

1.1 Miniproteins as therapeutic modalities

Miniproteins are small (1–10 kDa), highly stable proteins with rigid tertiary structures making them promising tools for drug development, especially against targets considered "undruggable" by traditional modalities (1). They represent a promising class of therapeutics, combining the benefits of both small molecules and large biologics, without their limitations (**Figure 1.**). Their stability comes from disulfide bonds, hydrophobic cores, metal coordination, or engineered constraints, enhancing resistance to degradation and oxidation (2). Unlike larger biologics, their moderate size enables superior tissue penetration, allowing them to reach specific locations that might otherwise be inaccessible. Miniproteins can exhibit high affinity and extreme selectivity due to their large interaction surface and produce no harmful breakdown products, as they are made of naturally metabolized amino acids. Additionally, they can be readily engineered for low immunogenicity, reducing the likelihood of anti-drug antibody (ADA) responses. Their developability is further enhanced by tunable pharmacokinetics/pharmacodynamics (PK/PD) through modular fusions and low-cost, versatile manufacturing options using synthetic and recombinant methods (1,3,4).

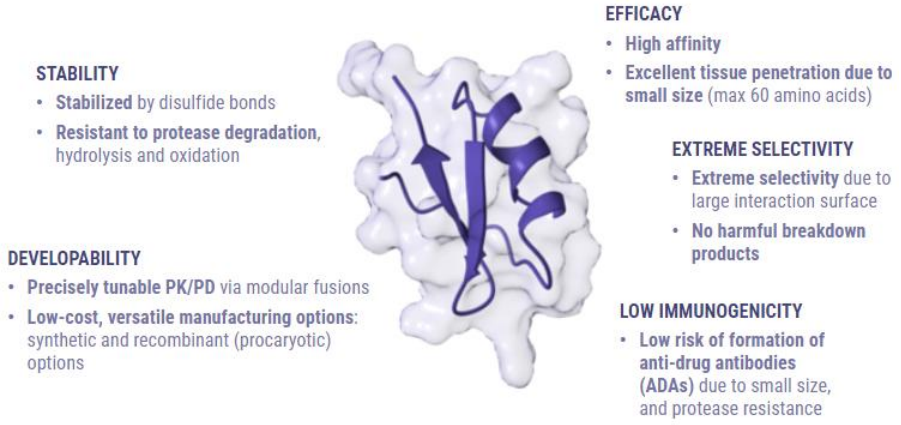

Figure 1. *Miniproteins combine the benefits of small molecules and large biologics. Miniproteins drugs can be small, stable, and highly selective molecules with excellent tissue penetration and low immunogenicity. Their modular design allows tunable PK/PD and cost-effective production, making them promising scaffolds for next-generation therapeutics.*

Despite these advantages, miniproteins have not yet realized their full potential, but with the appropriate tools they have the potential to be the next generation of therapeutic agents, offering targeted treatments with improved safety and effectiveness for a range of diseases (1,5,6).

1.2 Animal peptide-toxins: diverse miniprotein scaffolds with therapeutic potential

Animal venom is a rich source of potential miniprotein drugs and also contains a diverse array of bioactive molecules, including enzymes, peptides, lipids, biogenic amines, and nucleotides (7–9). With tens of thousands of venomous species worldwide and potentially millions of unique toxins, the diversity of venom components is huge. In animal venom research, the terms "peptides," "peptide toxins," and "small proteins" are commonly used interchangeably (10–13). However, from a biochemical perspective, many of these molecules are more accurately described as miniproteins. *In vivo* stability is especially prominent in cysteine-rich peptides (CRPs). Disulfide bonds stabilize their structures, supporting secondary elements like alpha-helices and beta-sheets, and often a well-defined tertiary structure. This distinction between peptides and miniproteins is crucial, as their properties provide significant PK/PD advantages, demonstrating unique properties both *in vitro* and *in vivo* (14).

Venom-derived miniproteins show remarkable diversity targeting multiple biological pathways (7,8). They are typically composed of 20-70 amino acids and originate from various venomous species like scorpions, snakes, spiders, and sea anemones. The structural diversity of these miniproteins, makes them potent candidates for therapeutic applications (1,9,13,15,16).

Miniproteins vary in structure, from β-strands like κ-PVIIA (cone snail toxin) to α-helices, seen in scorpion κ-hefutoxin 1 and sea anemone BgK. Another variation, the 310 αα type, includes the Stichodactyla toxin (ShK). Moreover, a mix of these structures—such as 310 ββ, αββ, βαββ, and 310 ββα types—are illustrated through examples like spider hanatoxin 1, scorpion maurotoxin, scorpion charybdotoxin, and snake dendrotoxin I, shown on **Figure 2.** (17–19) .

DOI:10.14753/SE.2025.3224

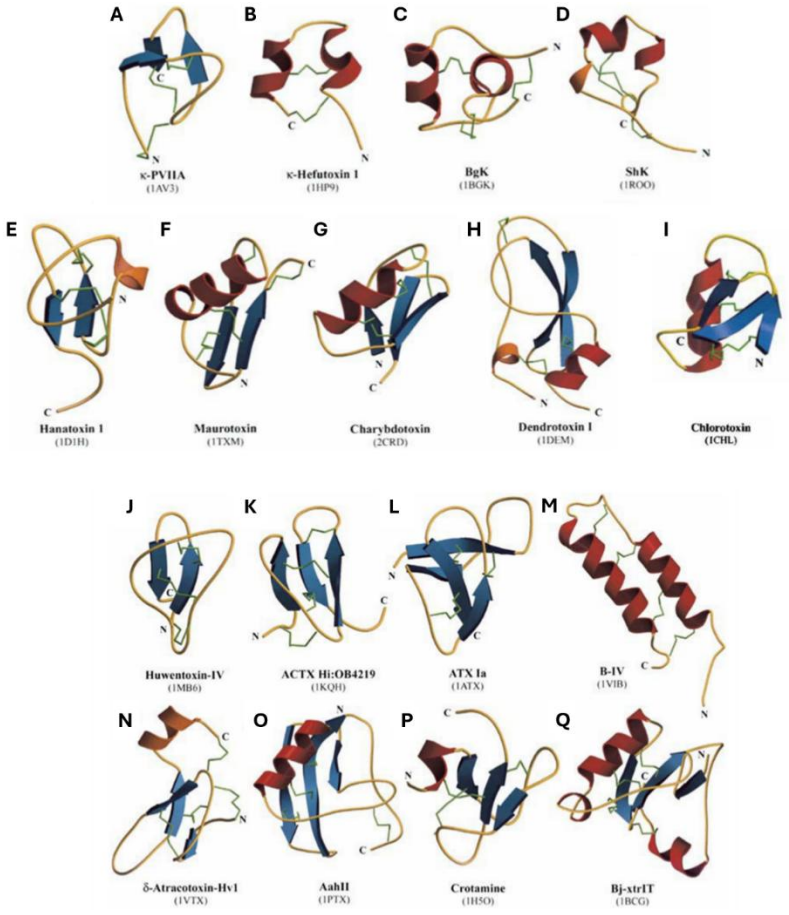

Figure 2. *Different scaffolds of venom derived miniproteins. Each subfigure is labeled with a letter* ***(A–Q)****, representing a distinct miniprotein structure. The names of the toxins and their respective Protein Data Bank (PDB) identifiers are provided beneath each representation (17).*

Scorpion venom is among the richest sources of peptide toxins, with a single gland containing around 70 different sequences (20). They are acting on various ion channels including Na^+, Cl^-, K^+ channels sharing a common structural scaffold, known as cysteine-stabilized alpha-beta (CSαβ) structure (**Figure 2., F,G,I**). The structural diversity within the CSαβ framework is fundamental to the specificity and potency of scorpion venom toxins (**Table 1.**). Despite having a similar fold, the disulfide bonding pattern and cysteine framework can vary greatly among different members, creating subgroups within this structural family. Generally, larger miniproteins composed of 60-70 amino acids and containing four disulfide bonds typically target Na^+ channels. In contrast, shorter peptides with 30-40 amino acids and three to four disulfide bonds are usually involved in blocking K^+ and Cl^- channels (3,21).

DOI:10.14753/SE.2025.3224

Table 1. *Structural data and corresponding pharmacology of reference animal toxins acting on K^+ and Cl^- channels. Representative miniprotein toxins from animal venoms are shown with their sequences, structural folds, and main ion channel targets. Structural types include β-sheet, α-helix, and mixed folds such as CSαβ, 3_{10}αα, and βαββ. Most act as pore blockers of K^+ channels, while some target Cl^- channels. Variations in disulfide bonding and sequence length contribute to their specificity and pharmacological activity (17).*

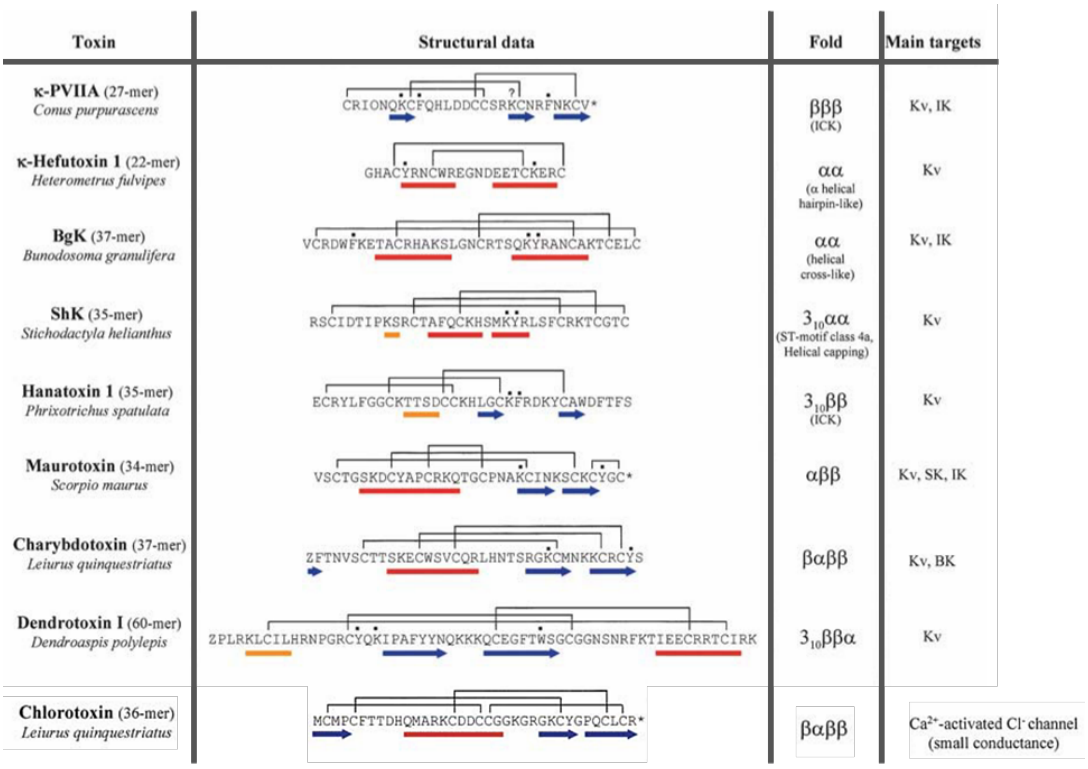

In the case of K^+ channel targeting toxins, the CSαβ fold is often required to bind to the pore domain of ion channels, acting as pore blocker toxins (22,23). These toxins physically obstruct the ion conduction pathway. Conversely, toxins with different structures like spider toxins interact with the voltage-sensing domains (VSD) of ion channels, functioning as gating modifier toxins (24). Besides ion channels these compounds are highly effective at targeting specific receptors (e.g., G-protein-coupled receptors), and enzymes (e.g., matrix metalloproteinases, serine proteases) involved in various physiological and pathological processes.

Although promising, naturally souruced miniproteins can face drug development challenges like selectivity, solubility, and the presence of immunogenic epitopes (7,25,26). These issues can be addressed through specific modifications, which need

advanced computational tools, robust binding and screening assays and sophisticated lead selection procedures (27–30).

1.3 Discovery of potential miniprotein drugs – Historical perspectives

Peptide and miniprotein drug discovery started with observing venom effects in humans before studying their mechanisms (phenotypic-based approach). This method did not require prior knowledge of the target mechanism, but allowed high probability of discovering therapeutically relevant compounds. However, optimizing these compounds was challenging without understanding their specific mechanisms (31). A successful example of this approach is Prialt® (ziconotide), a painkiller derived from the venom of the sea snail Conus magus (32). Early drug discovery efforts involved low-throughput methods, such as electrophysiological recordings, which provided insights into the effects of venoms and toxins on cellular functions (33).

From the nineteen-nineties, drug discovery transitioned from a phenotypic-based approach to a target-based version. This strategy focuses on identifying the role of specific targets in diseases and screening for novel compounds that interact with them. Despite using molecular and chemical knowledge to validate a hypothesis, it does not always ensure relevance in living organisms. To discover bioactive peptides in venoms, both bioassay-guided and sequence-based methods were employed. The bioassay-guided approach purifies venom, tests its fractions for activity, and isolates the active peptide. The sequence-based method involves sequencing the venom gland transcriptome and using bioinformatics to identify potential toxin-like genes, leading to the identification of novel compounds in the venom (34).

With so many venomous species and complex venoms, much of their medical potential is still unexplored. New technologies now allow for large-scale production and optimization of venom-derived miniproteins, improving their therapeutic potential. Biotechnology nowadays starts to uncover the potential of venom-derived molecules, with high-throughput screening (HTS) becoming a key method in drug discovery over the past two decades. Combining computational tools with molecular biology will further accelerate their development into effective drugs (35).

DOI:10.14753/SE.2025.3224

1.4 Development of screening assays - The key to effective drug discovery

In drug discovery, after validating a drug target, the next step is finding compounds (hit and lead molecules) that effectively modulate it. This requires development of screening assays. Screening assays are indispensable to find compounds with high affinity and selectivity for the target. Binding assays, such as radioligand binding, fluorescence-based assays, surface plasmon resonance (SPR), and enzyme-linked immunosorbent assays (ELISA), are commonly used to study interactions between miniproteins and their targets. Functional assays, including enzyme activity assays, electrophysiology assays, and fluorescence resonance energy transfer (FRET) assays, can subsequently confirm that these interactions lead to the desired biological effect (36). Having a screening assay alone is not enough. Successful drug discovery depends on optimizing assays, especially for HTS (**Figure 3.**). Without optimization, HTS cannot reliably identify the most selective and potent compounds.

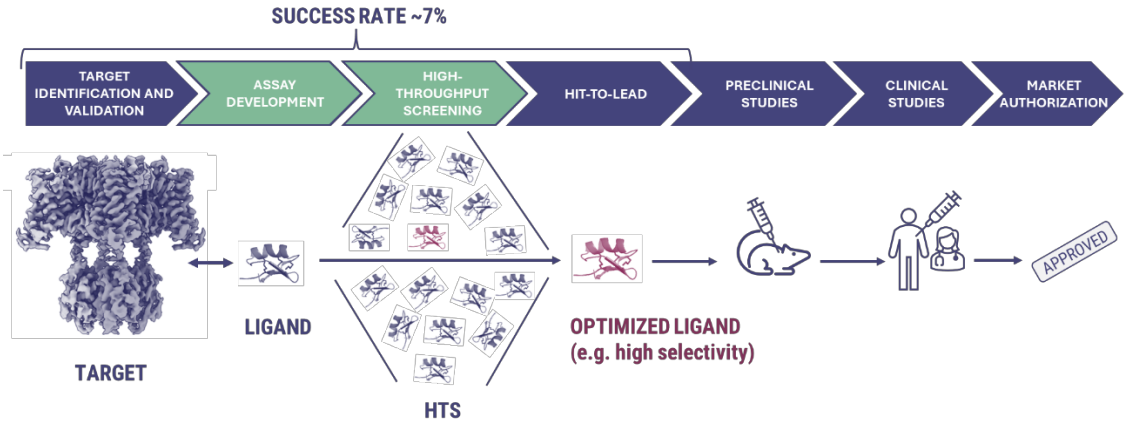

Figure 3. *Overview of the drug discovery and development stages. The process begins with identifying and validating a biological target, followed by assay development and high-throughput screening (HTS) to find initial ligands. Selected hits are optimized for properties like selectivity during the hit-to-lead phase. Promising candidates then advance through preclinical testing in animals, clinical trials in humans, and finally, regulatory approval.*

Refining assay conditions - improving signal-to-noise ratios, reducing variability, and improving reproducibility and predictivity - enables HTS to efficiently screen large compound libraries. This optimization improves the success rate by accelerating the identification of promising drug candidates and facilitating their transition into preclinical development.

1.5 Challenges in screening assay development for complex target-ligand combinations

Developing screening assays for complex targets, especially those targeted by cysteine-rich miniproteins, depends on both ligand properties and target complexity. Ligands vary in affinity, specificity, stability, and manufacturability, impacting assay sensitivity and reliability. Low-affinity ligands (Kd>100nM) demand highly sensitive detection methods, since non-specific binding increases false positives, requiring stringent washing steps. However, for high-affinity ligands (Kd < 1 nM), selectivity becomes more important to reduce false positives. Stability and solubility challenges also necessitate optimized assay conditions to prevent artifacts. Similarly, target complexity and dynamics influence assay design. Membrane-bound targets like ion channels require more sophisticated assays that preserve native structure, while soluble enzymes and other extracellular receptors may be compatible with simpler formats. For HTS, assays must be cost-efficient, sensitive, and selective. Screening large libraries requires keeping assay costs low (ideally <$1 per compound).

Computational tools like molecular docking and machine learning streamline small-molecule screening by enabling rapid virtual screening and reducing reliance on physical libraries. While *in silico* screening of small molecules also require validation, miniprotein screening depends even more on wet lab experiments due to their complex folding and structural variability. Selecting the appropriate assay format (e.g., microplate-based, bead-based, chip-based) and designing a well-defined screening target are essential for achieving high translational accuracy in miniprotein drug discovery. Display technologies—including phage, yeast, bacterial, mRNA, and ribosome display—also remain key tools for screening miniproteins.

1.6 Phage display

Phage display, developed by G. Smith in 1985, is a powerful method for presenting polypeptides on the surface of filamentous bacteriophages, such as M13 (37). This technology links the phenotype of displayed peptides or proteins with the genotype (genetic information) contained within the same virion, allowing for rapid generation and screening of diverse peptide and protein libraries. The technique has proven instrumental for applications including drug discovery, delivery and molecular biology (38,39).

Phage display uses different bacteriophages, with M13, T7, and lambda being the most common (**Figure 4**.) (40).

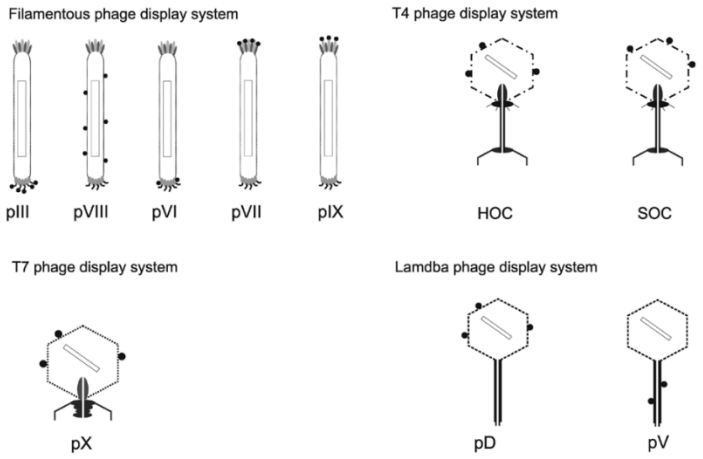

Figure 4. *Schematic presentation of phage display systems. Different phage types (filamentous M13, T4, T7, and lambda) and their coat proteins (e.g., pIII, pVIII, HOC, SOC, pX, pD, pV) used for peptide or protein display are illustrated (38).*

Each phage offers distinct advantages depending on the target molecule and desired expression characteristics:

- **T7 phage display:** Known for its robustness, T7 phage displays peptides directly on its capsid, avoiding periplasmic secretion and maintaining stability under conditions that may inactivate other phages (41).
- **Lambda phage display:** Capable of displaying larger proteins (42).
- **Filamentous phages (M13, f1, fd):** Filamentous phages, particularly M13, are among the most widely used due to their ability to display peptides and proteins on various coat proteins, making them highly versatile (43).

1.6.1 M13 phage display system

The M13 filamentous bacteriophage is the most commonly used phage display system used for identifying high-affinity binders in antibody discovery, affinity maturation and epitope mapping (44,45). This phage system offers multiple coat proteins that can be used for display, each suited to different purposes (**Figure 4.**) (38,45):

- **pVIII display:** The main coat protein, appears in about 3,000 copies per phage, making it ideal for displaying short peptides. This high density enhances signal

detection in assays where strong binding signals are advantageous. However, pVIII can only display short peptides (typically 6-7 residues) without affecting phage stability.

- **pVI display:** pVI allows moderate-density display of larger peptides but is used less due to compatibility issues.
- **pVII and pIX display:** These minor coat proteins, found at the opposite end of the phage from pIII, allow multivalent peptide display. However, pVII and pIX display systems have limited use in comparison to other coat proteins due to lower binding stability.
- **pIII display:** As a minor coat protein located at the tip of the M13 phage, pIII is particularly advantageous for displaying larger and more complex proteins, such as antibody fragments. With only a few copies per phage particle, pIII allows monovalent presentation of full-length proteins and complex binding domains without compromising phage viability. This lower-density display reduces steric hindrance, helping maintain structural integrity and binding specificity. The pIII system allows for a diverse library of up to ~10^9 variants, which is essential for identifying high-affinity binders for therapeutic and diagnostic applications.

The M13 phage system, especially through the pIII display, has proven invaluable in phage display technology, offering a robust and versatile platform for screening and optimizing biologics.

1.6.2 *In vitro* biopanning process using M13 bacteriophages

Biopanning is a targeted selection process designed to identify high-affinity ligands, such as peptides/miniproteins and antibodies, from million-scale libraries panned against purified biomolecules. Unlike conventional high-throughput screening methods, which often require subsequent wet lab validation, biopanning allows for a streamlined, iterative approach where the library of potential binders is exposed to a target molecule or cell type in conditions that closely resemble real biological environments (46).

While alternative phage display platforms are available, M13 remains the preferred choice due to its monovalent display capability, ease of purification, and broad library diversity. To date, 14 monoclonal antibodies (mAbs) derived from phage display using the M13 pIII system have been approved for clinical use. They are targeting a range of

diseases including anthrax, macular degeneration, rheumatoid arthritis, and various cancers such as non-small cell lung carcinoma, colorectal and gastric cancer (47). The M13 phage display system operates as a solid phase biopanning technique, where the target molecule is immobilized on a solid support, such as on a plate or bead surface. After library production (1st step) each cycle in the biopanning process includes binding (2nd step), washing to remove non-specific ligands (3rd step), elution of high-affinity binders (4th step), and amplification (5th step), refining the selection with each iteration cycle (**Figure 5.**). Once phages are sufficiently enriched on the target compared to the control, the molecules displayed on them are identified as hits through sequencing (6th step). Then, these hits can be analyzed further and developed into lead compounds (7th step).

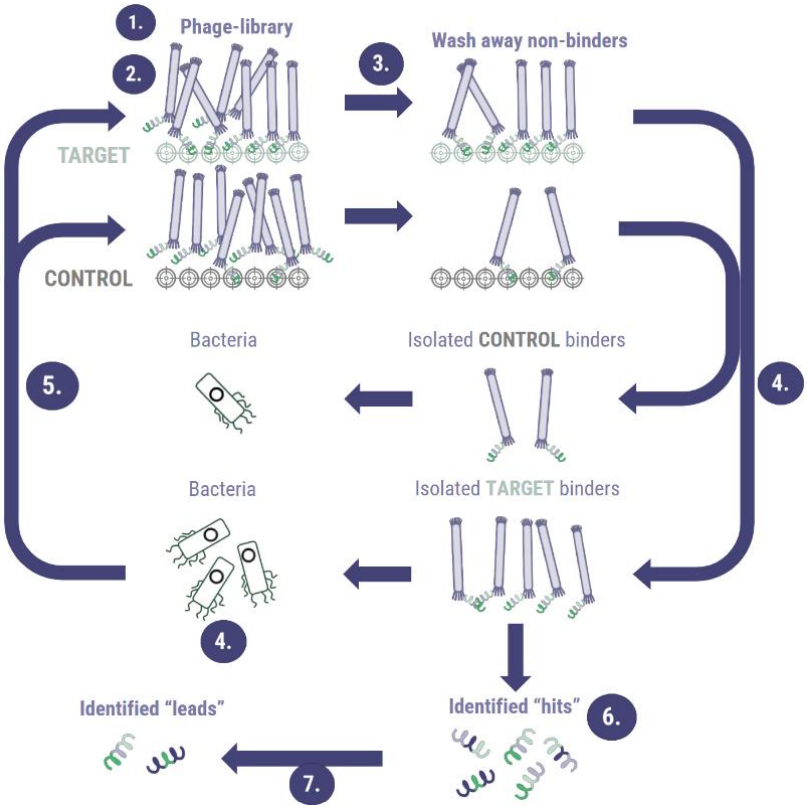

Figure 5. *Schematic summary of in vitro phage panning with the M13 pIII system. The biopanning process begins with (1.) generating a phage-displayed library (2.) incubation of the library to allow binding to immobilized molecules. Next, (3.) non-binders are washed away, and (4.) specific binders are eluted from both target and control surfaces. These are then (5.) amplified in E. coli bacteria. After several rounds, (6.) target-specific*

binders are identified as hits through sequencing, and (7.) these hits can be further developed into lead compounds.

1.7 Ideal targets for miniprotein drug discovery

Over the last two decades, genomics has greatly accelerated the discovery of new molecular targets but has not directly led to the development of new drugs. Their structural complexity often hinders effective small-molecule binding, and their location restricts access to large biologics. These challenging targets include ion channels, G-protein-coupled receptors (GPCRs), selective cytokine signaling pathways, and certain enzymes—all of which play critical roles in disease but remain extremely difficult to drug (**Figure 6.**).

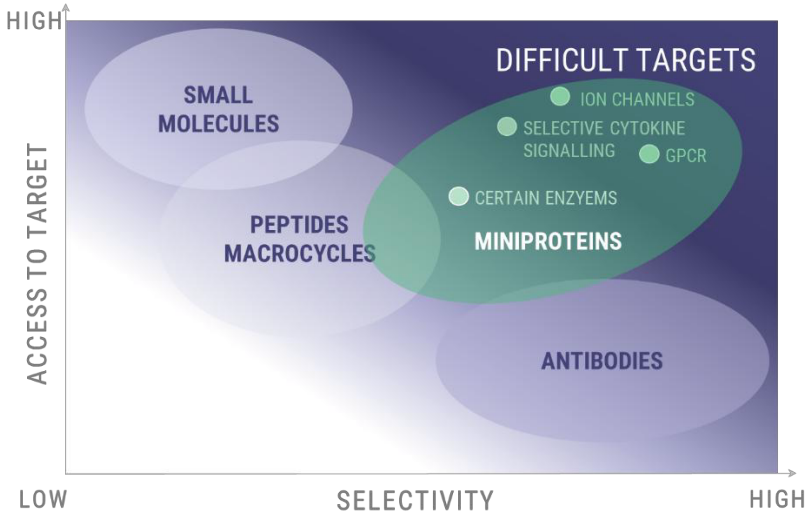

Figure 6. *Miniproteins accessing difficult targets with high potency and selectivity. Miniproteins occupy a unique space in drug discovery by combining the high target accessibility of small molecules with the selectivity of biologics. They are especially suited for challenging targets like ion channels, GPCRs, cytokine signaling pathways, and certain enzymes, where traditional modalities often fall short.*

This is especially important for voltage-gated potassium channels (Kv), which differ by only a few amino acids in their extracellular pore domain - key sites for selective channel blockers. Similarly challenging targets are matrix metalloproteinases (MMPs) with highly similar catalytic domains. By focusing on high-specificity yet difficult-to-drug targets,

miniproteins provide a new promising modality in drug discovery, combining the precision of biologics and the target access of small molecules.

1.8 Matrix metalloproteinases (MMPs) as promising therapeutic targets

MMPs represent a diverse family of 23 proteolytic enzymes that contribute to extracellular matrix (ECM) remodeling, wound healing, and various physiological processes (48). They share a common structural organization, including a pro-peptide domain, a catalytic domain with a zinc-binding site, and often a hemopexin-like C-terminal domain that contributes to substrate specificity and interaction with tissue inhibitors of metalloproteinases (TIMPs)(49). Their active sites are zinc-dependent and highly conserved, featuring three histidine residues bound to the catalytic zinc. Based on substrate specificity and domain organization, MMPs are classified into several subgroups: collagenases, gelatinases, stromelysins, matrilysins, and membrane-types, which highlight their diverse roles in maintaining and regulating ECM. Collagenases (e.g., MMP-1, MMP-8, MMP-13) degrade interstitial collagens, whereas gelatinases (e.g., MMP-2, MMP-9) primarily degrade gelatin and collagen type IV. Stromelysins (e.g., MMP-3, MMP-10) act on a broad range of ECM components, matrilysins (e.g., MMP-7, MMP-26) degrade proteoglycans, laminin, and other ECM proteins, and membrane-type MMPs (e.g., MMP-14, MMP-15) are anchored to the cell membrane and can activate other MMPs (**Figure 7.**) (50).

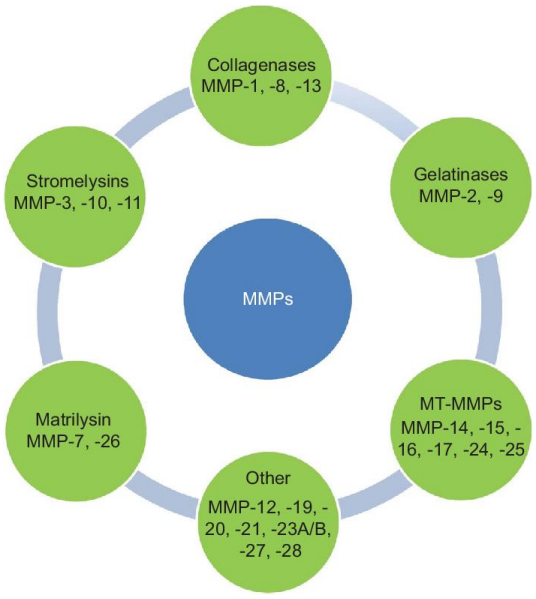

Figure 7. *Classification of matrix metalloproteinases (MMPs). MMPs are divided into subgroups based on substrate specificity and domain structure: collagenases (MMP-1, -8, -13), gelatinases (MMP-2, -9), stromelysins (MMP-3, -10, -11), matrilysins (MMP-7, -26), membrane-type MMPs (MMP-14 to -17, -24, -25), and others (MMP-12, -19 to -21, -23A/B, -27, -28) (50).*

MMP activity is regulated in four key ways. First, gene expression controls how much MMP is produced by managing transcription and mRNA stability. Second, compartmentalization affects where MMPs function by influencing their location, access to substrates, and interactions with other proteins. Third, pro-enzyme activation ensures that MMPs remain inactive until needed. Finally, enzyme inhibition prevents excessive activity, helping to maintain balance in the extracellular matrix (51,52).

The dysregulation of MMP activity drives the development of various pathologies, broadly categorized into three groups: (1) tissue destruction, (2) fibrosis, and (3) matrix weakening. Overexpression of MMPs is involved in several diseases. In cancer, MMPs help tumors to invade and metastasize by breaking down ECM barriers and promoting the formation of new blood vessels (angiogenesis). In arthritis, excessive MMP activity degrades cartilage, leading to joint damage and inflammation. In cardiovascular diseases, MMPs contribute to vascular remodeling and the progression of atherosclerosis by degrading the structural components of blood vessels (51,53,54).

MMP inhibitors like Batimastat and Marimastat were developed, but their clinical success was hindered by lack of specificity and side effects, particularly musculoskeletal pain. Similar issues led to the discontinuation of the development of other inhibitors, such as Tanomastat and MMI-270 (55). Ongoing research aims to develop more selective MMP inhibitors (MMPIs) to better understand the complex regulation of MMP activity to enhance therapeutic outcomes (56).

1.8.1 MMP-2 and its role in cancer progression

MMP-2 (gelatinase A) plays a critical role in degrading type IV collagen, a major component of the basement membrane. While this function is essential for normal physiological processes, in cancer, the dysregulation of MMP-2 drives tumor progression, invasion, and metastasis (57).

Elevated levels of MMP-2 have been observed in various cancers, where its activity is associated with increased malignancy and poor prognosis (58,59).

During metastasis, MMP-2 facilitates the early stages of tumor invasion by breaking down the basement membrane, allowing cancer cells to breach this barrier and invade surrounding tissues. This degradation is a key step in the metastatic cascade, enabling cancer cells to migrate and establish secondary tumors in distant organs.

In addition to promoting tumor invasion, MMP-2 also plays a significant role in angiogenesis, the formation of new blood vessels, which is crucial for supplying growing tumors with oxygen and nutrients. By degrading ECM components and releasing sequestered growth factors such as Vascular Endothelial Growth Factor A (VEGFA) (60).

Over the past two decades, MMP-2 has been recognized as one of the most critical MMPs in glioblastoma multiforme (GBM)—the most common and aggressive primary brain tumor, characterized by high mortality rates and resistance to conventional therapies (61–65).

1.8.2 Chlorotoxin targeting MMP-2

Ongoing research focuses on two main ways to use MMP-2 in drug development: direct inhibition and targeting for therapeutic delivery or precision surgery. Inhibition strategies aim to suppress MMP-2 activity, with miniprotein-based drugs emerging as promising candidates. Alternatively, MMP-2 can serve as a target for therapies such as antibody-

drug conjugates (ADCs) or radioligand therapies, enabling selective drug delivery to MMP-2-expressing cells (61).

Chlorotoxin (CTX) is a 36-amino acid, cysteine-rich peptide/miniprotein, derived from the venom of the Deathstalker scorpion (*Leiurus quinquestriatus*) (**Figure 8.**). CTX shows high selectivity for glioma and neuroectodermal-origin cancer cells while sparing healthy tissues (66–69). CTX binds MMP-2's collagen-binding domain with an IC_{50} of 115 nM, inhibiting its activity and making it a promising candidate for treating high-grade gliomas and other MMP-2-elevated tumors. (70).

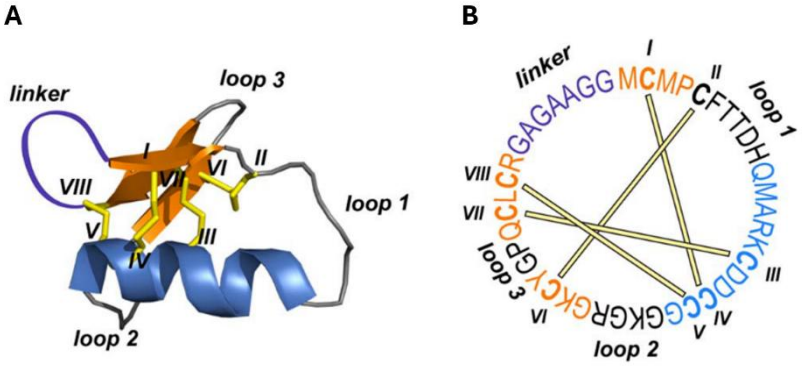

Figure 8. *Structure of Chlorotoxin.* ***(A)*** *The three-dimensional structure of chlorotoxin (PDB: 1CHL) highlights key structural features: disulfide bonds are depicted in yellow stick format, the β-sheet is shown as orange arrows, and the α-helix is represented in blue.* ***(B)*** *The sequence representation of cyclic chlorotoxin illustrates disulfide bond connectivities with yellow lines, and cysteine residues are labeled using Roman numerals (I–VIII). An additional sequence (linker) specific to the cyclic form is shown in violet (67).*

One of the primary challenges for glioblastomas is the difficulty in clearly defining tumor boundaries during surgery. MMP-2-targeting agents like chlorotoxin could help address this issue by not only inhibiting the enzyme that drives tumor invasion but also by supporting real-time tumor visualization (71,72). Tozuleristide (BLZ-100), a synthetic peptide derived from CTX and conjugated to a near-infrared fluorescent dye, allows real-time tumor imaging during surgery. This helps surgeons better differentiate cancerous tissue from healthy tissue, leading to more complete tumor removal and potentially reducing recurrence. Tozuleristide has shown promise in brain tumor studies, particularly in glioblastoma (73).

Among the targets of CTX, MMP-2 stands out as the most significant and well-validated. Although initially believed to target chloride channels like CLC3 (74), CTX was later

shown to bind molecules such as MMP-2, annexin A2 (ANX-2), and neuropilin-1 (NRP-1). However, its binding specificity remains unclear and is a subject of ongoing debate. Some studies failed to confirm a direct interaction between the fluorescently-labeled Cy5.5-CTX and recombinant MMP-2 (75), while others suggest ANX-2 or NRP-1 as alternative targets (76,77). Conflicting data on the behavior of native versus recombinant CTX further complicates the picture. This lack of specificity not only raises questions about its molecular interactions but also introduces potential safety risks, as off-target effects could lead to toxicity or reduced therapeutic efficacy.

1.9 Potassium channels as promising therapeutic targets

Potassium ion channels form the largest and most diverse group of ion channels, with >80 known K^+ channel genes in mammals (**Figure 9.**). Their primary functions include setting and stabilizing the resting membrane potential in most cells and contributing to the repolarization phase of action potentials in excitable cells. All K^+ channels are built from subunits that form either a classic tetrameric structure (4P) or a similar 2x2P structure in two-pore domain K^+ (K2P) channels. These subunits can form homomers or heteromers, creating a wide variety of channels. While they share a conserved K^+ selectivity filter, their gating mechanisms vary depending on their role, responding to stimuli such as voltage (voltage-gated K^+ channels, Kv), calcium (calcium-activated K^+ channels, KCa), various cellular signals (inwardly rectifying K^+ channels, Kir), or temperature and mechanical stress (K2P) (78–81).

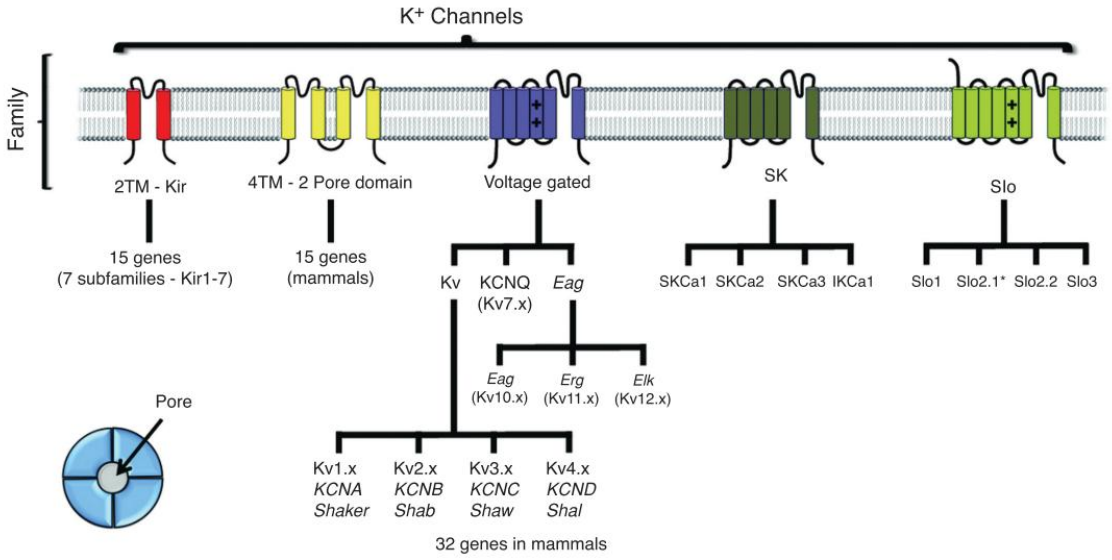

Figure 9. *Subunit structure of potassium channels families. Potassium channels are categorized into four main families based on structure and gating mechanisms: inwardly rectifying (Kir), two-pore domain (K2P), voltage-gated (Kv), and calcium-activated (KCa, including SK and Slo channels). These families consist of over 80 genes in mammals, with conserved K^+ selectivity filters and diverse activation mechanisms, contributing to their broad physiological functions (82).*

1.9.1 Structure, diversity, and the role of Kv1.x subfamily

Kv are divided into conductive and non-conductive (silent) groups. Conductive channels include Kv1.x, Kv2.x, Kv3.x, Kv4.x, Kv7.x, Kv10.x, Kv11.x, and Kv12.x subunits, while non-conductive subunits (Kv5.x, Kv6.x, Kv8.x, and Kv9.x) require heteromerization with Kv2.x subunits to form functional channels. A single cell may express multiple Kv channel types, in homo- and/or heterotetrameric forms, resulting in varied biophysical properties (83). The function of Kv channels is further diversified by auxiliary proteins such as Kv beta subunits (Kvβ), potassium channel interacting proteins (KChIP), potassium voltage-gated channel subfamily E regulatory subunits (KCNE), and calmodulin, as well as by alternative splicing and post-translational modifications.

The Kv1.x (Shaker) subfamily plays a critical role in regulating cellular excitability across various tissues, forming tetrameric channels with subunits held together by non-covalent bonds. Each subunit contains six transmembrane helices (S1-S6), connected by intracellular and extracellular loops, with the pore-forming region located between the S5

and S6 helices. This also feature a turret and filter (pore loop) region, which extends into the extracellular space and plays a role in interacting with pore-blocking toxins (**Figure 10.**). The VSD, found in the S1-S4 helices, detects changes in membrane potential and regulates the channel's opening and closing, which also binds gating-modifying ligands, giving further functional versatility to the Kv1.x subfamily. This structural complexity, combined with their functional diversity, makes Kv1.x channels critical for the proper functioning of many different cell types (84–86).

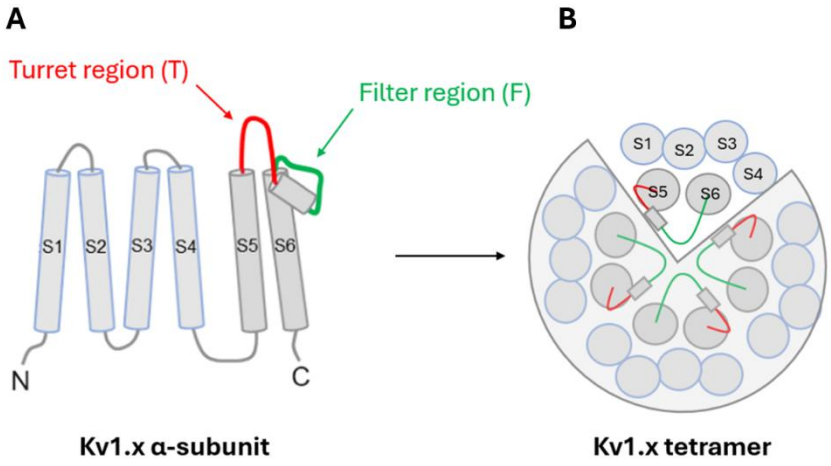

Figure 10. *Structure of Kv1.x channels.* ***(A)*** *Side view of a Kv1.x α-subunit, showing six transmembrane segments (S1–S6), with the voltage-sensing domain (S1–S4) and the pore domain (S5–S6). The turret (T, red) and filter (F, green) regions are located between S5 and S6 and extend extracellularly.* ***(B)*** *Top view of the Kv1.x tetramer, illustrating the arrangement of four subunits forming a central pore, with turret and filter regions contributing to inhibitor binding.*

- Kv1.1 is predominantly found in neurons, where it regulates action potential propagation and controls cellular excitability. Mutations in Kv1.1 can lead to neurological disorders like episodic ataxia type 1 (87,88).
- Kv1.2, expressed in both the central and peripheral nervous systems, is crucial for shaping the frequency of action potentials and modulating synaptic transmission. Dysfunction in Kv1.2 has been linked to seizure disorders and motor impairments (89–91).

- Kv1.3 plays a significant role in immune responses, being primarily expressed in immune cells such as T cells. It is a key therapeutic target for autoimmune diseases, including multiple sclerosis and psoriasis (92–95).
- Kv1.4, found mainly in cardiac and neuronal tissues, helps controlling repetitive firing in neurons by facilitating rapid recovery after action potentials (96,97).
- In the heart, Kv1.5 is vital for the repolarization of atrial myocytes, which is essential to maintain a normal heart rhythm. Dysfunction or mutations in Kv1.5 are associated with atrial fibrillation (98,99).
- Kv1.6, Kv1.7, and Kv1.8 represent important but less extensively studied members of the Kv1 potassium channel family, each uniquely contributing to the regulation of cellular excitability across various tissues (82).

1.9.2 Kv1.3 channel and its role in T cells

Kv1.3 influence cell proliferation by at least three models: the membrane potential model, voltage-sensing model, and channellosome balance model (100).

Among these, the flux-dependent membrane potential model is the most well-established. Unlike other cells, human T cells mainly express Kv1.3 and KCa3.1 potassium channels in homotetrameric form, making these channels particularly attractive targets for therapeutic intervention over the past two decades (92,101–106).

In this model, following T cell receptor (TCR) activation, Ca^{2+} is released from intracellular stores, which triggers the entry of Ca^{2+} from the extracellular space via Calcium Release-Activated Calcium (CRAC) channels such as Orai1. This increase in Ca^{2+} levels activates KCa3.1 channels promoting K^+ efflux, while the resulting depolarization activates homotetrameric Kv1.3 channels that also contribute to the K^+ efflux. The orchestrated activation of these channels leads to the total K^+ efflux, balancing the Ca^{2+} influx, stabilizing the membrane potential and consequently enabling a sustained Ca^{2+} signal (**Figure 11.**).

DOI:10.14753/SE.2025.3224

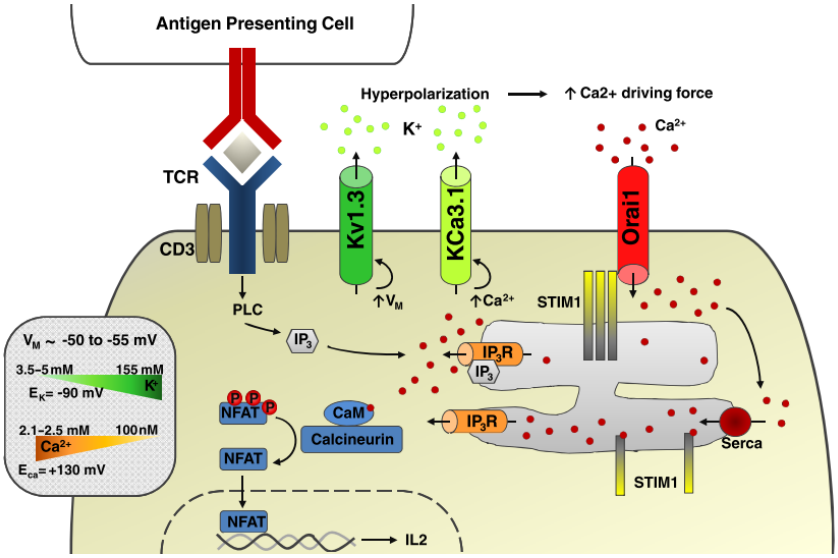

Figure 11. *The membrane potential model of T cell proliferation. TCR activation triggers Ca^{2+} influx via Orai1, balanced by K^{+} efflux through Kv1.3 and KCa3.1 channels. This maintains membrane potential, enabling sustained Ca^{2+} signaling, NFAT activation, and IL-2-driven T cell proliferation (100).*

The sustained Ca^{2+} signal initiates several downstream signaling pathways essential for T cell responses. One key pathway involves the activation of the Ca^{2+}-calmodulin complex, which subsequently activates the phosphatase calcineurin. Calcineurin dephosphorylates the transcription factor NFAT (Nuclear Factor of Activated T cells), allowing it to translocate into the nucleus. Inside the nucleus, NFAT binds to promoter regions of genes involved in cytokine production and T cell proliferation, leading to the activation of genes necessary for these processes (100,107).

The expression of Kv1.3 and KCa3.1 potassium channels in human T cells evolves during activation and differentiation, though not all T cells rely equally on both channels. Initially, T cells upregulate KCa3.1 upon antigen activation, but with repeated antigen stimulation, they display a transition to upregulate Kv1.3 (**Figure 12.**).

DOI:10.14753/SE.2025.3224

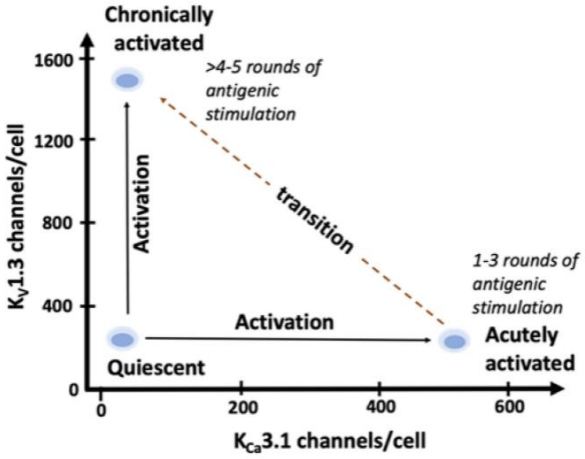

Figure 12. *The expression levels of Kv1.3 and KCa3.1 channels per T cell in quiescent, acutely activated (1–3 rounds of antigenic stimulation) and chronically activated (>4–5 rounds of antigenic stimulation) states (108).*

T cells are key regulators of the immune system, balancing protective immunity and excessive inflammation. Acutely activated T cells are KCa3.1-dependent that support immune homeostasis, while chronically reactivated Kv1.3-dependent T cells drive uncontrolled inflammation. This distinction underscores the importance of Kv1.3 as a therapeutic target in chronic inflammatory diseases (108–111).

1.9.3 Impact of Kv1.3 ^{high} T cells is chronic inflammatory diseases

Persistence of stimulus/antigen and/or relative deficiency of counter-regulatory mechanisms results in local immune cell infiltration and chronic activation. Chronic activation of T cells against innocuous or auto-antigens can lead to immune inflammation and autoimmunity. In chronic inflammatory diseases, disease-associated auto-reactive T cells repeatedly stimulated by autoantigens exhibit high Kv1.3 expression. In recent years, the presence of Kv1.3^{high}, KCa3.1^{low}, CR7^{negative} effector memory T (TEM) cells has been isolated from the site of inflammation in several autoimmune diseases. Additionally, disease-associated autoreactive T cells from patients with multiple sclerosis, type 1 diabetes, and rheumatoid and psoriatic arthritis, pancreatic islets, psoriasis plaques, alopecia areata hair roots and atopic dermatitis lesions have been shown to exhibit this phenotype (**Table 2.**) (105,109,112,113).

Table 2. *Kv1.3-related disorders and the channel's role in pathogenesis. Chronic inflammatory diseases are associated with elevated Kv1.3 expression in autoreactive effector memory T cells (TEM). These Kv1.3^{high} TEM cells infiltrate affected tissues contributing to inflammation and autoimmunity across multiple conditions including multiple sclerosis, psoriasis, and type 1 diabetes. (114).*

Disease	Kv1.3 alteration	Details about disease
Chronic inflammation		
Multiple sclerosis	↑ T_{EM} cells	Self-reactivity of T_{EM} cells in CNS. Demyelination
Psoriasis	↑ T_{EM} cells	Self-reactivity of T_{EM} cells in skin
Rheumatoid arthritis	↑ T_{EM} cells	Self-reactivity of T_{EM} cells in joints
Systemic lupus erythematosus	↑ T_{EM} cells	Systemic self-reactivity of T_{EM} cells. Diverse symptoms
Type I diabetes mellitus	↑ T_{EM} cells	Self-reactivity of T_{EM} cells in pancreas. Destruction of β-cells
Crohn's disease	↑ T_{EM} cells	Self-reactivity of T_{EM} cells in gastrointestinal tract
Alopecia areata	↑ T_{EM} cells	Self-reactivity of T_{EM} cells in hair follicles
Vasculitis	↑ T_{EM} cells	Self-reactivity of T_{EM} cells in blood vessels
Allergic contact dermatitis	↑ T_{EM} cells	Immune over reactivity to some external allergens (i.e. nickel)

The key role of Kv1.3^{high} T cells are supported by evidence from multiple animal models of autoimmune and inflammatory diseases, where miniprotein and small molecule Kv1.3 inhibitors have been successfully used to alleviate disease symptoms (115). Such models include chronic relapsing-remitting experimental autoimmune encephalomyelitis (CR-EAE) and adoptive EAE, delayed-type hypersensitivity (DTH), pristane-induced arthritis (PIA) (102), allergic contact dermatitis (116), spontaneous autoimmune diabetes (105), allergic asthma (117) and alopecia areata (118).

Despite significant advances in the therapeutic developments targeting autoimmune and chronic inflammatory diseases, lack of safe and effective treatment still poses a high, unmet need (119).Therefore, developing drugs that selectively target Kv1.3 channels, without affecting KCa3.1 or closely related homologs such as Kv1.1 and Kv1.2, offers significant potential for creating precise targeted immunomodulatory therapies with fewer side effects.

1.9.4 Diverse group of Kv1.3 inhibitor miniproteins

For the past two decades, extensive efforts have been made to develop selective Kv1.3 inhibitors with an immune-sparing mechanism of action (MoA). However, this has proven challenging due to the high homology between Kv1.3 and closely related channels, mainly Kv1.1, and Kv1.2 (26,30,120–125).

An impressive array of miniproteins from scorpion venom and sea anemones can block Kv1.3. These peptides function as physical pore blockers, binding within a vestibule at the external entrance of the channel pore (126).

DOI:10.14753/SE.2025.3224

Two primiary interactions anchor these peptides in Kv1.3's external vestibule. One critical interaction involves a lysine residue (e.g., Lys23 in HsTX1[R14A]; Lys22 in ShK) that protrudes into the channel's selectivity filter, effectively occluding it like a cork in a bottle. Many peptides also feature a "functional dyad" consisting of this critical lysine and a neighboring aromatic or aliphatic residue (e.g., Tyr21 in HsTX1[R14A], Tyr23 in ShK), which is essential for channel blockage (**Figure 13.**) (127).

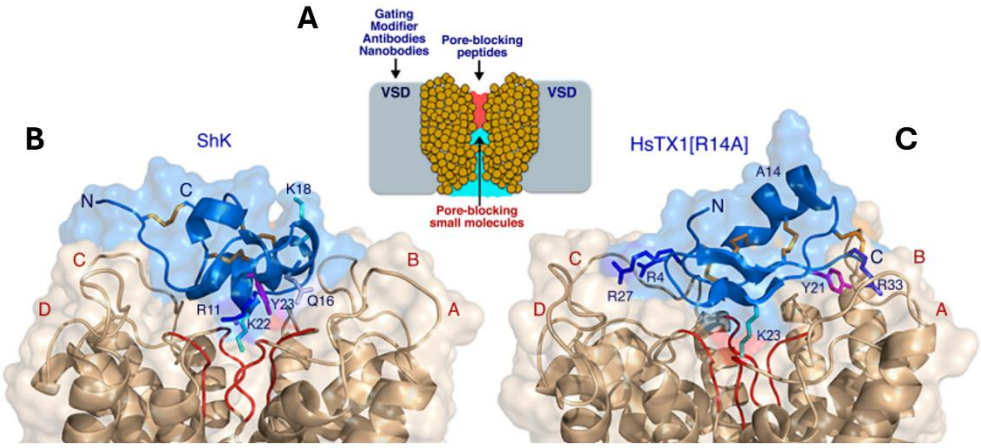

Figure 13. *Blockade of Kv1.3 channel by different mechanisms.* ***(A)*** *Represents two ways of channel blockade: voltage gating modification and pore blocking.* ***(B, C)*** *The pore region involved in toxin binding. Shows ShK and HsTX1[R14A] binding to Kv1.3 (127).*

Secondary interactions also help anchor these peptides in Kv1.3's vestibule, enhancing potency to picomolar levels. For example, Arg11 in ShK interacts with Asp386 in mouse Kv1.3 at the base of the vestibule. Some Kv1.3-blocking peptides, such as α-KTx18.1, lack the traditional functional dyad but still use a lysine side chain (e.g., Lys34 in α-KTx18.1) to block Kv1.3, regardless of its position within the peptide sequence (128–130).

These venom-derived miniproteins did not evolve to specifically target mammalian receptors of therapeutic interest. For example, the sea anemone toxin ShK blocks Kv1.3 at low picomolar concentrations but also affects Kv1.1, Kv1.6, and KCa3.1 channels with similar potency. Scorpion toxins like Kailiotoxin-1 (KTX1), Hongotoxin-1 (HgTX1), and Maurotoxin (MTX) inhibit Kv1.3 in the picomolar-nanomolar range, but they also block off-target channels such as Kv1.1 and Kv1.2 with high affinities. Vm24, a toxin isolated from the venom of *Vaejovis mexicanus smithi*, is the most potent Kv1.3 inhibitor to date

with a half-maximal inhibitory concentration (IC50) of 3 pM. However, it has limited selectivity for Kv1.3 over Kv1.2, KCa3.1, and Kv1.1 channels and begins to block these channels in subnanomolar concentrations. Selectivity issues can lead to severe side effects, limiting the clinical benefits of Kv1.3 inhibition (131–134).

The first attempt to overcome this limitation, Dalazatide (ShK-186), a moderately selective Kv1.3 inhibitor, was developed. This was based on the finding that ShK-F6CA, a fluoresceinated analogue of ShK, exhibited greater selectivity for Kv1.3 over Kv1.1, unlike ShK-rhodamine. To mimic F6CA, negatively charged L-phosphotyrosine was introduced at the N-terminus of ShK-186, resulting a Kv1.3-specific inhibitor (102,120). Dalazatide completed Phase 1b clinical trials. Extremely low doses (60 μg) significantly reduced plasma levels of inflammation markers and lowered the mean PASI (Psoriasis Area and Severity Index) score in 90% of patients. However, mild side effects like hypoesthesia and paresthesia also occurred in 70-90% of patients. These were likely caused by Dalazatide and/or its metabolite inhibiting off-target channels (e.g. Kv1.1) resulting in dose-limiting toxicity that prevented the demonstration of clinically meaningful efficacy (135).

Several other Kv1.3 channel blocker miniproteins have progressed through the development pipeline in recent years. ZP-9830 (from Zealand Pharma) and Si-544 (from SelectION Therapeutics) are designed to improve selectivity/developability and clinical challenges that Dalazatide encountered (136,137).

1.9.5 Structural challenges in developing KcsA-Kv1.x channel chimeras

Over the past two decades, the bacterial KcsA channel (K channel of Streptomyces A), isolated from Streptomyces lividans, has been established as a crucial model for examining the structure, function, and ligand interactions of Kv1.x channels. Its relatively straightforward production via bacterial recombinant expression systems has made it particularly useful. The KcsA channel is a homotetramer, with each subunit comprising two transmembrane helices (TM1 and TM2) connected by a pore loop. Structurally, it resembles the pore domain (S5–S6) of Kv1.x channels (138,139).

Researchers successfully created a hybrid construct by transferring the turret region of the human Kv1.3 to the corresponding part of the KcsA protein. Turret-only KcsA-Kv1.3 (T-only KcsA-Kv1.3) was expressed recombinantly and demonstrated the ability to bind

DOI:10.14753/SE.2025.3224

radiolabeled peptide toxins targeting the native Kv1.3 channel (140). Following this, other Kv1.x subfamily members were also expressed in T-only chimeric forms (141,142). Utilizing the T-only KcsA-Kv1.3 chimera in high-throughput screening led to the identification of a peptide, called Mokatoxin-1 (moka1), with a high binding affinity for Kv1.3 and promising selectivity (30).

However, it was found that not only the turret region but also part of the filter region is essential for selective ligand binding (27,131,141,143–147). This realization highlighted the limitations of T-only chimeras to accurately predict the binding affinities of potential ligand molecules. Previous attempts to produce active chimeras, where "active" refers to tetramers adopting the native conformation of wild-type KcsA, have been unsuccessful. Incorporating both the turret and filter regions (T+F) of human Kv1.x channels in heterologous expression systems resulted in poor expression and improper monomer assembly, leading to defective tetramers (**Figure 14.**).

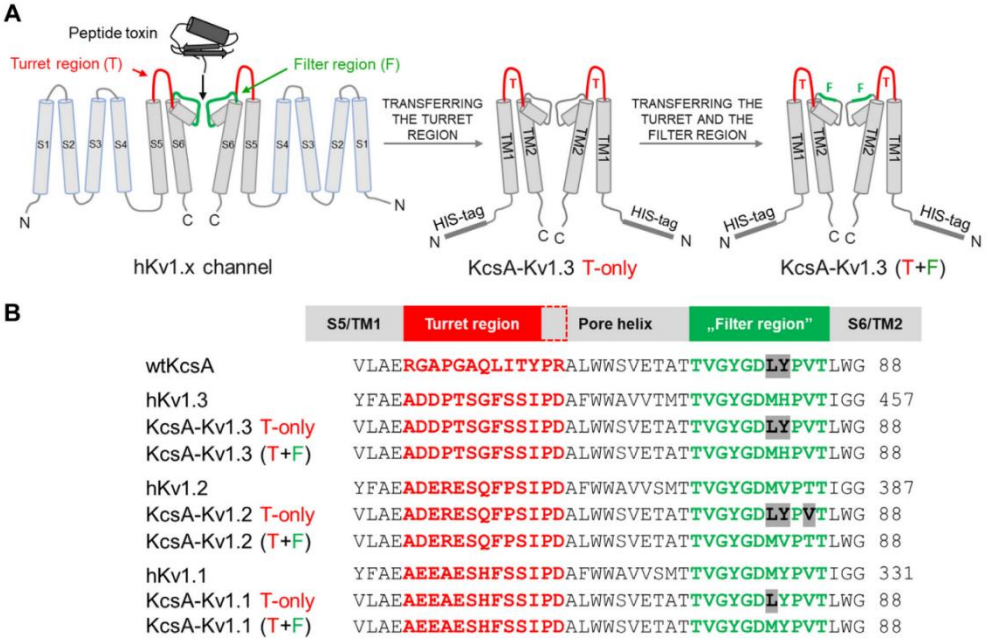

Figure 14. *The subunit structure and sequence of the two distinct versions of the KcsA-Kv1.x chimeras compared with the human Kv1.x channels.(**A**) The structural features of human Kv1.x (hKv1.x) channel pore domains and their interactions with pore-blocking peptide toxins are highlighted in red (turret region) and green (filter region).In hKv1.x channels, the six transmembrane helices are labeled S1 to S6, whereas in the chimeric KcsA-Kv1.x proteins, the two transmembrane helices are labeled TM1 and TM2. Both the T-only and T+F chimeras include an N-terminal 6× His-tag. (**B**) A comparative list*

presents the amino acid composition of the turret and filter regions in WT KcsA, human Kv1.1-3 channels, and the turret-only and turret-filter chimeras. The number following each sequence indicates the position of the last amino acid shown. Amino acid differences in the filter region among the native protein, turret-filter chimera, and turret-only chimera are shaded in gray. Abbreviations: C, C-terminal; F, filter; N, N-terminal; T, turret (138).

Therefore, the successful transfer of the filter region along with the turret region would be the key to enhance ligand binding and mimic human channel behavior.

DOI:10.14753/SE.2025.3224

2 OBJECTIVES

The **main goal** of my thesis was to develop and optimize screening assays for two model systems representing separate drug discovery projects at VRG Therapeutics. Each system required a distinct approach due to unique ligand-target combination. A **secondary focus** was to adapt these assays for high-throughput applications, enabling their use in future studies to discover new miniprotein drug candidates.Our aims were as follows.

Model system I.: CTX targeting MMP-2

1. **Development of microbead-based screening assays**
    - Characterization of chlorotoxin (CTX) variants.
    - Resolving conflicting data of CTX's targets and selectivity.
2. **Adaptation of screening assays for high-throughput applications**
    - Demonstrating that CTX can be displayed on phages.
    - Confirming that phage-displayed CTX retains binding properties of native CTX, supporting future optimization for glioblastoma treatment and diagnostics.

Model system II.: Miniprotein scaffolds targeting Kv1.3

3. **Designing and optimizing humanized KcsA-Kv1.x chimeras**
    - To overcome limitations of previous humanized T-only KcsA-Kv1.x channels.
    - To ensure scalability of solid-phase binding assays.
4. **Identification of key miniprotein scaffolds targeting Kv1.3**
    - To obtain miniprotein ligands for KcsA-Kv1.x chimera characterization
    - To select promising miniprotein candidates for future optimization by phage display
5. **Optimization of microplate-based screening assays (ELISA)**
    - Validating T+F KcsA-Kv1.x chimeras as reliable screening targets.
    - Assessing predictivity of T+F KcsA-Kv1.3 binding for human Kv1.3 channel blocking.
6. **Designing biopanning experiments**
    - Demonstrating system's ability to select Kv1.3-binding sequences from a phage library.
    - Establishing groundwork for high-throughput screening (HTS) and discovery of novel Kv1.3 blocker miniproteins

DOI:10.14753/SE.2025.3224

3 METHODS

3.1 Production of CTX, mCTX, Bs-Tx7, CTX-Cy5 and CTX-A488

3.1.1 Design and expression

Synthetically produced CTX was acquired from Iris Biotech. For clarity, synthetic CTX will be referred to as CTX throughout the thesis.

For the recombinant production of CTX (recombinant CTX will be referred to as rCTX), K27 monolysine mutant CTX (mCTX), and Bs-Tx7, their coding sequences were cloned into a pET-based expression vector as a C-terminal fusion to DsbC (disulfide bond isomerase C) and the recognition site Trp-Glu-Leu-Gln (WELQ) for the staphylococcal serine protease SplB. All constructs harbored an N-terminal 6×His-tag. Sequence verified expression plasmids were transformed into SHuffle T7 Express cells (New England Biolabs, catalog no.: C3029J), and were plated onto LB plates supplemented with 100 μg/ml ampicillin and incubated at 37°C for 16 hours. Next day, several colonies were inoculated into LB broth supplemented with 100 μg/ml ampicillin, and incubated for overnight at 30°C. Next day, the starter culture was inoculated into terrific broth autoinducing medium and was incubated at 30°C for 30 hours.

3.1.2 Protein purification

After expression, cells were harvested by centrifugation and resuspended in lysis buffer (50 mM Tris–HCl, pH 7.5, 300 mM NaCl, and 0.5% Triton X-100), then disrupted by sonication, and the debris was removed via centrifugation at 48,400g. His-tagged DsbC fusion proteins were captured from the soluble fraction by immobilized metal affinity chromatography (IMAC) employing a HiTrap TALON Crude chromatographic column (Cytiva) pre-equilibrated with IMAC A buffer (50 mM Tris–HCl, pH 7.5, 300 mM NaCl, and 30 mM imidazole). The loaded column was washed with IMAC A buffer, then eluted with IMAC B buffer (IMAC A supplemented with 250 mM imidazole). Eluted fractions were analyzed by SDS-PAGE.

From this stage, the purification processes of rCTX, mCTX, and Bs-Tx7 diverged slightly.

rCTX purification

The rCTX-containing eluate was dialyzed overnight at 4°C against 20 mM Tris–HCl (pH 8.0), then loaded onto a HiTrap Q HP column (Cytiva) equilibrated with the same buffer and eluted with a 0–50% linear gradient of 1 M NaCl. After pooling the DsbC–CTX containing fractions, rCTX was cleaved from its fusion partner by adding His-tagged SplB protease (SplB coding expression plasmid was generously provided by Bence Kiss) and tris(2-carboxyethyl)phosphine (TCEP) at a 3:1:1 fusion protein:protease molar ratio, followed by overnight incubation at 25°C. A secondary IMAC step removed His-tagged DsbC and SplB from the mixture, and the flow-through containing rCTX was concentrated using an Amicon Ultra-15 filter (MWCO = 3000 Da, Merck Millipore, catalog no.: UFC9003), with buffer exchanged to 10 mM Tris–HCl (pH 8.0) and 0.5 M NaCl for size-exclusion chromatography (SEC). rCTX was eluted from a HiLoad 16/600 Superdex 30 pg column (Cytiva), and Tris–HCl and NaCl concentrations were reduced by repeated concentration and dilution steps in USP-grade water for injection. Purity and molecular mass were confirmed by HPLC–UV/MS analysis.

mCTX purification

Eluted IMAC fractions containing DsbC–mCTX fusion protein were pooled, then the protein solution was dialyzed against 20 mM Hepes (pH 7.5). Post-dialysis, SplB and TCEP were added in the same molar ratio and incubated overnight at 25°C. Cation exchange chromatography on a HiPrep SP HP column (Cytiva), equilibrated with 20 mM Hepes (pH 7.5), was used to remove contaminants, with mCTX eluted in 20 mM Hepes (pH 7.5) and 600 mM NaCl. The eluate was concentrated using a Pall Microsep Advance filter unit (MWCO = 1000 Da, Pall Life Sciences, catalog no.: MCP001C41).

mCTX underwent further purification via size-exclusion chromatography on a HiLoad 16/600 Superdex 30 pg column equilibrated with 20 mM Hepes (pH 7.5) and 0.15 M NaCl. Buffer and salt concentrations were reduced by repeated concentration and dilution steps in USP-grade water for injection, with purity and mass verified by HPLC–UV/MS.

Bs-Tx7 purification

The DsbC–Bs-Tx7 fusion protein was dialyzed against 50 mM Na_2HPO_4 (pH 7.0), then treated with SplB and TCEP under the same conditions. The pH was adjusted to 4.2 with citric acid for cation exchange chromatography. After loading and extensive washing, Bs-Tx7 was eluted from a HiPrep SP HP column (Cytiva) with 50 mM Na_2HPO_4 (pH 4.2)

and 700 mM NaCl, concentrated, and further purified by size-exclusion chromatography employing a HiLoad 16/600 Superdex 30 pg column equilibrated with 50 mM Na_2HPO_4 (pH 4.2) and 0.15 M NaCl, followed by RP-HPLC on a Jupiter 300 C5 column (Phenomenex). Purity and molecular mass were confirmed by HPLC–UV/MS analysis. Protein concentrations of the purified CTX and Bs-Tx7 samples were determined by absorbance at 214 nm, using an extinction coefficient calculator. CTX aliquots were lyophilized and stored at −80°C.

CTX-Cy5 and CTX-A488 *purification*

Cyanine 5-labeled CTX (CTX-Cy5) was synthesized at Vichem Chemie Research Ltd by conjugation of CTX with cyanine 5 N-hydroxysuccinimide ester (Lumiprobe, catalog no.: 13010) and purified via RP-HPLC–UV/MS. Analytical RP-HPLC and tandem MS revealed a mixture of monoconjugates at lysine residues 15, 23, and 27, with approximate proportions of 20%, 38%, and 42%, respectively. Alexa Fluor 488-labeled CTX (CTX-A488) was similarly synthesized with Alexa Fluor 488 tetrafluorophenyl ester (ThermoFisher Scientific, catalog no.: A37570).

3.2 Flow cytometry-based binding assays

3.2.1 IgG coated bead binding test

The Ig-coated bead assay operates by immobilizing target proteins through target-specific rabbit IgG antibodies on MagnaBind Goat Anti-Rabbit IgG microbeads (ThermoFisher Scientific, catalog no.: 21356), which are pre-coated with goat anti-rabbit antibodies. A fluorophore-labeled ligand binds to the target protein, and fluorescence intensity is subsequently measured via flow cytometry. Each reaction used 1 µl of microbeads (diameter: 1–4 µm), followed by three washing cycles where the beads were resuspended in 2 ml of Dulbecco's PBS (DPBS, Sigma), placed in a magnetic concentrator (DynaMag-5; ThermoFisher Scientific), and the supernatant was discarded after 10 minutes. Beads were incubated at 4°C for 1 hour in 50 µl DPBS containing a rabbit antibody specific to the target protein, diluted at 1:100. The polyclonal anti-MMP-2 antibody (Sigma, catalog no.: HPA001939) used targets amino acid positions 445 to 575 of human MMP-2 protein (NP_004521.1). Recombinant MMP-2 proteins tested included the proenzyme expressed in HEK293 cells (catalog no.: Enz-100 with a C-terminal His-tag) and the mature active enzyme (ProSpec, catalog no.: Enz-769, aa 110-660, N-terminal His-tag) expressed in *E.*

coli. For NRP1, the target protein was the recombinant human NRP1 isoform b (NP_001019799.2) with a C-terminal His-tag (Sino Biological; catalog no.: 10011-H08H), and the anti-NRP1 antibody was obtained from ThermoFisher Scientific (catalog no.: PA5-96531).

Following antibody coating, the beads were washed three times and incubated overnight at 4°C in 50 µl DPBS containing the target protein at 0.16 µM, corresponding to 10 µg/ml for active MMP-2 (MW = 62 kDa). Blocking to prevent nonspecific binding was unnecessary. For testing fluorophore-labeled substances (e.g., CTX-Cy5 or CTX-A488), the target protein-coated beads were resuspended in 50 µl of test solution at the desired concentration, prepared by diluting a 100 µM stock in DPBS. After a 1-hour room-temperature incubation with the test solution, beads were washed, resuspended in 2 ml DPBS, and prepared for flow cytometry.

In competitive displacement assays, beads were first incubated in 50 µl test solution with the specified concentration of unlabeled test substance for 1 hour at room temperature. Then, 50 µl DPBS containing 2 µM labeled CTX (CTX-Cy5 or CTX-A488) and the specified unlabeled concentration were added, creating a final 1 µM concentration of labeled CTX and the displacing ligand. Beads were incubated for an additional hour, washed, resuspended in 2 ml DPBS, and prepared for flow cytometry.

Flow cytometric analysis was performed on a MACSQuant Analyzer 10 (Miltenyi Biotec) with a 635 nm red laser to measure Cy5-labeled ligand binding in the R1 channel, and a 488 nm blue laser for A488-labeled ligand binding in the B1 channel, using pulse area mode. Each sample utilized a 200 µl aspiration volume with gentle mixing, collecting 10,000 events at a maximum rate of 500 events/second. Gating was applied consistently around the main bead population to exclude doublets and multiplets based on a forward versus side scatter plot of control beads.

Quantitative analysis of labeled ligand binding utilized the median fluorescence intensity of gated events, normalized to negative control beads (beads not binding target proteins but exposed to 1 µM labeled CTX). Relative affinities were assessed by plotting RFI values against log concentrations and determining the half-maximal effective concentration (EC50) through sigmoidal curve fitting. In displacement studies, percent inhibition of labeled ligand binding was calculated, and the relative affinity of unlabeled test substances was assessed by plotting percent displacement against log concentrations,

determining IC50 using the "sigmoidal dose–response (variable slope)" algorithm in GraphPad Prism 8. The equation used for fitting a sigmoidal dose-response curve with a variable slope (often applied to calculate EC50 or IC50 values) is as follows:

$$Y = \text{Bottom} + \frac{\text{Top}-\text{Bottom}}{1+10^{(\text{LogEC50}-X)\,\cdot\,\text{Hillslope}}} \qquad (3.1)$$

- Y is the response (e.g., fluorescence intensity or percent inhibition).
- Bottom is the minimum asymptote of the curve.
- Top is the maximum asymptote of the curve.
- LogEC50 (or LogIC50 for inhibition curves) is the logarithm of the concentration at which half-maximal effect is achieved.
- X is the log concentration of the ligand or inhibitor.
- HillSlope reflects the steepness of the curve. A higher slope indicates a steeper transition between the minimum and maximum response.
- The software calculated 95% confidence intervals, and differences between EC50 or IC50 values from simultaneous curve fits were tested for significance via extra sum-of-squares F test with alpha = 0.05.

3.2.2 Cobalt-coated bead binding test

The cobalt-coated bead binding assay was used to measure binding intensities of CTX-Cy5 or phage-displayed ligand proteins to various target proteins. This assay anchors His-tagged target proteins to cobalt-coated His-Tag Isolation & Pulldown Dynabeads (ThermoFisher Scientific, catalog no.: 10103D), allowing the binding of a fluorophore-labeled ligand (or stained ligand-displaying phages) to the target protein, followed by measurement of bead-bound fluorescence intensity via flow cytometry.

For each reaction, 0.5 µl of beads (diameter = 1 µm) were pipetted into reaction tubes and washed three times. Each wash involved suspending the beads in 2 ml Tris-buffered saline (TBS) with 0.05% Tween-20, placing the tubes in a DynaMag-5 magnetic concentrator, and discarding the supernatant after 10 minutes. Beads were then incubated overnight at 4°C in 50 µl of target protein solution. All target proteins were applied at 0.16 µM (equivalent to 10 µg/ml for active MMP-2, MW = 62 kDa) and dissolved in TBS. Negative control beads were incubated with TBS without target proteins. Target proteins used included MMP2, NRP1, MMP-9, TIMP-2, MMP14, ANX2, αvβ3 integrin, CLC-3,

and human serum albumin, with each specified by NCBI accession number, segment sequence, His-tag position, supplier, and catalog number.

After target protein incubation, the beads were washed three times and blocked for 1 hour at room temperature with 100 μl Casein Blocking Solution (Sigma; catalog no.: B6429), followed by three more washes.

For fluorophore-labeled ligands (e.g., CTX-Cy5), the casein-blocked beads were resuspended in 50 μl of test solution with the labeled test substance and incubated for 1 hour at room temperature. Following incubation, the beads were washed three times, resuspended in 2 ml washing solution, and prepared for flow cytometry.

For phage-displayed ligands, the prepared beads were incubated with phage solution in TBS containing 0.5% bovine serum albumin and 0.05% Tween-20 (TBT) for 1 hour at room temperature. After phage binding, the beads were washed, incubated for 30 minutes at 4°C in 50 μl TBT containing anti-M13 mouse monoclonal antibody (Sino Biological; catalog no.: 11973-MM05) at 1:200 dilution, then washed again and incubated for 30 minutes at 4°C in 50 μl TBT containing Cy5-labeled goat anti-mouse secondary antibody (Abcam; catalog no.: ab6563) at 1:1000 dilution. After three final washes, the beads were resuspended in 2 ml washing solution and prepared for flow cytometry.

Flow cytometry analysis was conducted as described for the Ig-coated bead test, using RFI values from median fluorescence intensities of the beads to quantify binding intensity.

3.3 Kv1.x targeting miniprotein scaffold representatives

The synthetic peptide toxins tested—KTX1 (STK-370), HgTX1 (STH-400), ShK (STS-400), Vm24 (STV-055), and MTX (STM-340)—were obtained from Alomone Labs. These peptide toxins were dissolved in USP-grade water to a concentration of 100 μM, aliquoted, and stored at −20°C.

3.4 Recombinant production of KcsA-Kv1.x screening targets

3.4.1 Design and expression

The coding sequences for full-length wild-type KcsA (UniProtKB/Swiss-Prot: P0A334.1) and the T-only KcsA-Kv1.3 chimeric construct were cloned into the pQE30 vector, using BamHI and PstI restriction sites, with an N-terminal His-tag for ease of purification.

Additional KcsA-Kv1.x chimeric constructs, including KcsA-Kv1.1, KcsA-Kv1.2 (both T-only and T+F versions), and T+F KcsA-Kv1.3, were cloned into the pET45b plasmid using KpnI and HindIII sites, also incorporating an N-terminal 6×His-tag.

The pQE30-based constructs for WT KcsA and the Kv1.3 T-only chimera were transformed into XL1-Blue *E. coli* cells (Agilent, catalog no.: 200249), plated on LB agar with 100 μg/ml carbenicillin and 0.2% glucose, and incubated at 37°C. Colonies were transferred to starter media supplemented with carbenicillin and glucose and grown overnight at 30°C, then the following day inoculated into large scale LB media (with carbenicillin added) and incubated at 37°C. After reaching mid-log phase (A600 of 0.6), the temperature was adjusted to 30°C, 5 mM $BaCl_2$ was added, and protein expression was induced with 1 mM Isopropyl β-D-1-thiogalactopyranoside (IPTG, ThermoFisfer Scientific, catalog no.: AM9464) for 3 hours.

For constructs in pET45b, Kv1.x T-only and T+F chimeras were expressed in C41(DE3) *E. coli* cells (Lucigen, catalog no.: 60341-1-LU). Cells were grown in LB media with carbenicillin and glucose, and upon reaching mid-log phase, the temperature was lowered to 18°C, $BaCl_2$ was added, and expression was induced with 0.1 mM IPTG overnight. Cultures were centrifuged, and cell pellets were stored at -20°C for further processing.

3.4.2 Purification and quality control

Cell pellets were resuspended in lysis buffer (50 mM Tris, pH 8.0, 300 mM KCl, 5% glycerol) with SIGMAFAST protease inhibitor (Sigma-Aldrich) and lysed by sonication. Cell debris was removed by centrifugation, and membrane fractions were pelleted by ultracentrifugation. Membranes were solubilized in buffer with 20 mM n-Dodecyl-beta-maltoside (DDM) (Avanti) and ultracentrifuged again. The supernatant was loaded onto a HiTrap TALON Crude column (Cytiva) pre-equilibrated with washing buffer and connected to an ÄKTA Pure system. Bound proteins were eluted with a linear gradient of elution buffer (containing 250 mM imidazole), and fractions were analyzed by SDS-PAGE.

Fractions containing the target protein were pooled, further purified via size-exclusion chromatography on a HiLoad 16/600 Superdex 200 column (Cytiva) pre-equilibrated with storage buffer and eluted at 1 ml/min. Eluted peak fractions were analyzed by SDS-

PAGE, pooled, concentrated, and quantified by UV absorbance at 280 nm using Expasy's ProtParam tool. Protein samples were aliquoted, flash-frozen, and stored at -80°C.

For functional validation, chimeric proteins underwent phage ELISA with a dilution series of M13 bacteriophage displaying HgTx1, a high-potency inhibitor of Kv1.1, Kv1.2, and Kv1.3 channels. Western blot analysis verified protein expression using a 6×His-tag monoclonal antibody, and NativePAGE analysis further confirmed protein integrity.

3.5 Cells for electrophysiology recordings

Chinese Hamster Ovary (CHO) cells were cultured in Dulbecco's Modified Eagle Medium (DMEM) with high glucose, supplemented with 10% fetal bovine serum (FBS), 2 mM L-glutamine, 100 U/ml penicillin, and 100 µg/ml streptomycin (Invitrogen). The cells were maintained at 37°C in a humidified atmosphere with 5% CO_2 and 95% air and passaged twice weekly after a 5-minute incubation in PBS containing 0.2 g/L EDTA. For experiments, CHO cells were transiently transfected with plasmids encoding human Kv1.1 (hKCNA1 gene) and Kv1.2 (hKCNA2 gene) in the pCMV6-AC-GFP vector (RG211000 and RC222200, OriGene Technologies) using Lipofectamine 2000 (Invitrogen, catalog no.: 11668027), following the manufacturer's instructions. Transfected cells were then cultured under standard conditions.

Twenty-four hours post-transfection, cells were washed twice with 2 ml extracellular solution (ECS, see below) and replated onto 35 mm polystyrene cell culture dishes (Cellstar, Greiner Bio-One) for patch-clamp experiments. GFP-expressing transfectants were identified using a Nikon TE 2000U fluorescence microscope (Nikon) with 455–495 nm and 515–555 nm bandpass filters for excitation and emission, respectively. These cells were used for current recordings, with a co-transfection success rate of approximately 60–70%. Typically, recordings were performed 24–36 hours after transfection.

Human Kv1.3 currents were recorded from activated peripheral blood mononuclear cells (PBMCs) isolated from healthy volunteers 3–4 days post-activation. Mononuclear cells were separated from heparinized peripheral blood using Histopaque-1077 density gradient centrifugation and then washed twice with Ca^{2+}- and Mg^{2+}-free Hanks' solution containing 25 mM Hepes buffer, pH 7.4. The cells were cultured at a density of 0.5×10^6 cells per ml in RPMI 1640 medium supplemented with 10% fetal calf serum (Sigma-Aldrich), 100 µg/ml penicillin, 100 µg/ml streptomycin, and 2 mM L-glutamine. To

enhance Kv1.3 expression, 10 μg/ml phytohemagglutinin A (Sigma-Aldrich) was added to the medium. Cells were gently washed twice with 2 ml ECS before patch-clamp experiments.

3.6 Patch clamp measurements with Kv1.x channels

Conventional whole-cell patch-clamp electrophysiology was employed to record ionic currents. Micropipettes were pulled from GC150F-7.5 borosilicate capillaries (Harvard Apparatus), yielding tip diameters between 0.5 and 1 μm and a resistance of 2 to 8 MΩ in the extracellular solution. Recordings were performed using an Axopatch 200B amplifier connected to a PC with Axon Digidata 1550A data acquisition hardware and pCLAMP 10.7 software. The holding potential was set at -120 mV, and recordings with leak currents exceeding 10% of the peak current were discarded. Experiments were conducted at room temperature (20–24°C). Whole-cell current traces were corrected for ohmic leakage and digitally smoothed with a three-point boxcar filter prior to analysis.

The extracellular (ECS) solution contained 145 mM NaCl, 5 mM KCl, 2.5 mM $CaCl_2$, 1 mM $MgCl_2$, 10 mM Hepes, and 5.5 mM glucose, adjusted to pH 7.35 with NaOH, while the intracellular (ICS) solution contained 140 mM KF, 2 mM $MgCl_2$, 1 mM $CaCl_2$, 11 mM EGTA, and 10 mM Hepes, adjusted to pH 7.22 with KOH. Both ECS and ICS had an osmolarity of 302 mOsM. Native peptides, phage-expressed peptides, and controls were dissolved in ECS with 0.1 mg/ml BSA (Sigma-Aldrich). Bath perfusion was controlled using a gravity-driven micro perfusion system with a flow rate of 0.5 ml/min, with excess fluid continuously removed.

For Kv1.1–Kv1.3 current measurements, voltage steps to +50 mV were applied from a -120 mV holding potential, with peak currents recorded every 15 seconds. Specific protocols included 15 ms depolarizing pulses for Kv1.3, 50 ms stimuli for Kv1.1, and 200 ms pulses for Kv1.2. Positive controls were used at concentrations near their IC50 values (0.3 mM and 10 Mm) tetraethylammonium (TEA^+) for Kv1.1 and Kv1.3, respectively, and 14 nM charybdotoxin for Kv1.2). The remaining current fraction at each concentration was calculated as $I/I0$, where $I0$ is the peak current in the absence of inhibitor and I is the peak current after 2 minutes of peptide or phage perfusion.

3.7 Recombinant production of phages

Phage display test solutions were prepared following standard phage display protocols (148). Phosphorylated and annealed oligonucleotides encoding the peptide construct were ligated into a linearized pAS62 phagemid vector at a vector-to-insert ratio of 1:3. The final phagemid construct included a signal sequence, the peptide of interest, a linker (GSASSATR), and the C-terminal portion of the P3 coat protein (amino acids 216–424 of NP_510891.1). Chemically competent XL1-Blue *E. coli* cells (Agilent, catalog no.: 2022249) were transformed with the ligation product, plated on LB plates supplemented with 100 μg/ml ampicillin, and incubated at 37°C for 16 hours. Clones were sequenced, and a confirmed colony was inoculated into 3 ml of 2YT medium with 100 μg/ml ampicillin and grown at 37°C to mid-log phase.

The culture was then infected with M13KO7 helper phage (New England Biolabs, catalog no.: N0315S) at a phage-to-cell ratio of 10:1 and incubated for 30 minutes at 37°C. Afterward, the culture was transferred to 200 ml of 2YT medium supplemented with 100 μg/ml ampicillin and 25 μg/ml kanamycin and incubated overnight at 37°C. Following incubation, the culture was centrifuged at 8000g for 10 minutes at 4°C. The supernatant was mixed with 40 ml of PEG/NaCl solution (200 g/l PEG-8000, 146.1 g/l NaCl) and incubated for 20 minutes at room temperature. Phages were pelleted by centrifugation at 18,000g for 15 minutes at room temperature. After discarding the supernatant, residual media was removed by a brief centrifugation at 1000 rpm. Phages were resuspended in 4 ml of phage resuspension buffer (TBS with 0.5% BSA and 0.05% Tween-20), and insoluble materials were removed by centrifugation at 18,000g for 10 minutes at 4°C.

The supernatant was divided into four 1.5 ml tubes (4 × 1 ml), precipitated again with 100–200 μl of PEG/NaCl, incubated for 5 minutes, and centrifuged at 12,000g. The pellets were resuspended in small volumes (150–300 μl) of phage resuspension buffer and combined. Phage particle concentrations were determined using a NanoDrop One C spectrophotometer (Thermo Fisher Scientific), with particle concentrations calculated as (A268–A320) × 5 × 10^12 particles/ml (148). The phage stock solution was stored at 4°C.

3.8 Microplate-based ELISA binding assays

3.8.1 Phage binding assay

Phage stock solutions were diluted to working concentration in phage resuspension buffer with 2 mM DDM. For protein immobilization, the following amounts were prepared in a final volume of 50 µl per well: wt KcsA (0.1 µg), T-only KcsA-Kv1.1 (0.005 µg), T+F KcsA-Kv1.1 (0.02 µg), T-only KcsA-Kv1.2 (0.01 µg), T+F KcsA-Kv1.2 (0.1 µg), T-only KcsA-Kv1.3 (0.01 µg), and T+F KcsA-Kv1.3 (0.1 µg). Each protein sample was diluted in 50 µl of storage buffer (20 mM Tris, pH 8.0, 300 mM KCl, 2 mM DDM) and added to the designated wells of a Pierce Clear 96-Well Nickel-Coated Plate (Thermo Fisher Scientific, catalog no.: 15442). The plate was incubated for 1 hour at room temperature on a horizontal shaker at 130 rpm.

Following protein immobilization, the plate was blocked for 1 hour at room temperature with 180 µl per well of TBS-BSA supplemented with 1 mM DDM. Wells were then washed four times with 300 µl of washing buffer (TBS with 0.1% Tween-20) using a Wellwash Versa microplate washer (Thermo Fisher Scientific). A 50 µl solution of phage (in TBS-BSA-Tween with 0.1% Tween-20 and 2 mM DDM) at the desired concentration was added to each well and incubated for 1 hour at room temperature on a horizontal shaker.

After phage incubation, the wells were washed four times with washing buffer. Then, 50 µl of anti-M13 IgG HRP (Invitrogen, catalog no.: MA5-36125) diluted 1:2500 in TBS-Tween (0.1%) was added to each well and incubated for another hour at room temperature. The wells were washed again four times with 300 µl washing buffer per well, followed by the addition of 50 µl per well of 1-Step Ultra TMB-ELISA solution (Thermo Fisher Scientific, catalog no.: 34028). After 5 to 10 minutes, the reaction was stopped by adding 50 µl of 1M HCl. The absorbance was measured at 450 nm using a Byonoy Absorbance 96 Plate Reader (Byonoy GmbH).

3.8.2 Phage competition assay

For protein immobilization, the following quantities were prepared in a final volume of 50 µl per well: T-only KcsA-Kv1.1 (0.005 µg), T+F KcsA-Kv1.1 (0.01 µg), T-only KcsA-Kv1.2 (0.025 µg), T+F KcsA-Kv1.2 (0.0125 µg), T-only KcsA-Kv1.3 (0.01 µg), and T+F KcsA-Kv1.3 (0.1 µg). Each protein sample was diluted in storage buffer. Binding of

specific concentrations of ligand-displaying phages was quantified by measuring light absorbance at 405 nm, similar to a phage ELISA assay. Different concentrations of competing toxin test substances were applied simultaneously to evaluate competition.

The results were expressed as percent inhibition (percent displacement) of indicator phage binding. Relative affinities of the tested toxins were determined by plotting percent displacement against log concentrations and calculating IC50 through sigmoidal curve fitting. The fitting used the "Sigmoidal dose-response (variable slope)" method with the least squares algorithm in GraphPad Prism 8, following equation (3.1).

3.9 Phage-display based solid phase biopanning

Nickel-coated 96-well plate was used to immobilize the T+F KcsA-Kv1.3 target. Wells were coated with T+F KcsA-Kv1.3 at (5 µg/mL concentration), followed by incubation at room temperature for 1 h and blocking with TBS-BSA supplemented with 1 mM DDM to minimize non-specific binding.

Phage-displayed miniproteins Vm24 and DDDKTX1 were prepared and amplified to appropriate titers for biopanning. To validate specific binding, a phage-ELISA was performed with Vm24 phages at an input of 10^10 CFU/well, with detection carried out using an anti-M13 IgG HRP antibody (Invitrogen, catalog no.: MA5-36125). To optimize conditions, Vm24 and DDDKTX1 mixtures were prepared at 10^10 CFU/well, 10^11 CFU/well, and 10^12 CFU/well with a Vm24:DDDKTX1 ratio of 1:10. These mixtures were applied to T+F KcsA-Kv1.3-coated wells and incubated in binding buffer (TBS-BSA-Tween, 0.1% v/v, 2 mM DDM).

The biopanning procedure included incubation of phage mixtures with the immobilized and blocked target, followed by controlled washes with washing buffer (TBS with 0.1% Tween-20) using a Wellwash Versa microplate washer (Thermo Fisher Scientific) to remove non-specific binding. Bound phages were then eluted with 0.01M HCl subsequently neutralized with Tris (1M, pH~11). Eluted phages were quantified by infecting bacterial cells and performing ten-fold serial dilutions for titering. Enrichment was evaluated by comparing phage titers before and after panning. Enrichment ratios and signal-to-noise values were calculated by counting colonies formed from 10 µL droplets at each dilution, using BSA-coated wells as controls.

DOI:10.14753/SE.2025.3224

4 RESULTS

4.1 Characterization of CTX and its variants by bead binding assays

For CTX receptor-binding studies, we used synthetically produced native CTX with a carboxamide C terminus, along with recombinantly produced rCTX and mCTX variants having a free carboxyl terminus. For comparative purposes, we also produced recombinant Bs-Tx7, a CTX-like toxin originally isolated from the venom of the Indian red scorpion (*Buthus sindicus*), which shares 66% sequence identity with CTX (**Figure 15.**).

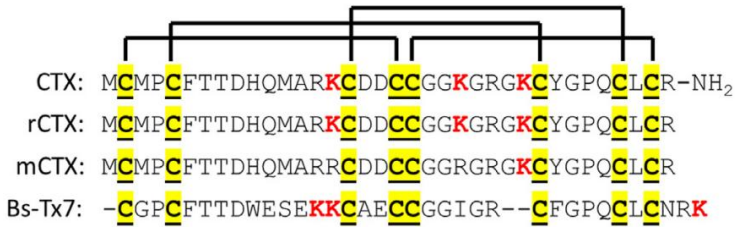

Figure 15. *Amino acid sequences of native and synthetic chlorotoxin having carboxamide C terminus (CTX), recombinantly produced chlorotoxin (rCTX), K27 monolysine mutant chlorotoxin (mCTX), and Bs-Tx7 scorpion toxin. Disulfide bond pattern is also indicated, and plausible conjugation site lysine (K) residues are highlighted in red (149).*

Additionally, we obtained monoconjugated fluorophore-labeled CTX's: CTX-Cy5, which emits in the red wavelength range and offers a high signal-to-autofluorescence ratio and CTX-A488, which emits green but has a lower signal-to-autofluorescence ratio.

To explore the potential direct binding partners of CTX, we designed and validated two distinct flow cytometry-based methods utilizing fluorescently labeled CTX. The first approach, the "**immunoglobulin (Ig)-coated bead binding test**" involves attaching target proteins to MagnaBind™ microbeads using protein-specific IgG antibodies. The second method, the "**cobalt-coated bead binding test**" takes the advantage of the strong affinity between metal ions and His-tagged target proteins.

DOI:10.14753/SE.2025.3224

4.1.1 Ig-coated bead binding test to measure MMP-2 binding

The **Ig-coated bead binding test** was used to study the competitive displacement of red-labeled CTX (CTX-Cy5) and green-labeled CTX (CTX-A488), by different CTX versions to determine their affinities to MMP-2.

Using 1 µM CTX-Cy5 as the displaced ligand, we compared concentration-displacement relationships for unlabeled CTX and Bs-Tx7. Both toxins caused nearly complete displacement of the labeled ligand at the highest concentration tested (30 µM), with well-fitted sigmoidal curves and parallel concentration-displacement trends, suggesting a shared binding site with CTX-Cy5. Bs-Tx7 binds to MMP-2 in a similar manner to CTX but with a 2.6-fold lower affinity, as indicated by the ratio of their IC50 values.

To confirm these findings, we also used 1 µM CTX-A488 as the displaced ligand and compared the relative affinities of CTX, CTX-Cy5, rCTX, and mCTX. The results showed nearly identical affinities for all four test substances, with the most notable finding being that the affinity of CTX for MMP-2 lies between 0.62 and 0.75 µM shown on **Figure 16.**

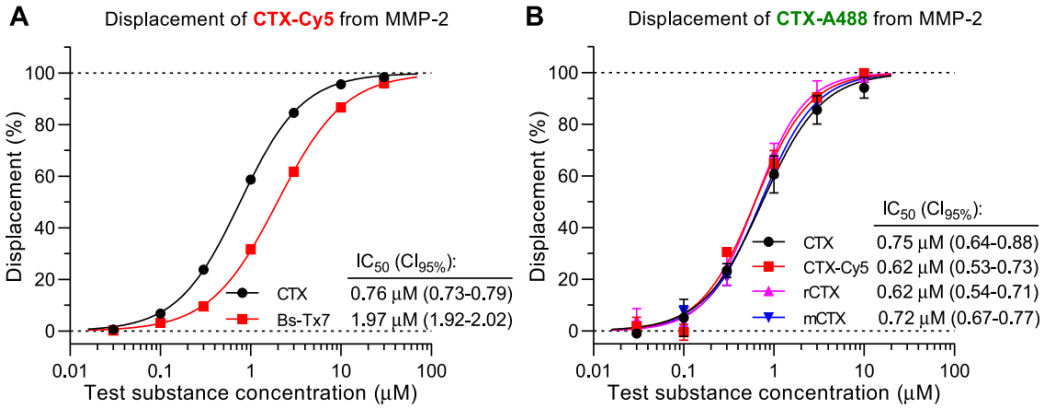

Figure 16. *Comparison of MMP-2 affinities of CTX, CTX analogs and CTX-like compounds in the displacement assay* ***(A)*** *The affinities of chlorotoxin (CTX) and the venom toxin Bs-Tx7 from Buthus sindicus scorpion were assessed via concentration-displacement curves against 1 µM CTX-Cy5. Both lines on the graph represent data from a single set of measurements. A statistically significant difference was observed between the IC50 values of CTX and Bs-Tx7 ($p<0.0001$).* ***(B)*** *The affinities of CTX, mutant CTX (mCTX), recombinant CTX (rCTX), and CTX-Cy5 were compared using concentration-displacement curves against 1 µM CTX-A488. Data are presented as the mean ± SD of*

two independent experiments for each test compound. No statistically significant differences were found among the IC50 values for the four compounds. Confidence intervals for the IC50 values are provided in both panels (A and B) (149).

4.1.2 CTX's target confirmation and HTS preparation

The **cobalt-coated bead binding test** was employed to investigate the binding of 1 µM CTX-Cy5 to a panel of His-tagged target proteins identified as relevant in the literature. These targets included MMP-2, NRP1, MMP-9, TIMP-2, MMP-14, ANX2, αvβ3 integrin (INT), CLC-3, and human serum albumin (HSA) serving as a nonspecific binding control. "His-tag isolation and pulldown" Dynabeads were coated with the aforementioned various His-tagged proteins at a concentration of 0.16 µM each. The target proteins tested included MMP-2, NRP1, CLC-3 chloride channel, TIMP-2, MT1-MMP (MMP14), ANX2, αvβ3 integrin (INT), MMP-9, and human serum albumin (HSA).

The analysis showed that CTX-Cy5 bound to both MMP-2 and NRP1 with similar signal intensities. Lower fluorescence intensity signals were detected for CLC-3 and TIMP-2 compared to MMP-2 and NRP1, indicating weaker binding (**Figure 17.**).

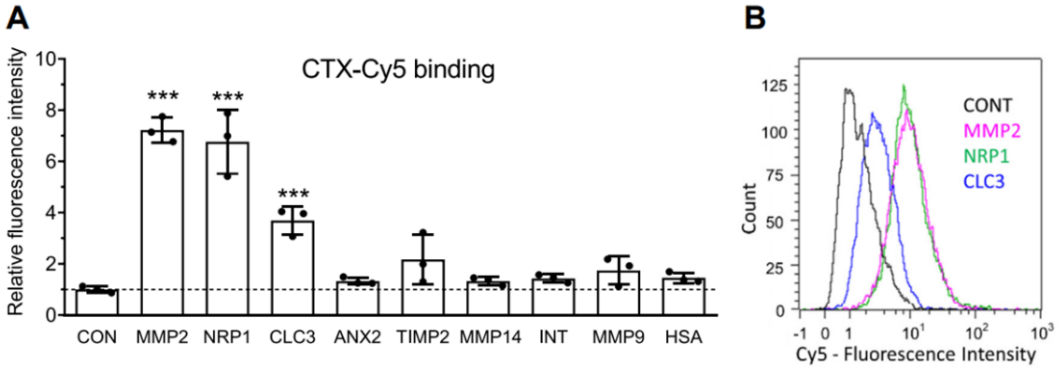

Figure 17. *Binding of CTX-Cy5 to proposed target proteins and human serum albumin* ***(A)*** *Beads were blocked with casein and then stained with 1 µM CTX-Cy5. Control beads (CONT), also blocked with casein, were not exposed to any target proteins prior to staining. The bar graphs display relative fluorescence intensities, calculated from the median fluorescence values of 10,000 events recorded by the flow cytometer. Data are shown as mean ± SD from three independent experiments, with scatter plots superimposed. Statistical significance is indicated by * ($p < 0.05$) and *** ($p < 0.001$) compared to the control group (ANOVA with Dunnett's test).* ***(B)*** *Representative*

histograms show the intensity distributions from the staining experiment described in A (149).

Parallel assays with CTX-displaying phages showed a binding pattern similar to that of CTX-Cy5, with strong interactions observed for MMP-2 and NRP1 and weaker signals for CLC-3 and TIMP-2. The binding patterns observed with CTX-displaying phages mirrored those of labeled CTX, showing similarly strong interactions with MMP-2 and NRP1, and lesser, but significant binding to CLC-3 and TIMP-2 (**Figure 18.**).

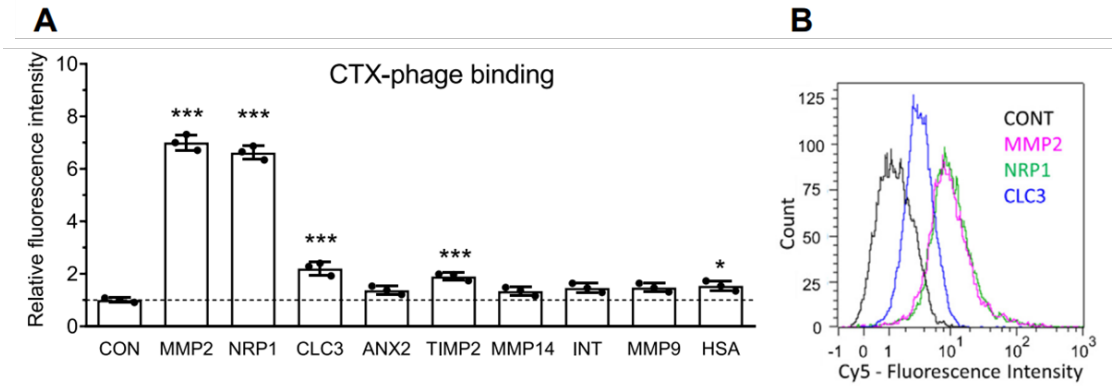

Figure 18. *Binding of CTX-displaying phages to various proposed target proteins and human serum albumin in the cobalt-coated bead test.* ***(A)*** *Beads were blocked with casein, then incubated with CTX-displaying phages (5.5 × 10^14 particles/ml), and stained to detect M13 phage binding. Control beads (CONT) in this part of the experiment were blocked and stained but did not undergo incubation with any target protein or phage. The bar graphs in C represent the relative fluorescence intensities, calculated from the median fluorescence intensities of 10,000 events recorded by the flow cytometer, and are presented as mean ± SD from three separate experiments with superimposed scatter plots. The statistical significance markers * and *** indicate significant differences ($p < 0.05$ and $p < 0.001$, respectively) from control (ANOVA followed by Dunnett's test).* ***(B)*** *representative intensity distribution histograms of beads from the phage binding experiment in A (149).*

4.2 Scalable KcsA-Kv1.x chimera expression and purification: T-only and T+F version

Both turret-filter (T+F) and turret-only (T-only) chimeric versions of the KcsA-Kv1.x channels were successfully expressed and purified. DNA constructs encoding the

chimeric proteins were cloned into pQE or pET expression plasmids. Optimized expression and purification protocols were applied to produce sufficient quantities of KcsA-Kv1.x chimeric proteins (see materials and methods for details).

Initial expression trials demonstrated that KcsA-Kv1.1, KcsA-Kv1.2, and T+F KcsA-Kv1.3 and T-only chimeric proteins were successfully expressed in the membrane fractions of several *E. coli* strains. Among these, C41 (DE3) *E.coli* stain yielded the highest levels of of active KcsA-Kv1.x tetramers capable of binding peptides. The expressed proteins were purified using a stepwise approach, starting with high-speed centrifugation to isolate the membrane fraction, followed by immobilized metal affinity chromatography and gel filtration chromatography. Gel filtration chromatograms revealed multiple elution peaks for each chimeric protein (**Figure 19.**), with active tetramer peaks confirmed by phage ELISA. Active tetramer fractions were then pooled, concentrated, aliquoted, and stored at −80°C.

DOI:10.14753/SE.2025.3224

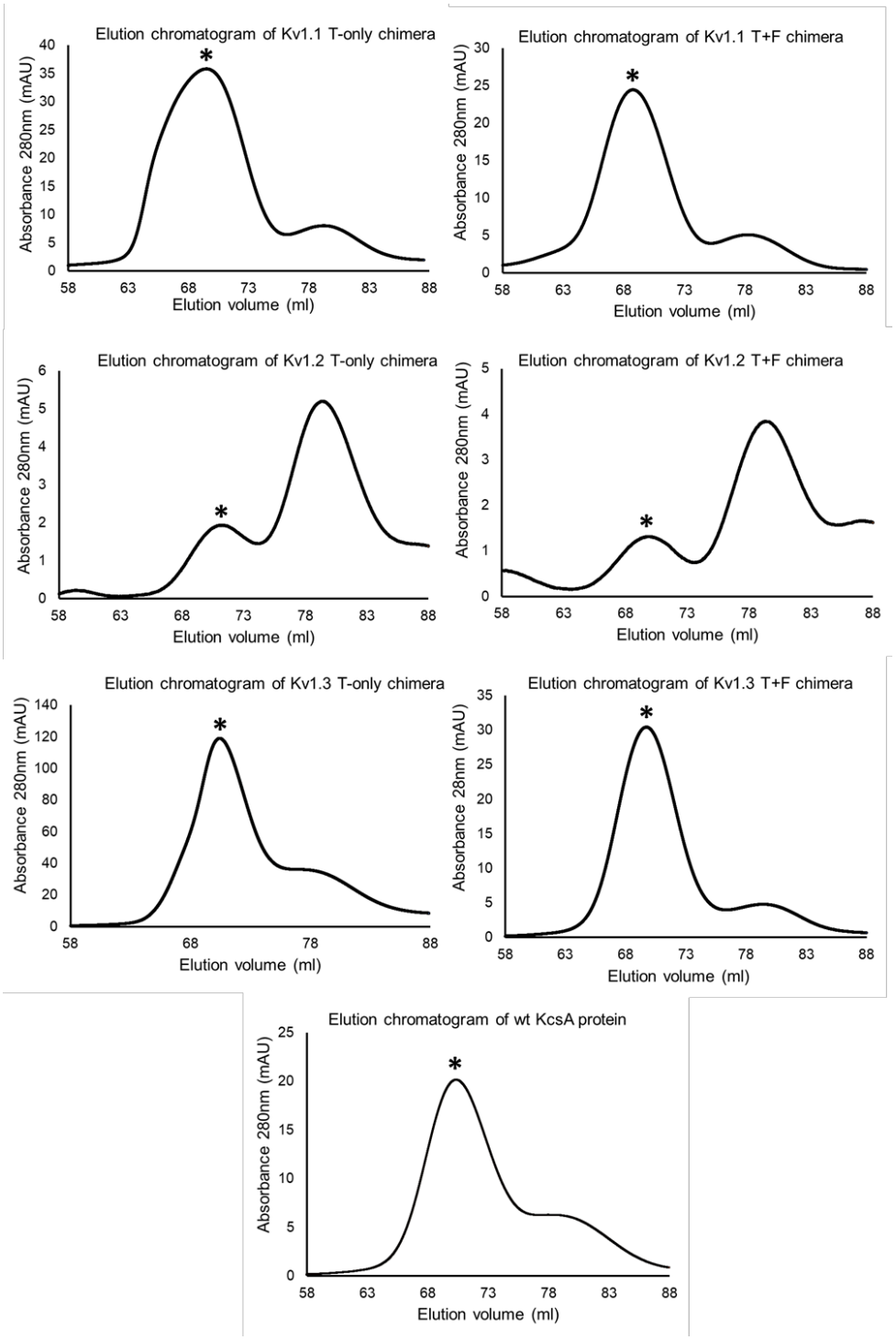

Figure 19. *Elution profile of KcsA-Kv1.x chimeras in gel filtration chromatography. Representative gel filtration chromatograms display WT KcsA alongside T-only KcsA-Kv1.x and T+F chimeras. Protein samples were introduced into a HiLoad 16/600 Superdex 200 pg column and eluted at a flow rate of 1 ml/min. The peak corresponding to active tetrameric chimeras is marked with a black asterisk (*). The T+F label designates the Turret-Filter variant of the KcsA-Kv1.x chimera (138).*

DOI:10.14753/SE.2025.3224

Purified proteins were analyzed by SDS-PAGE, revealing high purity for all chimeric and wild-type KcsA proteins (**Figure 20., A**). Both monomeric and tetrameric forms were identified using western blot with mouse anti-His monoclonal antibody against the N-terminal 6×His-tag fused to the chimeric proteins. Monomers and tetramers migrated at the expected molecular weights, suggesting intact proteins (**Figure 20., B**). Tetrameric bands were detected for wtKcsA and Kv1.1, Kv1.3 chimeras in both T-only and T+F versions on SDS-PAGE. However, no tetramer bands were observed for T-only and T+F KcsA-Kv1.2 chimeras under these denaturing conditions.

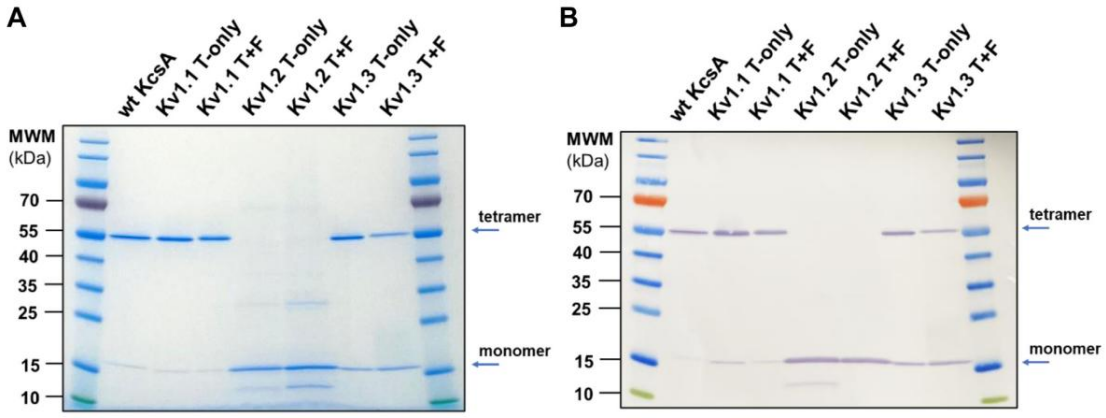

Figure 20. *SDS-PAGE and western blot analysis of KcsA-Kv1.x chimera.* ***(A)*** *SDS-PAGE analysis of purified KcsA-Kv1.x chimeras. Eluted fractions containing active tetrameric chimeras from gel filtration were pooled, concentrated, and stored in aliquots at −80°C. A 0.5 µg sample of each chimera was loaded onto a Tris-Glycine 4–16% gradient gel and electrophoresed at 200 V for 55 minutes. The gel was subsequently stained using a protein gel stain.* ***(B)*** *Western blot analysis of purified KcsA-Kv1.x chimeras, with 0.5 µg of protein per well. Following transfer at 25 V for 120 minutes, detection was carried out using a mouse anti-6×His-tag monoclonal primary antibody and a goat anti-mouse IgG HRP-conjugated secondary antibody. A chemiluminescent solution was used for visualization. The T+F label represents the Turret-Filter variant of the KcsA-Kv1.x chimera (138).*

To confirm the presence of tetramers, we analyzed the chimeric proteins using native PAGE. Most membrane proteins require detergent-containing loading buffer for native conditions; therefore, we tested the purified chimeras with the mild non-ionic detergents digitonin and DDM. Tetrameric forms of all chimeras were identified using digitonin

(**Figure 21., A**). The KcsA-Kv1.1, KcsA-Kv1.2, and T+F KcsA-Kv1.3 chimeras were also tested with DDM by native PAGE, revealing tetramers in their multimeric forms (**Figure 21., B**).

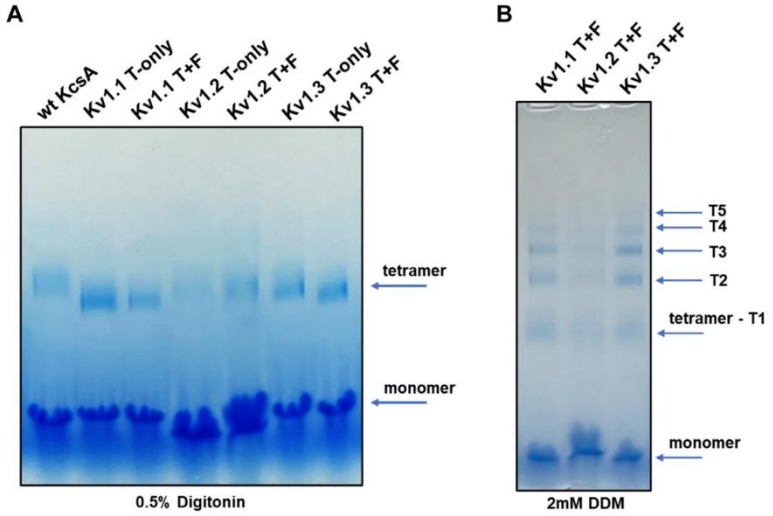

Figure 21. *Native PAGE analysis of KcsA-Kv1.x chimera. A 0.5 µg sample of each chimera was loaded per well onto a 4–16% gradient Bis-Tris gel, supplemented with the specified concentrations of either Digitonin* ***(A)*** *or N-Dodecyl-β-D-maltoside (DDM)* ***(B)*** *detergents. Electrophoresis was conducted at 150 V for 105 minutes. Due to experimental conditions, up to five distinct species (n = 5) were detected: T1 represents a single tetramer, while T2–T5 correspond to multimers of tetrameric chimeras. The T+F label designates the Turret-Filter variant of the KcsA-Kv1.x chimera (138).*

4.3 Selection of Kv1.x targeting scaffolds for chimera characterization and future screening

A database of K^+ channel-targeting miniproteins was compiled from literature and curated sources to identify structural scaffolds relevant for chimera characterization and future library design aimed at developing new Kv1.3 inhibitors. All sequences associated with potassium channels were collected from these datasets.

- http://kaliumdb.org/
- https://venomzone.expasy.org/
- http://www.conoserver.org/
- http://www.reptile-database.org/

- http://www.arachnoserver.org/
- https://www.uniprot.org/

Entries were categorized based on sequence alignments using Clustal Omega, and disulfide bridge patterns were analyzed with PyMOL to classify miniprotein scaffolds. The classification of scaffolds is summarized in **Table 3.**

Table 3. *Identified molecular scaffolds and their key characteristics; the table provides the main representative member of each unique molecular scaffold, along with the potassium channel types that are known to be inhibited by members of each scaffold.*

Scaffold No.	Scaffold representing example	Inhibited K^+ channels
1. scaffold	κ-KTx 1.2, Kappa-hefutoxin-2	KCa1.1, Kv1.3
2. scaffold	Kunitz-type conkunitzin-S1	Shaker, Kv1.7
3. scaffold	Tertiapin	Kir1.1, Kir3.1/Kir3.4
4. scaffold	Potassium channel toxin SsTx	Kv7.1, Kv7.2, Kv7.4,
5. scaffold	Alpha/kappa-conotoxin pl14a	Kv1.6
6. scaffold	**α-KTx 3.1, Kaliotoxin-1**	**Kv1.3, Kca1.1, KCa3.1**
7. scaffold	Plectasin	Kv1.3
8. scaffold	α-KTx 20.3, Kappa-buthitoxin-Tt2b	Kv1.3, Kv1.2
9. scaffold	**Kappa-stichotoxin-She3a, ShK-toxin**	**Kv1.3, Kv1.1, Kv1.4**
10. scaffold	Kappa-actitoxin-Bgr1a, Bgk-toxin	Kv1.1, Kv1.3, Kv1.2
11. scaffold	Kunitz-type serine protease inhibitor IX	Kv1.3
12. scaffold	Kappa-theraphotoxin-Gr2a	Kv4.2, Kv4.3, Kv1.3
13. scaffold	Kappa-theraphotoxin-Pg1a	Kv4.2, Kv2.1, Kv1.3
14. scaffold	Kappa-conotoxin PVIIA	Shaker
15. scaffold	δ-KTx 2.1, Kunitz-type s.p.i. LmKTT-1a	Kv1.3
16. scaffold	DeltaKappa-actitoxin-Avd4a	Kv3.1, Kv3.4, Kv1.3
17. scaffold	Crotamine	Kv1.3
18. scaffold	Beta-defensin 4A, hBD-2	Kv1.3, KCa1.1
19. scaffold	Kappa-scoloptoxin-Ssm1a	Kv1, Kv7.1
20. scaffold	Beta-bungarotoxin B2 chain	Kv1
21. scaffold	**α-KTx 6.2, Maurotoxin**	**Kv1, Kv1.2, Kv1.3**
22. scaffold	**α-KTx 23.2, Vm24-toxin**	**Kv1, Kv1.1, Kv1.3**
23. scaffold	α-KTx 12.1, Ts6-toxin	Shaker, Kv1.1, Kv1.3
24. scaffold	γ-KTx 1.1, Ergtoxin	Kv11.1, Kv11.3
25. scaffold	ε-KTx 1.1, Ts11-toxin	Kv1.3
26. scaffold	Kappa-hexatoxin-Hv1c	KCa1.1

An example of the disulfide bridge pattern and tertiary structure analysis using PyMOL is shown in **Figure 22.**

DOI:10.14753/SE.2025.3224

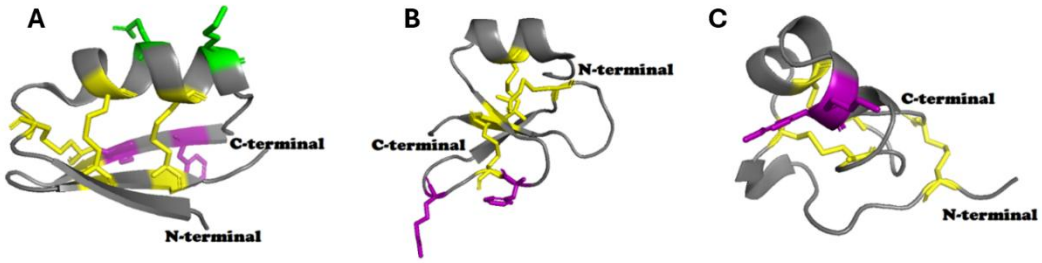

Figure 22. *Three-dimensional structural models created with the molecular modeling program PyMol, showing representations of three different scaffolds with disulfide bridge connections highlighted in yellow;* ***(A)*** *OsK1-toxin* ***(B)*** *HBD2* ***(C)*** *ShK-toxin*

Beyond cysteine connectivity, known signal and propeptide sequences were also considered. The results of sequence alignments and scaffold grouping with members are visualized in ***Appendix.*** The sequences recorded in this collection should be interpreted as shown on **Figure 23.**

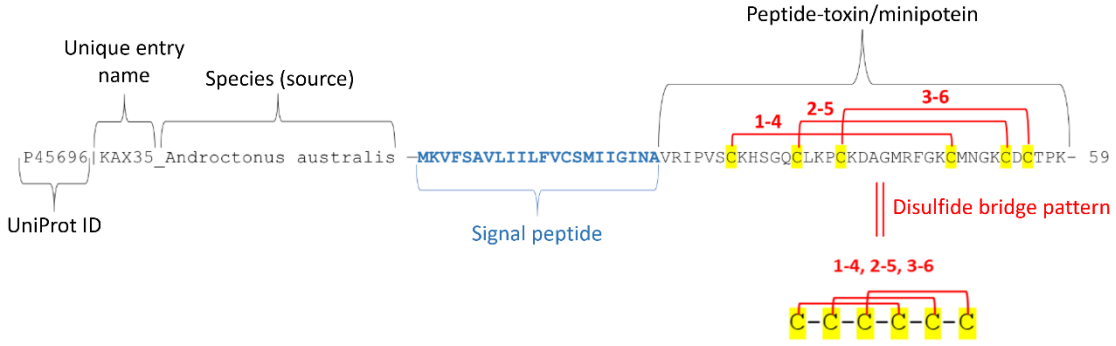

Figure 23. *Example sequence in the database with key informations highlighted. The figure illustrates a scorpion toxin peptide (Androctonus australis), highlighting its UniProt ID (P45696), signal peptide (blue), and mature toxin region. The disulfide bridge pattern (1-4, 2-5, 3-6) stabilizes the structure, with cysteines (yellow) and connectivity (red lines) essential for ion channel modulation.*

From the 26 potassium channel-inhibiting scaffolds, we selected the four most suitable for combinatorial library design, incorporating a detailed evaluation from medicinal chemists to ensure optimal developability (**Figure 24.**).

DOI:10.14753/SE.2025.3224

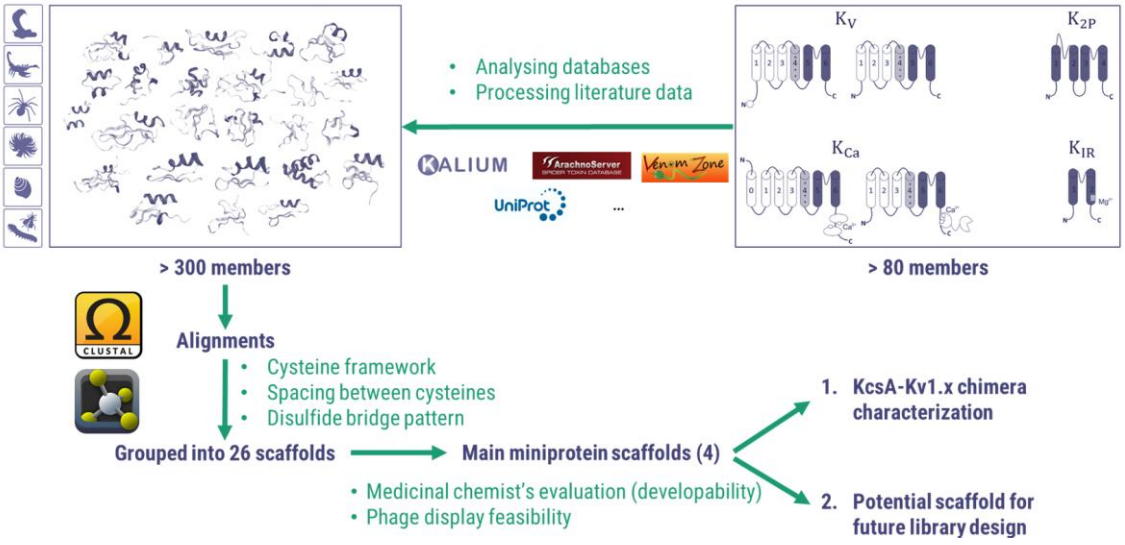

Figure 24. *Summary of in silico analysis and classification of scaffolds. The workflow for identifying and classifying miniprotein scaffolds that target potassium (K^+) channels, aimed at designing new Kv1.3 inhibitors. Over 300 sequences from venom-derived miniproteins were collected from databases such as Kalium 3.0, UniProt, ArachnoServer, and others. Sequences were aligned using Clustal Omega and structurally analyzed (e.g., cysteine patterns, disulfide bridges) with PyMOL, leading to classification into 26 scaffolds. Four main scaffolds were selected based on developability and phage display feasibility for two purposes: Kv1.x chimera characterization and future library design.*

The identified four main scaffolds are shown on **Figure 25.**

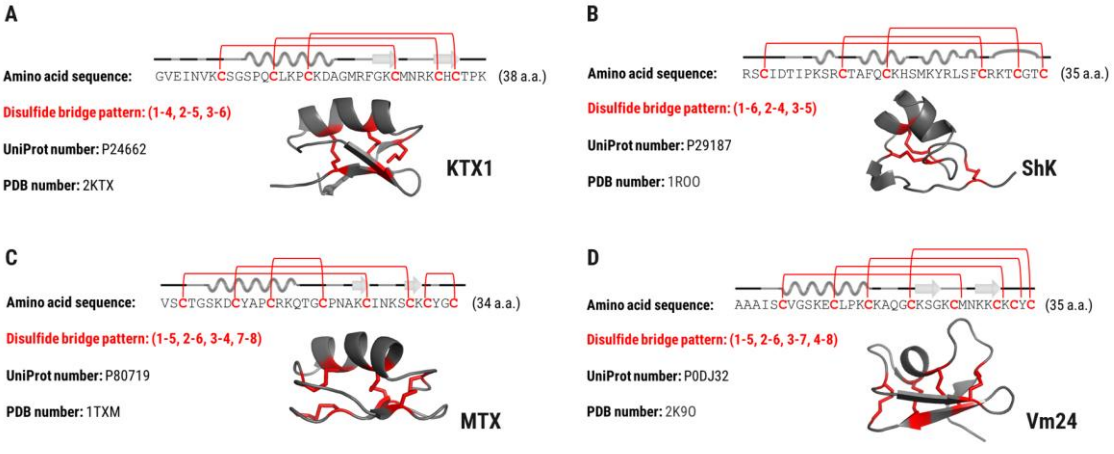

Figure 25. *Selected scaffold representatives for chimeric testing. This figure presents four representative scaffolds of potassium channel-inhibiting peptides, selected from a custom database with a focus on Kv1.3 inhibition. Each scaffold* ***(A–D)*** *is displayed with its*

amino acid sequence, disulfide bridge pattern, UniProt accession number, and PDB structure. The secondary structure of each peptide is illustrated, highlighting the connectivity of disulfide bonds in red.

For each of the four miniprotein scaffolds, a representative peptide toxin—Vm24, MTX, ShK, or KTX1—was selected for display on the P3 coat protein of M13 bacteriophages. Additionally, HgTX1, which shares the same scaffold as KTX1, was also included. These peptide toxins were used to analyze T-only and T+F KcsA-Kv1.x chimeras.

4.4 Assessment of T-only and T+F KcsA-Kv1.3 chimeras

The methods used to evaluate the binding affinity and blocking potency of the selected peptide toxin-displaying phages and synthesized miniprotein versions are illustrated on **Figure 26.** To confirm the pharmacological rank order, whole-cell patch-clamp experiments were performed on mammalian cells to measure the blocking potency of selected toxins on hKv1.1, hKv1.2, and hKv1.3 channels (**Figure 26., A**). Relative binding affinities were measured using phage ELISA, detecting interactions between peptide toxin-displaying phages and Kv1.x chimera-coated surfaces (**Figure 26., B**). The IC50/displacing potency values of synthetic peptide toxins were determined in a competition assay using HgTx1-displaying phages for Kv1.3 and Kv1.2, and ShK-displaying phages for Kv1.1 as indicator ligands (**Figure 26., C**).

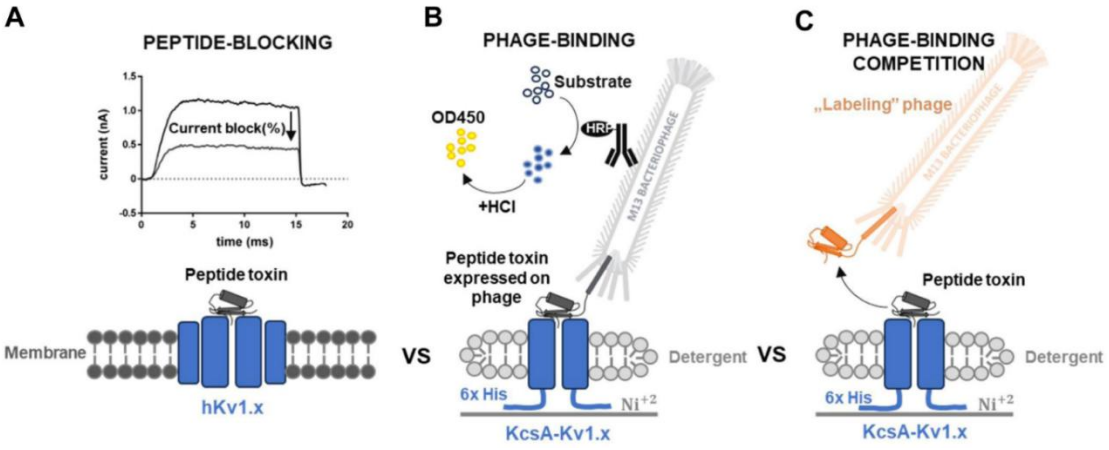

Figure 26. *The illustration of the comparative analysis of T-only KcsA-Kv1.x and T+F chimeric proteins with human Kv1.x channel proteins. (**A**) Patch-clamp assay: Human Kv1.x (hKv1.x) channel blocking by toxin test substances was assessed using whole-cell*

patch-clamp experiments. Whole-cell current traces were recorded before and after perfusion of the tested toxin, using the appropriate voltage protocol for each hKv1.x channel. ***(B)*** *Phage ELISA binding assay: A His-tagged chimeric target protein was immobilized on a nickel-coated plate, followed by the addition of toxin peptide-displaying phages. After washing away unbound particles, bound phages were labeled with an HRP-conjugated antibody, and detection was achieved via HRP-catalyzed signal generation upon substrate addition.* ***(C)*** *Phage ELISA binding competition assay: Binding of labeling phages (HgTX1- or ShK-displaying) was analyzed as in (B), with the simultaneous application of varying concentrations of competing toxin test substances to assess competitive binding effects (138).*

The relative binding affinities of various channel-blocking toxins were assessed for the T-only version of the KcsA-Kv1.3 chimera. These affinities were compared to the blocking potency of the same toxins on native hKv1.3 channels, measured by patch-clamp assay. Three toxins—Vm24, HgTx1, and KTX1—were selected based on their reported Kv1.3 channel-blocking IC50 values of 3 pM, 86 pM, and 650 pM, respectively (**Table 4.**).

Comparing the potency of the chosen toxins to block the native Kv1.3 channel during patch-clamp experiments showed notable differences from the binding assay results with the T-only chimeric channel (**Figure 27., A–E** Patch-clamp electrophysiology results ranked the blocking potencies as Vm24 > HgTx1 > KTX1 (**Figure 27., A**, and **Table 4.**). No detectable binding of the tested phage-displayed toxins to WT KcsA was observed **Figure 27., B**. Phage-binding assays showed comparable binding levels for Vm24 and KTX1, while HgTx1 exhibited lower binding to the T-only chimera (**Figure 27., C**). The IC50 values of Vm24, HgTx1, and KTX1 in competition binding assays with the T-only chimera ranged from 0.42 to 0.67 nM (**Figure 27., E**).

DOI:10.14753/SE.2025.3224

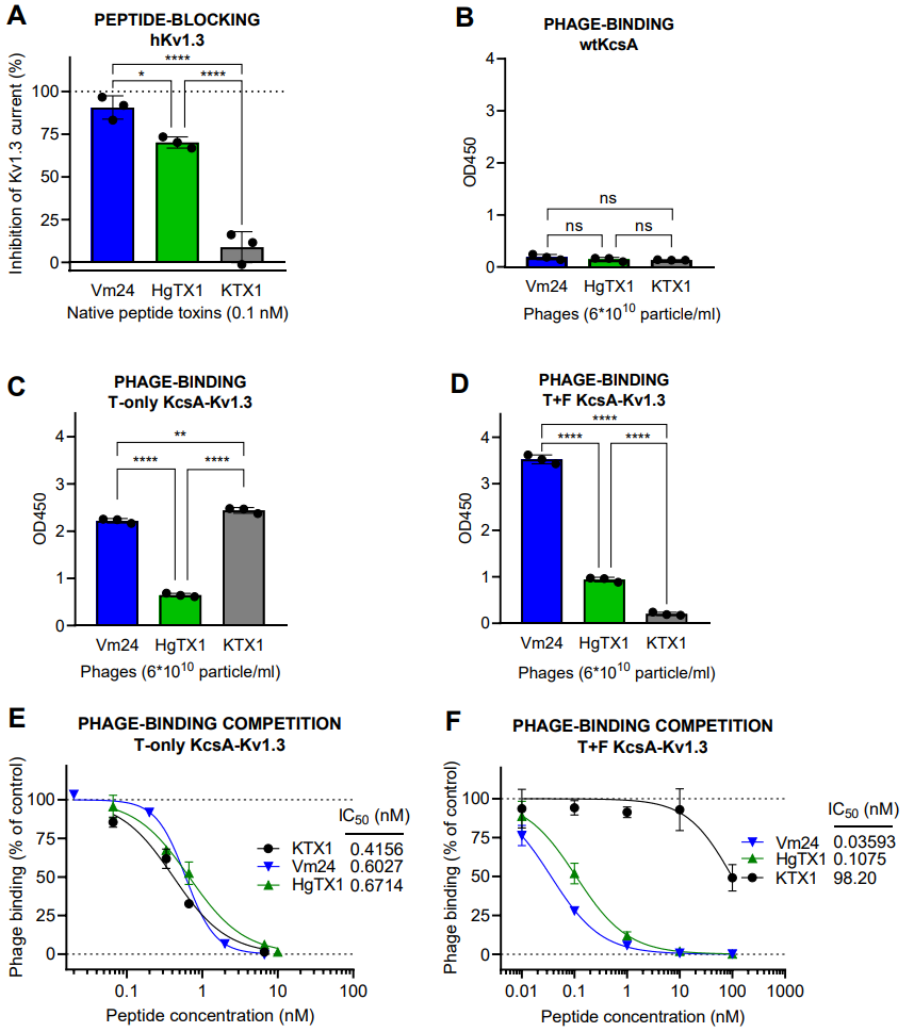

Figure 27. *Comparison of T-only KcsA-Kv1.3 and T+F chimera binding to native Kv1.3 channel blocking potency.* ***(A)*** *Inhibition of hKv1.3 potassium currents (%) by peptide toxins Vm24, HgTX1, and KTX1 at 0.1 nM was measured via patch-clamp in human lymphocytes.* ***(B)*** *Phage ELISA binding of toxin-expressing phages to WT KcsA (negative control) was assessed by absorbance.* ***(C)*** *Phage binding of Vm24, HgTX1, and KTX1 to T-only KcsA-Kv1.3 was tested in the phage-binding assay.* ***(D)*** *Similarly, phage binding of the three toxins to T+F KcsA-Kv1.3 was evaluated.* ***(E)*** *Percent phage binding vs. log concentration plots and IC50 values for toxin test substances were obtained from the HgTx1-phage binding competition assay using T-only KcsA-Kv1.3.* ***(F)*** *The same assay was performed on T+F KcsA-Kv1.3, with all data expressed as mean ± SD from three replicates. Statistically significant IC50 differences were confirmed in* ***(F)*** *but not in* ***(E)*** *using one-way ANOVA and Tukey HSD tests, with significant differences marked and nonsignificant results labeled as 'ns' (138).*

Binding assays were conducted for the selected toxins on both the T-only and T+F KcsA-Kv1.3 chimeras to compare their interactions. The rank order of affinities in both phage-binding (**Figure 27., D**) and competition assays (**Figure 27., F**) was consistent with the blocking potencies observed in native Kv1.3 channels during patch-clamp studies (Vm24 > HgTx1 > KTX1) (**Figure 27., A)**. This demonstrates that the T+F KcsA-Kv1.3 chimera is a more reliable predictor of Kv1.3 channel blocking potency than the T-only KcsA-Kv1.3 chimera.

4.5 Assessment of T-only and T+F KcsA-Kv1.1 and Kv1.2 chimeras

MTX, ShK, and KTX1 were selected for comparative studies on Kv1.2 and Kv1.1 channels, covering a range of potency values from sub-nanomolar to high-nanomolar. The binding of these toxins to the T-only KcsA-Kv1.2 chimera showed significant discrepancies compared to their potencies in blocking the native Kv1.2 channel. MTX1, which has a high blocking potency for native Kv1.2 channels (**Figure 28., A**), showed no binding to the T-only KcsA-Kv1.2 chimera in both the phage-binding (**Figure 28., C**) and competition assays (**Figure 28., E**). Similarly, the rank order of the affinities of ShK and KTX1 was also inconsistent with their mammalian channel blocking potencies (**Figure, A, C and E**). In contrast, for the T+F KcsA-Kv1.2 chimera the rank order of affinities for the three toxins aligned with their channel blocking potencies (**Figure 28., A, D, and F**).

DOI:10.14753/SE.2025.3224

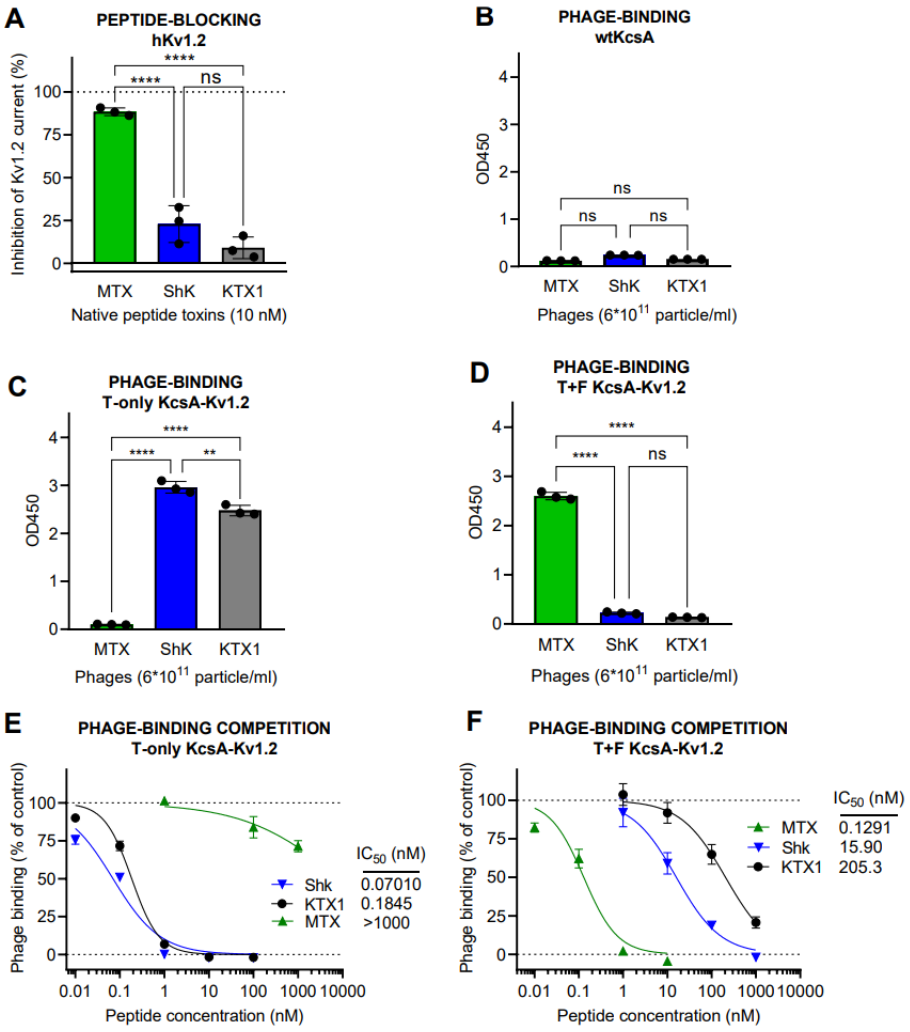

Figure 28. *Comparison of T-only KcsA-Kv1.2 and T+F chimeras binding to native human Kv1.2 channel blocking potency.* ***(A)*** *Peptide toxins MTX, ShK, and KTX1 inhibited hKv1.2 currents (percent inhibition) at 10 nM, measured via patch-clamp in CHO cells.* ***(B)*** *Phage ELISA binding of toxin-expressing phages to WT KcsA (negative control) was assessed.* ***(C)*** *Phage binding of MTX, ShK, and KTX1 to T-only KcsA-Kv1.2 was measured.* ***(D)*** *Binding of the three toxins to T+F KcsA-Kv1.2 was analyzed.* ***(E)*** *Percent phage binding vs. log concentration plots and IC50 values were obtained from the HgTx1-phage binding competition assay using T-only KcsA-Kv1.2.* ***(F)*** *The HgTx1-phage binding competition assay on T+F KcsA-Kv1.2-coated plates yielded IC50 values, with all data expressed as mean ± SD from three replicates. Data visualization includes bar graphs with scatter plots and sigmoidal curve fitting. IC50 differences in* ***(E)*** *and* ***(F)*** *were analyzed using one-way ANOVA and Tukey HSD tests, with significant differences marked and nonsignificant results labeled as 'ns' (138).*

DOI:10.14753/SE.2025.3224

The predictivity of the KcsA-Kv1.1 chimera ligand binding for human Kv1.1 channel blocking potency was assessed similarly. In the competition-binding assay, ShK-phage was used as the displaced indicator ligand due to its exceptionally high affinity for the Kv1.1 receptor, making the assay more sensitive than using HgTX1-phage. This increased sensitivity allowed for a more precise assessment of binding interactions with the KcsA-Kv1.1 chimeras. For KcsA-Kv1.1 chimeras, phage-binding and competition-binding results were comparable for both T-only and T+F versions (**Figure 29., C–F**). This indicated similar affinities for the test toxins to both versions, with a rank order of ShK > KTX1 and negligible binding of MTX1, either in phage-displayed (**Figure 29., C and D**) or native peptide form (**Figure 29., E and F**). The binding rank order for the KcsA-Kv1.1 chimeras was consistent with previously reported hKv1.1 channel blocking potency rankings (**Figure 29., A**).

DOI:10.14753/SE.2025.3224

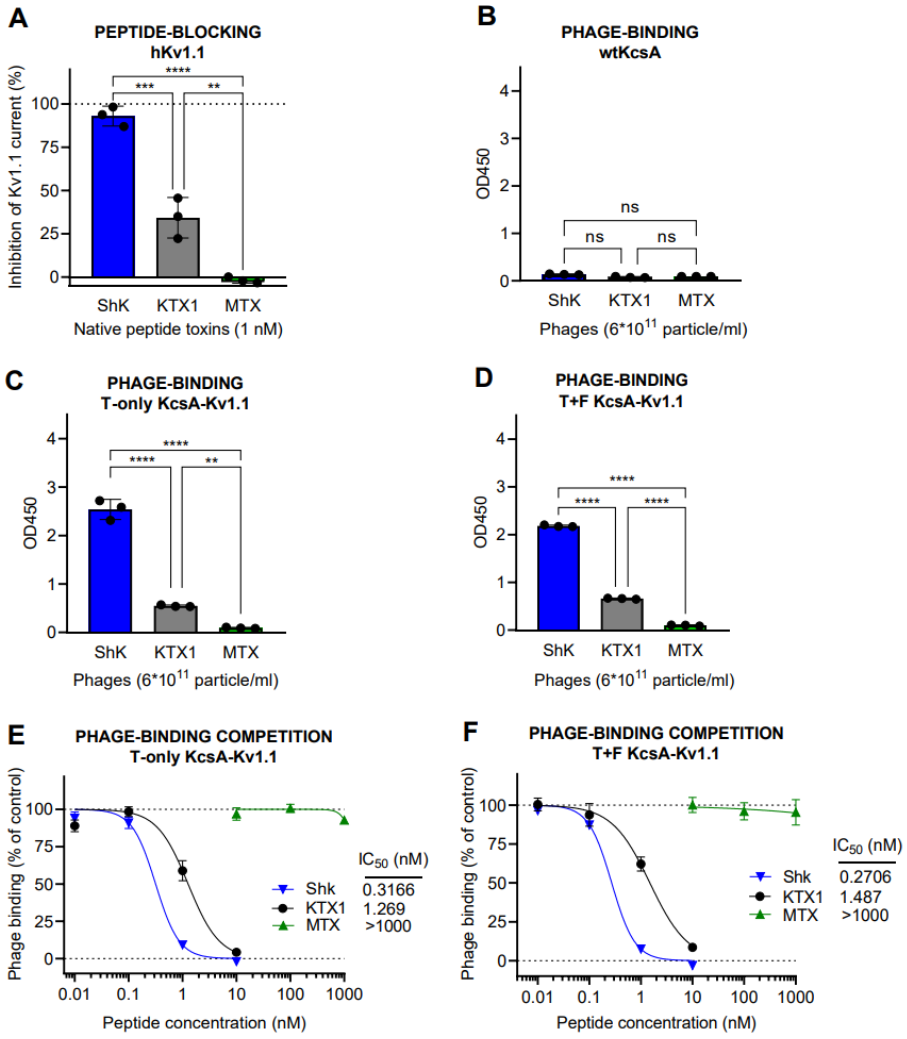

Figure 29. *Comparison of T-only KcsA-Kv1.1 and T+F chimera binding to native Kv1.1 channel blocking potency.* ***(A)*** *Peptide toxins ShK, KTX1, and MTX inhibited hKv1.1 currents (percent inhibition) at 1 nM, measured via patch-clamp in CHO cells.* ***(B)*** *Phage ELISA binding of toxin-expressing phages to WT KcsA (negative control) was assessed.* ***(C)*** *Phage binding of ShK, KTX1, and MTX to T-only KcsA-Kv1.1 was measured.* ***(D)*** *Binding of the three toxins to T+F KcsA-Kv1.1 was analyzed.* ***(E)*** *Percent phage binding vs. log concentration plots and IC50 values were obtained from the ShK-phage binding competition assay using T-only KcsA-Kv1.1.* ***(F)*** *The ShK-phage binding competition assay on T+F KcsA-Kv1.1-coated plates yielded IC50 values, with all data expressed as mean ± SD from three replicates. Data visualization includes bar graphs with scatter plots and sigmoidal curve fitting. IC50 differences in (E) and (F) were analyzed using one-way ANOVA and Tukey HSD tests, with significant differences marked and nonsignificant results labeled as 'ns' (138).*

DOI:10.14753/SE.2025.3224

4.6 Functional assessment of miniprotein displaying phages

Phage-displayed toxins were tested to assess their hKv1.3 channel blocking potency. Whole-cell patch-clamp assays using human PBMSs were used to measure the hKv1.3 channel blocking efficiency of phage-displayed Vm24, HgTX1, and KTX1. TEA^+ at 10 mM inhibited approximately 50% of the Kv1.3 current, serving as a positive control for recording conditions. A mutant form of KTX1, DDDKTX1, which does not bind Kv1.3, did not inhibit Kv1.3 currents in its phage-displayed form (**Figure 30.**)(30). This served as an important negative control to exclude the possibility that the phage construct itself could inhibit the Kv1.3 current independently of the fused toxin. Phage concentrations for comparative testing were determined based on their relative binding effectiveness to Kv1.3 T+F chimeras (refer to **Figure 27., D**). The concentration required to achieve approximately 50% current inhibition was determined for each phage-displayed toxin (**Figure 30., A and B**).

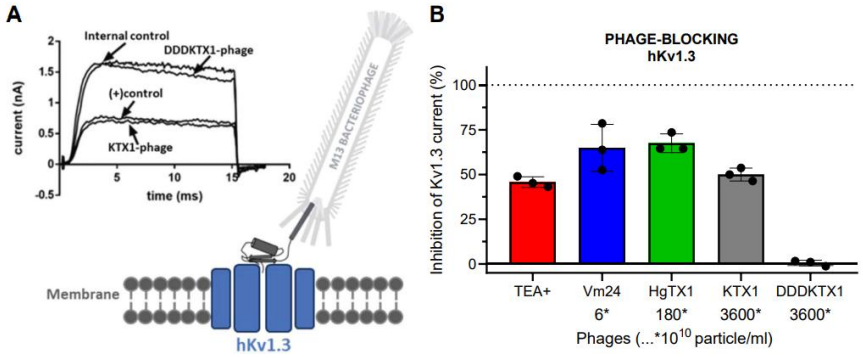

Figure 30. *Human Kv1.3 potassium channel blocking effects of phage-displayed toxin peptides.* ***(A)*** *Schematic of a peptide toxin expressed on a phage binding to the hKv1.3 channel, alongside representative whole-cell current traces with TEA+ (10 mM) as a positive control, KTX1-phage, and inactive DDDKTX1-phage. Peptide toxins were fused to the P3 coat protein of M13 phages via an eight-amino acid linker.* ***(B)*** *Blocking effect (percent inhibition) of phage-expressed peptide toxins on hKv1.3, measured by patch-clamp in human T-lymphocytes. TEA+ (10 mM, red) served as a positive control, typically inhibiting ~50% of hKv1.3 currents. KTX1-phages (gray, 3.6 × 10^{13} particles/ml) effectively blocked currents, while DDDKTX1-phages (black) showed no inhibition. The bar graph compares the blocking effects of HgTX1 (green) and Vm24 (blue) phages at 1.8 × 10^{12} and 6 × 10^{10} particles/ml, respectively, reflecting their relative Kv1.3-blocking potencies. Data represent mean ± SD of peak currents (N = 3) (138).*

Using this approach, the affinity of the phage-displayed peptides for Kv1.3 is inversely proportional to the phage concentration required to block the current by 50%—lower inhibitory phage concentration indicates higher affinity. All three phages significantly inhibited the Kv1.3 current, demonstrating that the C-terminal fusion of these toxins to the P3 envelope protein of M13 phages does not hinder their inhibitory potential. The estimated relative potencies, calculated from the phage concentrations required to reach a 50% blocking effect, were approximately 1, 1/30, and <1/600 for Vm24, HgTx1, and KTX1, respectively (**Figure 30., B**).

4.7 Developing a biopanning protocol using the T+F KcsA-Kv1.3-based screening assay for HTS application

The above described phage-ELISA binding assay (**Figure 26., B**) was converted into a HTS format through the application of biopanning. First, I compared the phage-ELISA binding signals with phage titers used for enrichment calculation obtained using Vm24 phages in 10^9 and 10^{10} input titer to ensure that the binding interactions observed in the ELISA were consistent with the enrichment patterns seen in the panning experiments. In **Figure 31., A** the signal-to-noise ratio represents results from the HRP-Ab based ELISA, where binding was measured by absorbance at 450nm. In contrast, **Figure 31., B** shows the number of eluted phages when the protocol was stopped before adding the HRP-Ab; instead, bound phages were eluted, neutralized and used to infect *E.coli* cells, and quantified by counting resulting colonies. These colony counts indicate how many phages were eluted from the wtKcsA and Kv1.3.KcsA T+F chimera. The bacteria can only grow on ampicillin agar plates if infected by phages, as the phage transfers the resistance gene.

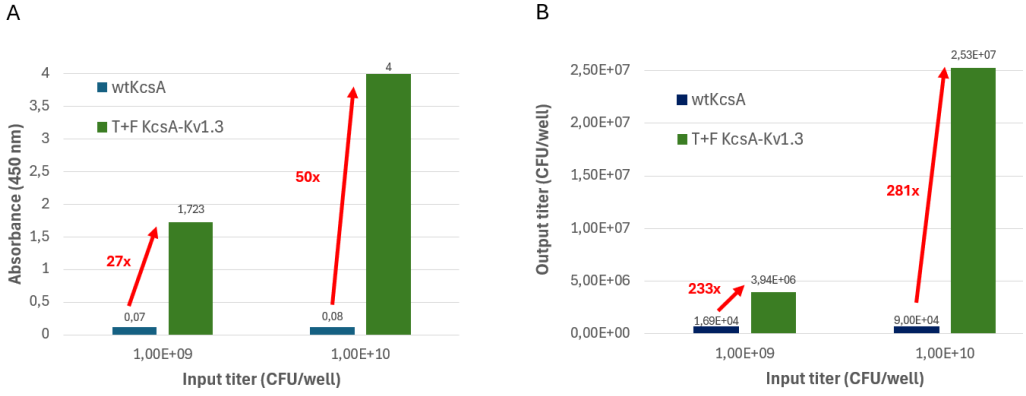

Figure 31. *Phage ELISA binding data compared with enrichment data.* ***(A)*** *Binding to either wtKcsA (blue) or the T+F Kv1.3-KcsA chimera (green) was quantified using HRP-*

conjugated antibody-based phage ELISA. Absorbance at 450 nm indicates the relative strength of binding. At an input of 10^9 CFU/well, the chimera produced a signal of 1.723, which is 27 times higher than wtKcsA (0.07). At 10^{10} CFU/well, the absorbance for the chimera increased to 4.0, representing a 50-fold increase over wtKcsA (0.08). ***(B)*** *Phages bound to wtKcsA or the T+F chimera were eluted, neutralized, and used to infect E. coli. Resulting colonies on ampicillin plates reflect the number of infectious phage particles. At 10^9 CFU/well input, output titer for the chimera reached 3.94×10^6 CFU/well, corresponding to a 233-fold enrichment over wtKcsA (1.69×10^4). At 10^{10} CFU/well input, the chimera yielded 2.53×10^7 CFU/well, a 281-fold increase compared to wtKcsA (9.00×10^4).*

While the ELISA assay showed a signal-to-noise ratio of 27- to 50-fold, titering measurements revealed even higher values—233- and 281-fold—for phages eluted from the Kv1.3-KcsA T+F chimera compared to wtKcsA, representing the enrichment of binder phages.

Second, phage mixtures containing Vm24 and DDDKTX1 in a 1:9 ratio—comprising 90% DDDKTX1-displaying phages—were prepared at a concentration of 10^{10} CFU/well. This mixture was screened against T+F KcsA-Kv1.3-coated wells, with BSA-coated wells serving as controls. Vm24-displaying phages were successfully recovered, showing a 62.5-fold enrichment over the BSA control after a single round of panning (**Figure 32.**).

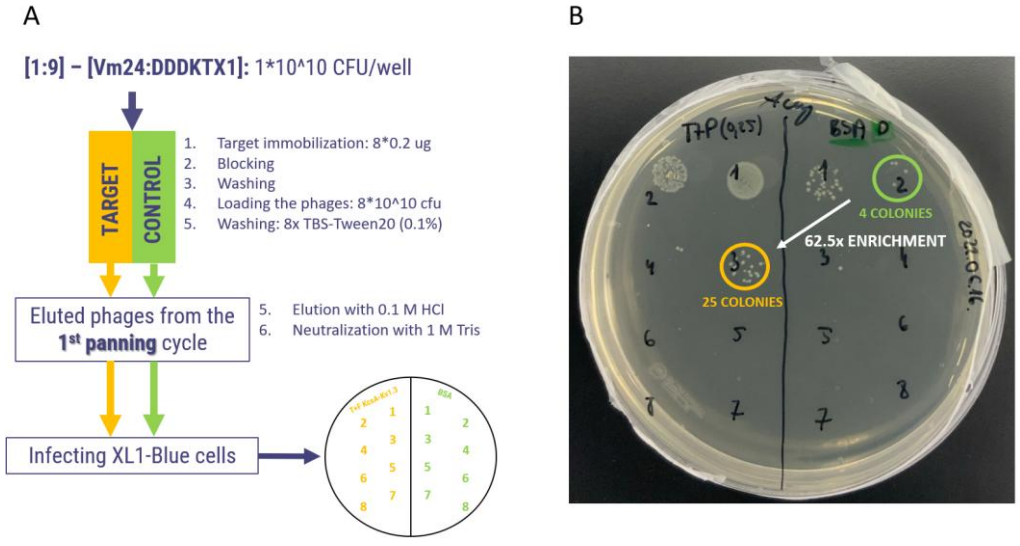

Figure 32. *Panning cycle and enrichment of Vm24 from a 1:9 Vm24-DDDKTX1 phage mixture.* ***(A)*** *Schematic of the first panning cycle using a 10^{10} CFU/well phage mixture*

DOI:10.14753/SE.2025.3224

(1:9 Vm24:DDDKTX1). Phages were incubated with T+F KcsA-Kv1.3-coated wells (target) and BSA-coated wells (control). Eluted phages were used to infect E. coli XL1-Blue cells for colony-based output quantification. ***(B)*** *Agar plate showing 25 colonies from the 4th dilution of the target well vs. 4 colonies from the 2nd dilution of the BSA control, corresponding to a 62.5-fold enrichment of Vm24 after a single panning round.*

DOI:10.14753/SE.2025.3224

5 DISCUSSION

Developing and optimizing screening assays are crucial for designing selective and potent drug candidates, especially for complex targets. While computational advances, such as AlphaFold2 (150), have improved our understanding of protein structures, and facilitated drug discovery programs, HTS systems remain critical for hit and lead identification.

This research bridges a key gap in two different therapeutic development processes, addressing the unique challenges associated with targeting Kv1.3, a potassium channel involved in chronic inflammatory diseases, and MMP-2 implicated in GBM and other cancers.

The research demonstrated the successful development and optimization of robust screening assays to these distinct ligand-target combinations, showcasing novel methodologies that improve sensitivity, specificity and translational relevance. This discussion reflects on the significance of these findings, and their place within the broader landscape of drug discovery.

5.1 Clarifying CTX binding properties

The bead-based assays developed for studying CTX interactions provided valuable insights into its binding properties and target specificity.

The **Ig-coated bead test** used immobilization strategies and rigorous washing steps to improve sensitivity, allowing reliable detection of low-affinity ligands like CTX and its derivatives. The displacement assays, using fluorescently labeled CTX variants (CTX-Cy5 and CTX-A488), demonstrated their suitability for studying binding dynamics. The measured binding affinities of CTX variants for MMP-2, determined by displacing fluorescent variants, ranged between 0.62 and 0.75 μM, lower than the 115 nM value reported in the literature. The assay also proved reliable for structure-activity relationship (SAR) studies, demonstrating that CTX and the CTX-like Bs-Tx7 interacted with the same binding site, with Bs-Tx7 exhibiting a 2.6-fold lower affinity than CTX. These findings highlight the Ig-coated bead test's potential to guide the design of more potent CTX analogs (**Figure 16.**).

The **cobalt-coated bead test** expanded the scope of CTX binding studies, allowing us to examine CTX interactions with a wider range of potential targets. CTX-Cy5 exhibited significant binding to NRP1, with comparable intensity to MMP-2. This dual affinity

suggests that CTX has the potential to target both MMP-2-mediated and NRP1-mediated pathways, making it a versatile tool for addressing multiple aspects of tumor biology. Weaker, but notable interactions with chloride channel CLC-3 and tissue inhibitor of metalloproteinases-2 (TIMP-2) were also observed, indicating a broader spectrum of CTX target affinity which could be pivotal (**Figure 17.**).

These assays not only clarified the debated CTX affinity of MMP-2 but also provided valuable insights into its target specificity to better understand its *in vivo* effect in the future.

5.2 Validating the cobalt-coated bead assay as a multi-target screening assay

Parallel investigations with CTX-displaying phages mirrored the binding patterns observed for CTX-Cy5. Both demonstrated strong and consistent binding to MMP-2 and NRP1, with weaker interactions to CLC-3 and TIMP-2. The similar pattern between fluorescently labeled and phage-displayed CTX binding profiles underscores the robustness and versatility of the cobalt-coated bead assay (**Figure 18.**).

This assay's reliability and adaptability for phage display make it well-suited for HTS. It can facilitate the discovery of high-affinity CTX analogs with improved specificity and therapeutic potential by minimizing off-target interactions with proteins like NRP1, CLC-3, and TIMP-2.

5.3 Identification of optimal scaffolds for Kv1.3 inhibition

K^+ channel targeting miniproteins exhibit great structural diversity, with distinct scaffolds described in the literature. Through comprehensive analysis, incorporating sequence alignments, disulfide bridge pattern evaluation, and sequence clustering, I identified 26 potassium channel-targeting miniprotein scaffolds. The selection process identified four key scaffolds, with Vm24, MTX, ShK, and KTX1 as their representatives (**Figure 25.**). These scaffold representatives validated T+F KcsA-Kv1.x chimeras as reliable screening targets and will serve as initial miniprotein structures for library production and phage display-based HTS.

5.4 Improved predictivity of T+F KcsA-Kv1.2 and Kv1.3 chimeras

Building on earlier work that transferred only the turret (T) region, we enhanced a solid-phase screening system by additionally transferring the filter (F) region to improve KcsA-

Kv1.x chimeras. Previous attempts to produce active T+F chimeras faced significant challenges due to weak expression and improper monomer assembly, resulting in defective tetramers (140).

To produce substantial amounts of active proteins, we established new expression and purification protocols, adjusting several parameters (see materials and methods for details). The choice of the appropriate expression strain was crucial; the C41 (DE3) *Escherichia coli* strain, designed for producing difficult-to-express or toxic proteins, proved to be the most effective, likely due to its weakened T7 RNAP activity aiding proper membrane assembly. T-only and T+F KcsA-Kv1.2 chimeras did not show detectable levels of tetramers, in SDS-PAGE masurements, suggesting sensitivity to denaturing and reducing conditions (**Figure 20.** and **Figure 21.**).

We incorporated all T-only and T+F KcsA-Kv1.x chimeras into solid-phase binding assays to evaluate toxin binding and compare it with their blocking potencies on native channel counterparts.

For Kv1.2 and Kv1.3, T-only chimeras showed binding patterns that did not match their native channels. However, the T+F chimeras, which included both the turret and filter regions, restored the correct rank order of toxin affinities (**Figure 27.** and **Figure 28.**). In contrast, both T-only and T+F Kv1.1 chimeras accurately reflected native Kv1.1 properties, with a consistent toxin affinity order (ShK > KTX1 > MTX) (**Figure 29.**).

The Kv1.2 T-only chimeras behaved like Kv1.1, losing affinity for MTX, a key blocker of native Kv1.2. This was linked to the V82Y mutation, as the human Kv1.1 filter region naturally has a Y (tyrosine) at this position, similar to the T-only Kv1.2 chimera, which still retains part of the wild-type KcsA protein which has Y at position 82.

In the T-only KcsA-Kv1.3 chimera, the change in toxin binding was likely caused by the H82Y mutation, which corresponds to His451 in hKv1.3. Structural studies suggest that this residue is critically important for toxin binding, and our findings support this (27,131,141,143–147).

Previously, these limitations prevented the effective use of humanized KcsA chimeras in ligand characterization and have resulted moderately selective Kv1.3 inhibitors, slowing down the development of highly selective Kv1.3 blockers for therapeutic success.

5.5 Bridging binding and functional assessment

To link binding affinity with functional potency, we evaluated the Kv1.3-blocking potency of phage-displayed toxins (Vm24, HgTx1, and KTX1) using whole-cell patch-clamp assays. The results demonstrated that phage-displayed toxins retained their inhibitory properties, aligning closely with their native peptide counterparts. Moreover, a previously characterized mutant of KTX1—DDDKTX1, which is unable to bind to the Kv1.3 channel—did not block Kv1.3 currents in its phage-displayed form, supporting the validity of our patch-clamp measurements (30). The measured relative potencies aligned with the published potencies of the native peptide forms, with IC50 values of 3 pM, 86 pM and 650 pM, respectively (**Table 4.**) (**Figure 30.**).

5.6 HTS potential of T+F KcsA-Kv1.x chimeras

Kv1.x ion channels present challenges for HTS due to their structural complexity and low production yields in membrane-embedded forms. While T-only KcsA-Kv.1x chimeras were available, they featured only partial humanization at the critical binding site/pore region, limiting their reliability. The development of T+F chimeras overcame these obstacles and enabled large-scale production for binding assays and high-throughput applications.

Given the significant translational value of T+F KcsA-Kv1.3 binding, a nickel-coated plate-based ELISA assay was transformed into a HTS approach. This process involved the use of phage-displayed miniproteins Vm24 and DDDKTX1 and biopanning experiments. The result confirmed the optimal immobilized target amount, phage titer input and washing conditions to maximize assay performance (**Figure 31.** and **Figure 32.**).

By integrating scalable chimera production, predictive T+F chimeras, and an optimized biopanning workflow, we established a robust foundation for screening million-scale phage libraries. Using Kv1.1 and Kv1.2 chimeras in the future negative selection cycles will further ensure the identification of highly selective Kv1.3 binders. This approach will speed up the discovery of new, improved Kv1.3 inhibitor drugs.

DOI:10.14753/SE.2025.3224

5.7 Therapeutic potential of miniproteins: Examples and future directions

Peptides, such as the anti-diabetic semaglutide, exemplify the potential of small polypeptides in achieving high affinity and target specificity (151). However, miniproteins take this further by offering additional benefits, including improved stability and favorable pharmacokinetics and overall developability.

Future pharmaceutical research and development should place greater emphasis on miniproteins as a promising therapeutic modality, given their potential to target challenging and clinically relevant proteins like Kv1.3 and MMP-2. The development of HTS-compatible screening assays, such as those in this work, is crucial for accelerating miniprotein discovery. By integrating computational design with structural insights and high-throughput methods, the field can unlock new opportunities for treating chronic inflammatory diseases, cancer, and other conditions with high unmet medical needs.

DOI:10.14753/SE.2025.3224

6 CONCLUSIONS

This research highlights the pivotal role of screening assay development and optimization in advancing targeted miniprotein therapeutics. By focusing on two drug discovery projects at VRG Therapeutics—targeting MMP-2 for cancer therapy and Kv1.3 for chronic inflammatory diseases—this work establishes scalable and reliable screening platforms that streamline the identification of novel miniprotein-based drugs for future applications.

For MMP-2, a bead-based flow cytometry assay was successfully developed, resolving discrepancies regarding CTX binding specificity. Similar binding results obtained with native CTX and phage-displayed CTX underscore the reliability of the cobalt-coated bead assay, providing a strong foundation for future HTS campaigns to further improve MMP-2 affinity and selectivity. If successful, these efforts could lead to new treatments and more precise surgical tools for glioblastoma and other cancers where MMP-2 is overexpressed.

The Kv1.3 project presented additional challenges due to the membrane-bound nature of the target. In this study, these challenges were addressed by designing chimeric constructs that incorporated both the turret and filter regions (T+F) of Kv1.x, enabling structurally and functionally reliable models.

The summary of comparative predictivity assessments is presented in **Table 4.** The displayed IC50 values from competition assays represent toxin affinities. These values are compared with previously reported channel-blocking potencies for the corresponding native hKv1.x channels.

Table 4. *Summary of chimeric protein-binding results studies in the light of IC50 values from literature (138).*

	T-only chimera		T+F chimera		Kv1.x blocking	
Toxin ligand	**IC_{50} (nM)**	**Rank**	**IC_{50} (nM)**	**Rank**	**IC_{50} (nM)**	**Rank**
Kv1.3						
Vm24	0.577 (±0.431)	2	0.036 (±0.004)	1	0.003	1
HgTx1	0.671 (±0.090)	3	0.108 (±0.022)	2	0.086	2
KTX1	0.416 (±0.062)	1	98.2 (±81.6)	3	0.650	3
Kv1.2						
MTX	>1000 (NQ)	3	0.129 (±0.050)	1	0.8	1
ShK	0.070 (±0.026)	1	15.9 (±4.4)	2	9.0	2
KTX1	0.185 (±0.031)	2	205.3 (±59.4)	3	>1000	3
Kv1.1						
ShK	0.317 (±0.069)	1	0.271 (±0.037)	1	0.007–0.09	1
KTX1	1.270 (±0.308)	2	1.487 (±0.260)	2	1.1–41	2
MTX	>1000 (NQ)	3	>1000 (NQ)	3	>100	3

Toxin binding to T+F KcsA-Kv1.x chimeras strongly correlates with their blocking potency, supporting their superiority over T-only variants for screening toxin-phage libraries. These chimeras were successfully applied in two microplate-based phage-ELISA assays—direct phage binding and competition assays—demonstrating their suitability for HTS by successful biopanning experiments. Their strong predictivity and scalability make them ideal tools for identifying highly selective Kv1.3 inhibitors, which could lead to novel treatments for chronic inflammatory diseases and overcome the limitations of previous attempts (e.g. Dalazatide) to develop highly selective Kv1.3 inhibitors.

Beyond these model systems, this research establishes a broader guidance for investigating miniproteins in drug discovery. The combination of scalable production, predictive chimeric screening, and optimized biopanning provides a strong pipeline for accelerating ligand identification. Future applications could extend these methodologies to other ion channels, proteases, and structurally complex drug targets, expanding the scope of miniproteins as a promising therapeutic modality. By integrating these approaches into early-stage drug development, this work contributes to more efficient screening strategies, paving the way for next-generation selective therapeutics.

DOI:10.14753/SE.2025.3224

7 SUMMARY

This thesis focuses on the development and optimization of HTS assays for two clinically validated yet hard-to-drug targets, MMP-2 and Kv1.3, implicated in various types of cancer and chronic inflammatory diseases, respectively. The goal was to establish scalable and reliable screening assays that facilitate target characterization and enable high-throughput identification of novel miniprotein therapeutics.

For MMP-2, two microbead-based flow cytometry assays were developed to characterize CTX and its variants. The Ig-coated bead binding assay confirmed a Kd of 0.62–0.75 μM, while the cobalt-coated bead binding assay revealed additional interactions with NRP1 and to lesser extent withCLC-3 and TIMP-2, supporting a multi-target role for CTX. To enable HTS applications, CTX was successfully displayed on phages, with experiments confirming that phage-bound CTX retained its binding profile, supporting its future optimization for glioblastoma therapy and diagnostics.

For Kv1.x channels, a systematic scaffold selection process was conducted to enable structured testing of Kv1.x chimeras and assess their reliability. From this, four scaffolds were chosen, each represented by a specific toxin: Vm24, HgTx1, MTX, and ShK. This approach ensures comprehensive evaluation and allows for future optimization of each scaffold primarly for selective Kv1.3 inhibition. T-only and T+F KcsA-Kv1.1, Kv1.2, and Kv1.3 chimeras were designed, produced and evaluated using microplate-based ELISA assays and patch-clamp measurements. The results demonstrated that T+F chimeras provided more predictive toxin-binding and blocking profiles, particularly for Kv1.2 and Kv1.3, whereas T-only Kv1.1 chimeras remained sufficient for accurate screening. Following this validation, the optimized chimeras were incorporated into a biopanning workflow, enabling the selection of Kv1.3-binding sequences from a phage library. This process led to up to 62.5-fold enrichment of Kv1.3-specific binders in a single selection cycle, confirming the effectiveness of the system in identifying selective inhibitors by directed evolution techniques.

8 REFERENCES

1. Crook ZR, Nairn NW, Olson JM. Miniproteins as a powerful modality in drug development. *Trends Biochem Sci*. 2020;45(4):332–46.

2. Ciesiołkiewicz A, Perez JL, Berlicki Ł. Miniproteins in medicinal chemistry. *Bioorg Med Chem Lett*. 2022;71:128806.

3. Norton RS, Chandy KG. Venom-derived peptide inhibitors of voltage-gated potassium channels. *Neuropharmacology*. 2017;127:124–38.

4. Evers A, Pfeiffer-Marek S, Bossart M, Heubel C, Stock U, Tiwari G, et al. Peptide optimization at the drug discovery-development interface: tailoring of physicochemical properties toward specific formulation requirements. *J Pharm Sci*. 2019;108(4):1404–14.

5. Muttenthaler M, King GF, Adams DJ, Alewood PF. Trends in peptide drug discovery. *Nat Rev Drug Discov*. 2021;20(4):309–25.

6. Barman P, Joshi S, Sharma S, Preet S, Sharma S, Saini A. Strategic approaches to improvise peptide drugs as next generation therapeutics. *Int J Pept Res Ther*. 2023;29(4):61.

7. Bordon KCF, Cologna CT, Fornari-Baldo EC, Pinheiro-Júnior EL, Cerni FA, Amorim FG, et al. From animal poisons and venoms to medicines: achievements, challenges and perspectives in drug discovery. *Front Pharmacol*. 2020;11:1132.

8. Casewell NR, Wüster W, Vonk FJ, Harrison RA, Fry BG. Complex cocktails: the evolutionary novelty of venoms. *Trends Ecol Evol*. 2013;28(4):219–29.

9. King GF, Gentz MC, Escoubas P, Nicholson GM. A rational nomenclature for naming peptide toxins from spiders and other venomous animals. *Toxicon*. 2008;52(2):264–76.

10. Stepensky D. Pharmacokinetics of toxin-derived peptide drugs. *Toxins (Basel)*. 2018;10(11):483.

11. Norton RS. Enhancing the therapeutic potential of peptide toxins. *Expert Opin Drug Discov*. 2017;12(6):611–23.

12. Honma T, Shiomi K. Peptide toxins in sea anemones: structural and functional aspects. *Mar Biotechnol (NY)*. 2006;8(1):1–10.

13. Pennington MW, Czerwinski A, Norton RS. Peptide therapeutics from venom: current status and potential. *Bioorg Med Chem*. 2018;26(10):2738–58.

14. Asada N, Krebs CF, Panzer U. Miniproteins may have a big impact: new therapeutics for autoimmune diseases and beyond. *Signal Transduct Target Ther*. 2024;9(1):298.

15. Cid-Uribe JI, Veytia-Bucheli JI, Romero-Gutierrez T, Ortiz E, Possani LD. Scorpion venomics: a 2019 overview. *Expert Rev Proteomics*. 2020;17(1):67–83.

16. Mohamed Abd El-Aziz T, Garcia Soares A, Stockand JD. Snake venoms in drug discovery: valuable therapeutic tools for life saving. *Toxins (Basel)*. 2019;11(10):564.

17. Mouhat S, Jouirou B, Mosbah A, De Waard M, Sabatier JM. Diversity of folds in animal toxins acting on ion channels. *Biochem J*. 2004;378(Pt 3):717–26.

18. Undheim EA, Mobli M, King GF. Toxin structures as evolutionary tools: using conserved 3D folds to study the evolution of rapidly evolving peptides. *Bioessays*. 2016;38(6):539–48.

19. Sunagar K, Undheim EA, Chan AH, Koludarov I, Muñoz-Gómez SA, Antunes A, et al. Evolution stings: the origin and diversification of scorpion toxin peptide scaffolds. *Toxins (Basel)*. 2013;5(12):2456–87.

20. Ghosh A, Roy R, Nandi M, Mukhopadhyay A. Scorpion venom-toxins that aid in drug development: a review. *Int J Pept Res Ther*. 2019;25(1):27–37.

21. Kalia J, Milescu M, Salvatierra J, Wagner J, Klint JK, King GF, et al. From foe to friend: using animal toxins to investigate ion channel function. *J Mol Biol*. 2015;427(1):158–75.

22. Bartok A, Panyi G, Varga Z. Potassium channel blocking peptide toxins from scorpion venom. In: Gopalakrishnakone P, editor. Scorpion venoms. *Dordrecht: Springer*; 2015. p. 493–527.

23. Kuzmenkov AI, Grishin EV, Vassilevski AA. Diversity of potassium channel ligands: focus on scorpion toxins. *Biochemistry (Mosc)*. 2015;80(13):1764–99.

24. Agwa AJ, Peigneur S, Chow CY, Lawrence N, Craik DJ, Tytgat J, et al. Gating modifier toxins isolated from spider venom: modulation of voltage-gated sodium channels and the role of lipid membranes. *J Biol Chem*. 2018;293(23):9041–52.

25. Mitragotri S, Burke PA, Langer R. Overcoming the challenges in administering biopharmaceuticals: formulation and delivery strategies. *Nat Rev Drug Discov*. 2014;13(9):655–72.

26. Gubič Š, Hendrickx LA, Toplak Ž, Sterle M, Peigneur S, Tomašič T, et al. Discovery of KV 1.3 ion channel inhibitors: medicinal chemistry approaches and challenges. *Med Res Rev*. 2021;41(4):2423–73.

27. Chen R, Chung SH. Structural basis of the selective block of Kv1.2 by maurotoxin from computer simulations. *PLoS One*. 2012;7(10):e47253.

28. Bryson CJ, Jones TD, Baker MP. Prediction of immunogenicity of therapeutic proteins: validity of computational tools. *BioDrugs*. 2010;24(1):1–8.

29. Gordon D, Chen R, Chung SH. Computational methods of studying the binding of toxins from venomous animals to biological ion channels: theory and applications. *Physiol Rev*. 2013;93(2):767–802.

30. Takacs Z, Toups M, Kollewe A, Johnson E, Cuello LG, Driessens G, et al. A designer ligand specific for Kv1.3 channels from a scorpion neurotoxin-based library. *Proc Natl Acad Sci U S A*. 2009;106(52):22211–6.

31. Herzig V, Cristofori-Armstrong B, Israel MR, Nixon SA, Vetter I, King GF. Animal toxins – nature's evolutionary-refined toolkit for basic research and drug discovery. *Biochem Pharmacol*. 2020;181:114096.

32. Swinney DC, Anthony J. How were new medicines discovered? *Nat Rev Drug Discov*. 2011;10(7):507–19.

33. Bibic L, Herzig V, King GF, Stokes L. Development of high-throughput fluorescent-based screens to accelerate discovery of P2X inhibitors from animal venoms. *J Nat Prod*. 2019;82(9):2559–67.

34. Prashanth JR, Hasaballah N, Vetter I. Pharmacological screening technologies for venom peptide discovery. *Neuropharmacology*. 2017;127:4–19.

35. Correnti CE, Gewe MM, Mehlin C, Bandaranayake AD, Johnsen WA, Rupert PB, et al. Screening, large-scale production and structure-based classification of cystine-dense peptides. *Nat Struct Mol Biol*. 2018;25(3):270–8.

36. Blay V, Tolani B, Ho SP, Arkin MR. High-throughput screening: today's biochemical and cell-based approaches. *Drug Discov Today*. 2020;25(10):1807–21.

37. Smith GP. Filamentous fusion phage: novel expression vectors that display cloned antigens on the virion surface. *Science*. 1985;228(4705):1315–7.

38. Bazan J, Całkosiński I, Gamian A. Phage display – a powerful technique for immunotherapy: 2. Vaccine delivery. *Hum Vaccin Immunother*. 2012;8(12):1829–35.

39. Smith GP, Petrenko VA. Phage display. *Chem Rev*. 1997;97(2):391–410.

40. Tan Y, Tian T, Liu W, Zhu Z, Yang CJ. Advance in phage display technology for bioanalysis. *Biotechnol J*. 2016;11(6):732–45.

41. Deng X, Wang L, You X, Dai P, Zeng Y. Advances in the T7 phage display system (review). *Mol Med Rep*. 2018;17(1):714–20.

42. Nicastro J, Sheldon K, Slavcev RA. Bacteriophage lambda display systems: developments and applications. *Appl Microbiol Biotechnol*. 2014;98(7):2853–66.

43. Rakonjac J, Bennett NJ, Spagnuolo J, Gagic D, Russel M. Filamentous bacteriophage: biology, phage display and nanotechnology applications. *Curr Issues Mol Biol*. 2011;13(2):51–76.

44. Wang R, Li HD, Cao Y, Wang ZY, Yang T, Wang JH. M13 phage: a versatile building block for a highly specific analysis platform. *Anal Bioanal Chem*. 2023;415(18):3927–44.

45. Ledsgaard L, Kilstrup M, Karatt-Vellatt A, McCafferty J, Laustsen AH. Basics of antibody phage display technology. *Toxins (Basel)*. 2018;10(6):236.

46. McGuire MJ, Li S, Brown KC. Biopanning of phage displayed peptide libraries for the isolation of cell-specific ligands. In: Martin B, editor. Methods in molecular biology. Vol. 504. *Totowa (NJ): Humana Press*; 2009. p. 291–321.

47. Alfaleh MA, Alsaab HO, Mahmoud AB, Alkayyal AA, Jones ML, Mahler SM, et al. Phage display derived monoclonal antibodies: from bench to bedside. *Front Immunol*. 2020;11:1986.

48. Laronha H, Caldeira J. Structure and function of human matrix metalloproteinases. *Cells*. 2020;9(5):1076.

49. Nagase H, Visse R, Murphy G. Structure and function of matrix metalloproteinases and TIMPs. *Cardiovasc Res*. 2006;69(3):562–73.

50. Gkouveris I, Nikitakis NG, Aseervatham J, Rao N, Ogbureke KUE. Matrix metalloproteinases in head and neck cancer: current perspectives. *Metalloproteinases Med*. 2017;4:47–61.

51. Löffek S, Schilling O, Franzke CW. Series "matrix metalloproteinases in lung health and disease": biological role of matrix metalloproteinases: a critical balance. *Eur Respir J*. 2011;38(1):191–208.

52. Clark IM, Swingler TE, Sampieri CL, Edwards DR. The regulation of matrix metalloproteinases and their inhibitors. *Int J Biochem Cell Biol*. 2008;40(6–7):1362–78.

53. Cabral-Pacheco GA, Garza-Veloz I, Castruita-De la Rosa C, Ramirez-Acuña JM, Perez-Romero BA, Guerrero-Rodriguez JF, et al. The roles of matrix metalloproteinases and their inhibitors in human diseases. *Int J Mol Sci*. 2020;21(24):9739.

54. Hadler-Olsen E, Winberg JO, Uhlin-Hansen L. Matrix metalloproteinases in cancer: their value as diagnostic and prognostic markers and therapeutic targets. *Tumour Biol*. 2013;34(4):2041–51.

55. Cathcart JM, Cao J. MMP inhibitors: past, present and future. *Front Biosci (Landmark Ed)*. 2015;20(7):1164–78.

56. Fields GB. The rebirth of matrix metalloproteinase inhibitors: moving beyond the dogma. *Cells*. 2019;8(9):984.

57. Wolosowicz M, Prokopiuk S, Kaminski TW. The complex role of matrix metalloproteinase-2 (MMP-2) in health and disease. *Int J Mol Sci*. 2024;25(24):13691.

58. Zhou W, Yu X, Sun S, Zhang X, Yang W, Zhang J, Zhang X, Jiang Z. Increased expression of MMP-2 and MMP-9 indicates poor prognosis in glioma recurrence. *Biomed Pharmacother*. 2019;118:109369.

59. Ramachandran RK, Sørensen MD, Aaberg-Jessen C, Hermansen SK, Kristensen BW. Expression and prognostic impact of matrix metalloproteinase-2 (MMP-2) in astrocytomas. *PLoS One*. 2017;12(2):e0172234.

60. John A, Tuszynski G. The role of matrix metalloproteinases in tumor angiogenesis and tumor metastasis. *Pathol Oncol Res*. 2001;7(1):14–23.

61. Cohen-Inbar O, Zaaroor M. Glioblastoma multiforme targeted therapy: The Chlorotoxin story. *J Clin Neurosci*. 2016;33:52–58.

62. Du R, Petritsch C, Lu K, Liu P, Haller A, Ganss R, et al. Matrix metalloproteinase-2 regulates vascular patterning and growth affecting tumor cell survival and invasion in GBM. *Neuro Oncol*. 2008;10(3):254–64.

63. Ramachandran RK, Sørensen MD, Aaberg-Jessen C, Hermansen SK, Kristensen BW. Expression and prognostic impact of matrix metalloproteinase-2 (MMP-2) in astrocytomas. *PLoS One*. 2017;12(2):e0172234.

64. Zhong Y, Lu YT, Sun Y, Shi ZH, Li NG, Tang YP, Duan JA. Recent opportunities in matrix metalloproteinase inhibitor drug design for cancer. *Expert Opin Drug Discov*. 2018;13(1):75–87.

65. Gialeli C, Theocharis AD, Karamanos NK. Roles of matrix metalloproteinases in cancer progression and their pharmacological targeting. *FEBS J*. 2011;278(1):16–27.

66. Fu YJ, Yin LT, Liang AH, Zhang CF, Wang W, Chai BF, et al. Therapeutic potential of chlorotoxin-like neurotoxin from the Chinese scorpion for human gliomas. *Neurosci Lett*. 2007;412(1):62–7.

67. Ojeda PG, Wang CK, Craik DJ. Chlorotoxin: Structure, activity, and potential uses in cancer therapy. *Biopolymers*. 2016;106(1):25–36.

68. Dardevet L, Rani D, Aziz TA, Bazin I, Sabatier JM, Fadl M, et al. Chlorotoxin: a helpful natural scorpion peptide to diagnose glioma and fight tumor invasion. *Toxins (Basel)*. 2015;7(4):1079–101.

69. Lyons SA, O'Neal J, Sontheimer H. Chlorotoxin, a scorpion-derived peptide, specifically binds to gliomas and tumors of neuroectodermal origin. *Glia*. 2002;39(2):162–73.

70. Deshane J, Garner CC, Sontheimer H. Chlorotoxin inhibits glioma cell invasion via matrix metalloproteinase-2. *J Biol Chem*. 2003;278(6):4135–44.

71. Dintzis SM, Hansen S, Harrington KM, Tan LC, Miller DM, Ishak L, et al. Real-time visualization of breast carcinoma in pathology specimens from patients receiving fluorescent tumor-marking agent tozuleristide. *Arch Pathol Lab Med*. 2019;143(9):1076–83.

72. Soroceanu L, Gillespie Y, Khazaeli MB, Sontheimer H. Use of chlorotoxin for targeting of primary brain tumors. *Cancer Res*. 1998;58(21):4871–9.

73. Yamada M, Miller DM, Lowe M, Rowe C, Wood D, Soyer HP, et al. A first-in-human study of BLZ-100 (tozuleristide) demonstrates tolerability and safety in skin cancer patients. *Contemp Clin Trials Commun*. 2021;23:100830.

74. DeBin JA, Maggio JE, Strichartz GR. Purification and characterization of chlorotoxin, a chloride channel ligand from the venom of the scorpion. *Am J Physiol*. 1993;264(2 Pt 1):C361–9.

75. Veiseh M, Gabikian P, Bahrami SB, Veiseh O, Zhang M, Hackman RC, et al. Tumor paint: a chlorotoxin:Cy5.5 bioconjugate for intraoperative visualization of cancer foci. *Cancer Res*. 2007;67(14):6882–8.

76. McGonigle S, Majumder U, Kolber-Simonds D, Wu J, Hart A, Noland T, et al. Neuropilin-1 drives tumor-specific uptake of chlorotoxin. *Cell Commun Signal*. 2019;17(1):67.

77. Kesavan K, Ratliff J, Johnson EW, Dahlberg W, Asara JM, Misra P, et al. Annexin A2 is a molecular target for TM601, a peptide with tumor-targeting and anti-angiogenic effects. *J Biol Chem*. 2010;285(7):4366–74.

78. Su Z, Brown EC, Wang W, MacKinnon R. Novel cell-free high-throughput screening method for pharmacological tools targeting K+ channels. *Proc Natl Acad Sci U S A*. 2016;113(20):5748–53.

79. Tian C, Zhu R, Zhu L, Qiu T, Cao Z, Kang T. Potassium channels: structures, diseases, and modulators. *Chem Biol Drug Des*. 2014;83(1):1–26.

80. Shieh CC, Coghlan M, Sullivan JP, Gopalakrishnan M. Potassium channels: molecular defects, diseases, and therapeutic opportunities. *Pharmacol Rev*. 2000;52(4):557–94.

81. Moulton G, Attwood TK, Parry-Smith DJ, Packer JCL. Phylogenomic analysis and evolution of the potassium channel gene family. *Recept Channels*. 2003;9(6):363–77.

82. González C, Baez-Nieto D, Valencia I, Oyarzún I, Rojas P, Naranjo D, et al. K+ channels: Function-structural overview. *Compr Physiol*. 2012;2(3):2087–149.

83. Villalonga N, Escalada A, Vicente R, Sánchez-Tilló E, Celada A, Solsona C, et al. Kv1.3/Kv1.5 heteromeric channels compromise pharmacological responses in macrophages. *Biochem Biophys Res Commun*. 2007;352(4):913–8.

84. Rudy B, Maffie J, Amarillo Y, Clark B, Goldberg EM, Jeong HY, et al. Voltage Gated Potassium Channels: Structure and Function of Kv1 to Kv9 Subfamilies. *Encyclopedia of Neuroscience*. 2009;7:397–425.

85. Wulff H, Castle NA, Pardo LA. Voltage-gated potassium channels as therapeutic targets. *Nat Rev Drug Discov*. 2009;8(12):982–1001.

86. Pardo LA. Voltage-gated potassium channels in cell proliferation. *Physiology*. 2004;19(5):285–92.

87. D'Adamo MC, Liantonio A, Rolland JF, Pessia M, Imbrici P. Kv1.1 channelopathies: pathophysiological mechanisms and therapeutic approaches. *Int J Mol Sci*. 2020;21(8):2935.

88. Lin King YH, Chen C, Lin King JV, Simms J, Glasscock E, Yang SB, et al. Kv1.1 preserves the neural stem cell pool and facilitates neuron maturation during adult hippocampal neurogenesis. *Proc Natl Acad Sci U S A*. 2022;119(22):e2118240119.

89. Shen W, Hernandez-Lopez S, Tkatch T, Held JE, Surmeier DJ. Kv1.2-containing K+ channels regulate subthreshold excitability of striatal medium spiny neurons. *J Neurophysiol*. 2004;91(3):1337–49.

90. Robbins CA, Tempel BL. Kv1.1 and Kv1.2: Similar channels, different seizure models. *Epilepsia*. 2012;53(Suppl. 1):134–41.

91. Xie G, Harrison J, Clapcote SJ, Huang Y, Zhang JY, Wang LY, et al. A new Kv1.2 channelopathy underlying cerebellar ataxia. *J Biol Chem*. 2010;285(42):32160–73.

92. Cahalan MD, Chandy KG, DeCoursey TE, Gupta S. A voltage-gated potassium channel in human T lymphocytes. *J Physiol*. 1985;358(1):197–237.

93. Chandy KG, Cahalan M, Pennington M, Norton RS, Wulff H, Gutman GA. Potassium channels in T lymphocytes: toxins to therapeutic immunosuppressants. *Toxicon*. 2001;39(9):1269–76.

94. Panyi G, Varga Z, Gáspár R. Ion channels and lymphocyte activation. *Immunol Lett*. 2004;92(1–2):55–66.

95. Cahalan MD, Chandy KG. The functional network of ion channels in T lymphocytes. *Immunol Rev*. 2009;231(1):59–87.

96. Wang Y, DeMazumder D, Hill JA. Ionic fluxes and genesis of the cardiac action potential. In: Muscle: fundamental biology and mechanisms of disease. Vol. 1-2. *Elsevier*; 2012. p. 67–85.

97. Tao Y, Zeng R, Shen B, Jia J, Wang Y. Neuronal transmission stimulates the phosphorylation of Kv1.4 channel at Ser229 through protein kinase A1. *J Neurochem*. 2005;94(6):1512–22.

98. Borrego J, Feher A, Jost N, Panyi G, Varga Z, Papp F. Peptide inhibitors of Kv1.5: An option for the treatment of atrial fibrillation. *Pharmaceuticals (Basel).* 2021;14(12):1303.

99. Ohanyan V, Yin L, Bardakjian R, Kolz C, Enrick M, Hakobyan T, et al. Requisite role of Kv1.5 channels in coronary metabolic dilation. *Circ Res*. 2015;117(7):612–21.

100. Pérez-García MT, Cidad P, López-López JR. The secret life of ion channels: Kv1.3 potassium channels and proliferation. *Am J Physiol Cell Physiol*. 2018;314(1):C27–C42.

101. Chi V, Pennington MW, Norton RS, Tarcha EJ, Londono LM, Sims-Fahey B, et al. Development of a sea anemone toxin as an immunomodulator for therapy of autoimmune diseases. *Toxicon*. 2012;59(4):529–46.

102. Tarcha EJ, Chi V, Muñoz-Elías EJ, Bailey D, Londono LM, Upadhyay SK, et al. Durable pharmacological responses from the peptide ShK-186, a specific Kv1.3 channel inhibitor that suppresses T cell mediators of autoimmune disease. *J Pharmacol Exp Ther*. 2012;342(3):642–53.

103. Nicolaou SA, Neumeier L, Steckly A, Kucher V, Takimoto K, Conforti L. Localization of Kv1.3 channels in the immunological synapse modulates the calcium response to antigen stimulation in T lymphocytes. *J Immunol*. 2009;183(10):6296–302.

104. Pérez-Verdaguer M, Capera J, Serrano-Novillo C, Estadella I, Sastre D, Felipe A. The voltage-gated potassium channel Kv1.3 is a promising multitherapeutic target against human pathologies. *Expert Opin Ther Targets*. 2016;20(5):577–91.

105. Beeton C, Wulff H, Standifer NE, Azam P, Mullen KM, Pennington MW, et al. Kv1.3 channels are a therapeutic target for T cell-mediated autoimmune diseases. *Proc Natl Acad Sci U S A*. 2006;103(46):17414–9.

106. Chiang EY, Li T, Jeet S, Peng I, Zhang J, Lee WP, et al. Potassium channels Kv1.3 and KCa3.1 cooperatively and compensatorily regulate antigen-specific memory T cell functions. *Nat Commun*. 2017;8:14644.

107. Lam J, Wulff H. The lymphocyte potassium channels Kv1.3 and KCa3.1 as targets for immunosuppression. *Drug Dev Res*. 2011;72(7):573–84.

108. Chandy KG, Sanches K, Norton RS. Structure of the voltage-gated potassium channel KV1.3: insights into the inactivated conformation and binding to therapeutic leads. *Channels (Austin)*. 2023;17(1):2253104.

109. Wulff H, Calabresi PA, Allie R, Yun S, Pennington M, Beeton C, et al. The voltage-gated Kv1.3 K+ channel in effector memory T cells as new target for MS. *J Clin Invest*. 2003;111(11):1703–13.

110. Beeton C, Wulff H, Singh S, Botsko S, Crossley G, Gutman GA, et al. A novel fluorescent toxin to detect and investigate Kv1.3 channel up-regulation in chronically activated T lymphocytes. *J Biol Chem*. 2003;278(11):9928–37.

111. Chandy KG, Wulff H, Beeton C, Pennington M, Gutman GA, Cahalan MD. K+ channels as targets for specific immunomodulation. *Trends Pharmacol Sci*. 2004;25(5):280–9.

112. Beeton C, Chandy KG. Potassium channels, memory T cells, and multiple sclerosis. *Neuroscientist*. 2005;11(6):550–62.

113. Rus H, Pardo CA, Hu L, Darrah E, Cudrici C, Niculescu T, et al. The voltage-gated potassium channel Kv1.3 is highly expressed on inflammatory infiltrates in multiple sclerosis brain. *Proc Natl Acad Sci U S A*. 2005;102(31):11094–9.

114. Serrano-Albarrás A, Estadella I, Cirera-Rocosa S, Navarro-Pérez M, Felipe A. Kv1.3: a multifunctional channel with many pathological implications. *Expert Opin Ther Targets*. 2018;22(2):101–5.

115. Cheng S, Jiang D, Lan X, Liu K, Fan C. Voltage-gated potassium channel 1.3: A promising molecular target in multiple disease therapy. *Biomed Pharmacother*. 2024;175:116651.

116. Azam P, Sankaranarayanan A, Homerick D, Griffey S, Wulff H. Targeting effector memory T cells with the small molecule Kv1.3 blocker PAP-1 suppresses allergic contact dermatitis. *J Invest Dermatol*. 2007;127(6):1419–29.

117. Bradding P, Wulff H. The K+ channels K(Ca)3.1 and K(v)1.3 as novel targets for asthma therapy. *Br J Pharmacol*. 2009;157(8):1330–9.

118. Gilhar A, Keren A, Shemer A, D'Ovidio R, Ullmann Y, Paus R. Autoimmune disease induction in a healthy human organ: A humanized mouse model of alopecia areata. *J Invest Dermatol*. 2013;133(3):844–7.

119. Fugger L, Jensen LT, Rossjohn J. Challenges, Progress, and Prospects of Developing Therapies to Treat Autoimmune Diseases. *Cell*. 2020;181(1):63–80.

120. Chang SC, Bajaj S, Chandy KG. ShK toxin: history, structure and therapeutic applications for autoimmune diseases. *WikiJ Sci*. 2018;1(1):3.

121. Beeton C, Pennington MW, Norton RS. Analogs of the sea anemone potassium channel blocker ShK for the treatment of autoimmune diseases. *Inflamm Allergy Drug Targets*. 2011;10(5):313–21.

122. Yin SJ, Jiang L, Yi H, Han S, Yang DW, Liu ML, et al. Different residues in channel turret determining the selectivity of ADWX-1 inhibitor peptide between Kv1.1 and Kv1.3 channels. *J Proteome Res*. 2008;7(11):4890–7.

123. Bednenko J, Harriman R, Mariën L, Nguyen HM, Agrawal A, Papoyan A, et al. A multiplatform strategy for the discovery of conventional monoclonal antibodies that inhibit the voltage-gated potassium channel Kv1.3. *MAbs*. 2018;10(4):636–50.

124. Rashid MH, Kuyucak S. Free energy simulations of binding of HsTx1 toxin to Kv1 potassium channels: the basis of Kv1.3/Kv1.1 selectivity. *J Phys Chem B*. 2014;118(3):707–16.

125. Varga Z, Tajti G, Panyi G. The Kv1.3 K+ channel in the immune system and its "precision pharmacology" using peptide toxins. *Biol Futur*. 2021;72(1):75–83.

126. Shen B, Cao Z, Li W, Sabatier JM, Wu Y. Treating autoimmune disorders with venom-derived peptides. *Expert Opin Biol Ther*. 2017;17(9):1065–75.

127. Chandy KG, Norton RS. Peptide blockers of Kv1.3 channels in T cells as therapeutics for autoimmune disease. *Curr Opin Chem Biol.* 2017;38:97–107.

128. Jouirou B, Mouhat S, Andreotti N, De Waard M, Sabatier JM. Toxin determinants required for interaction with voltage-gated K + channels. *Toxicon*. 2004;43(8):909–14.

129. Yu K, Fu W, Liu H, Luo X, Chen KX, Ding J, et al. Computational simulations of interactions of scorpion toxins with the voltage-gated potassium ion channel. *Biophys J*. 2004;86(6):3542–55.

130. Stehling EG, Sforça ML, Zanchin NIT, Oyama S, Pignatelli A, Belluzzi O, et al. Looking over toxin-K + channel interactions. clues from the structural and functional characterization of α-KTx Toxin Tc32, a Kv1.3 Channel Blocker. *Biochemistry*. 2012;51(9):1885–94.

131. Visan V, Fajloun Z, Sabatier JM, Grissmer S. Mapping of maurotoxin binding sites on hKv1.2, hKv1.3, and hlKCa1 channels. *Mol Pharmacol*. 2004;66(5):1103–12.

132. Koschak A, Bugianesi RM, Mitterdorfer J, Kaczorowski GJ, Garcia ML, Knaus HG. Subunit composition of brain voltage-gated potassium channels determined by hongotoxin-1, a novel peptide derived from Centruroides limbatus venom. *J Biol Chem*. 1998;273(5):2639–44.

133. Grissmer S, Nguyen AN, Aiyar J, Hanson DC, Mather RJ, Gutman GA, et al. Pharmacological characterization of five cloned voltage-gated K+ channels, types Kv1.1, 1.2, 1.3, 1.5, and 3.1, stably expressed in mammalian cell lines. *Mol Pharmacol.* 1994;45(6):1227–34.

134. Kalman K, Pennington MW, Lanigan MD, Nguyen A, Rauer H, Mahnir V, et al. Shk-Dap22, a potent Kv1.3-specific immunosuppressive polypeptide. *J Biol Chem*. 1998;273(49):32697–707.

135. Tarcha EJ, Olsen CM, Probst P, Peckham D, Muñoz-Elías EJ, Kruger JG, et al. Safety and pharmacodynamics of dalazatide, a Kv1.3 channel inhibitor, in the treatment of plaque psoriasis: A randomized phase 1b trial. *PLoS One*. 2017;12(7):1–19.

136. Tajti G, Wai DCC, Panyi G, Norton RS. The voltage-gated potassium channel KV1.3 as a therapeutic target for venom-derived peptides. *Biochem Pharmacol*. 2020;181:114146.

137. WO2021053194A1.

138. Szekér P, Bodó T, Klima K, Csóti Á, Hanh NN, Murányi J, et al. KcsA-Kv1.x chimeras with complete ligand-binding sites provide improved predictivity for screening selective Kv1.x blockers. *J Biol Chem*. 2024;300(4):107155.

139. Doyle DA, Morais Cabral J, Pfuetzner RA, Kuo A, Gulbis JM, Cohen SL, et al. The structure of the potassium channel: molecular basis of K+ conduction and selectivity. *Science.* 1998;280(5360):69–77.

140. Legros C, Pollmann V, Knaus HG, Farrell AM, Darbon H, Bougis PE, et al. Generating a high affinity scorpion toxin receptor in KcsA-Kv1.3 chimeric potassium channels. *J Biol Chem*. 2000;275(22):16918–24.

141. Legros C. Affinity capture using chimeric membrane proteins bound to magnetic beads for rapid ligand screening by matrix-assisted laser desorption/ionization time-of-flight mass spectrometry. *Rapid Commun Mass Spectrom*. 2009;24:1457–66.

142. Legros C, Schulze C, Garcia ML, Bougis PE, Martin-Eauclaire MF, Pongs O. Engineering-specific pharmacological binding sites for peptidyl inhibitors of potassium channels into KcsA. *Biochemistry*. 2002;41(51):15369–75.

143. MacKinnon R, Heginbotham L, Abramson T. Mapping the receptor site for charybdotoxin, a pore-blocking potassium channel inhibitor. *Neuron*. 1990;5(6):767–71.

144. Alessandri-Haber N, Lecoq A, Gasparini S, Grangier-Macmath G, Jacquet G, Harvey AL, et al. Mapping the functional anatomy of BgK on Kv1.1, Kv1.2, and Kv1.3. Clues to design analogs with enhanced selectivity. *J Biol Chem*. 1999;274(50):35653–61.

145. Tyagi A, Ahmed T, Jian S, Bajaj S, Ong ST, Goay SSM, et al. Rearrangement of a unique Kv1.3 selectivity filter conformation upon binding of a drug. *Proc Natl Acad Sci U S A*. 2022;119(5):1–10.

146. Gurrola GB, Hernández-López RA, Rodríguez De La Vega RC, Varga Z, Batista CVF, Salas-Castillo SP, et al. Structure, function, and chemical synthesis of Vaejovis mexicanus peptide 24: A novel potent blocker of Kv1.3 potassium channels of human T lymphocytes. *Biochemistry*. 2012;51(19):4049–61.

147. Zhao Y, Chen Z, Cao Z, Li W, Wu Y. Diverse structural features of potassium channels characterized by scorpion toxins as molecular probes. *Molecules*. 2019;24(11):1–16.

148. Tonikian R, Zhang Y, Boone C, Sidhu SS. Identifying specificity profiles for peptide recognition modules from phage-displayed peptide libraries. *Nat Protoc*. 2007;2(6):1368–86.

149. Farkas S, Cioca D, Murányi J, Hornyák P, Brunyánszki A, Szekér P, et al. Chlorotoxin binds to both matrix metalloproteinase 2 and neuropilin 1. *J Biol Chem*. 2023;299(9).

150. Skolnick J, Gao M, Zhou H, Singh S. AlphaFold 2: why it works and its implications for understanding the relationships of protein sequence, structure, and function. *J Chem Inf Model*. 2021;61(10):4827–31.

151. Mahapatra MK, Karuppasamy M, Sahoo BM. Semaglutide, a glucagon like peptide-1 receptor agonist with cardiovascular benefits for management of type 2

diabetes. In: Reviews in Endocrine and Metabolic Disorders. Vol. 23. *Springer*; 2022. p. 521–39.

9 BIBLIOGRAPHY OF THE CANDIDATE'S PUBLICATIONS

9.1 Publications related to the thesis

Szekér P, Bodó T, Klima K, Csóti Á, Hanh NN, Murányi J, Hajdara A, Szántó TG, Panyi G, Megyeri M, Péterfi Z, Farkas S, Gyöngyösi N, Hornyák P. KcsA-Kv1.x chimeras with complete ligand-binding sites provide improved predictivity for screening selective Kv1.x blockers. *J Biol Chem*. 2024;300(4):107155.

Farkas S, Cioca D, Murányi J, Hornyák P, Brunyánszki A, Szekér P, Boros E, Horváth P, Hujber Z, Rácz GZ, Nagy N, Tóth R, Nyitray L, Péterfi Z. Chlorotoxin binds to both matrix metalloproteinase 2 and neuropilin 1. *J Biol Chem*. 2023;299(9):104998.

9.2 Further scientific publications

Jankovics H, Szekér P, Tóth É, Kakasi B, Lábadi Z, Saftics A, Kalas B, Fried M, Petrik P, Vonderviszt F. Flagellin-based electrochemical sensing layer for arsenic detection in water. *Sci Rep*. 2021;11(1):3497.

DOI:10.14753/SE.2025.3224

10 ACKNOWLEDGEMENTS

First and foremost, I would like to express my gratitude to my supervisor, **Dr. Norbert Gyöngyösi**, for his guidance and support throughout my PhD journey. His scientific expertise, encouragement, and constructive feedback have been instrumental in shaping this work, and I am sincerely grateful for his mentorship.

I am also immensely thankful to **Dr. Zalán Péterfi**, whose scientific and industrial mentorship at VRG Therapeutics has provided critical insights and direction, bridging academic research with real-world applications.

A special thanks to **Dr. Péter Hornyák**, whose expertise in chimera design and production played a crucial role in this work. His mentorship and technical knowledge greatly contributed to the success of my work.

I would also like to acknowledge **Dr. Sándor Farkas** and **Dr. Márton Megyeri**, whose industrial mentorship helped me navigate the translational aspects of this research.

I am particularly grateful to **Tamás Bodó** for his contributions to chimera design and production and to **Katalin Klima** and **Hanh Nikoletta Ngo** for their technical support in phage display, both of whom played an essential role in the experimental success of this project.

I am especially grateful to **Professor György Panyi** and **Dr. Szántó Gábor Tibor** for performing the patch-clamp experiments. I deeply appreciate their support and collaboration.

I also want to extend my appreciation to **all my colleagues at VRG Therapeutics**, where my work was performed, whose collaboration, discussions, and guidance significantly impacted the outcomes of my research. Working in such an inspiring and supportive environment has been a privilege, and I really appreciate the teamwork and shared knowledge that shaped this project.

Lastly, I want to express my deepest gratitude to my **family and friends** for their endless encouragement, patience, and belief in me. Their support has been my foundation throughout this journey.

DOI:10.14753/SE.2025.3224

This work was supported by the National Research Development and Innovation Fund of Hungary: **2019-1.1.1-PIACI-KFI-2019-00127** funding was granted to Vascular Venture Ltd. The project no. 1019577 has been implemented with the support provided by the Ministry of Culture and Innovation of Hungary from the National Research, Development and Innovation Fund, financed under the **KDP-2020** funding scheme.